MICROSTRUCTURAL ANALYSIS OF PLATES WITH LARGE STRAINS AS A RESULT OF CENTRAL LOCALISED BLAST LOADING

BY

MICHAEL PHILIP SMITH

A thesis submitted in partial fulfilment of the requirements for the degree of Master of Science in Engineering

Department of Mechanical Engineering
University of Cape Town

January 1999

ACKNOWLEDGEMENTS

My sincere thanks to the following people:

- My supervisor Professor G.N. Nurick for his interest and guidance through my masters thesis. To Professor R.B. Tait for his advice and to Dawn Beckett for all her help.
- My friends and colleagues for their untiring interest, encouragement and advice.
- The staff of the UCT EM unit, Dane Gernrke, Miranda Waldron, Trevor Sewell, William Williams and Mohammed Jaffer. For their invaluable teaching on the use of the SEM and the work done on processing the micrographs.
- Mira Topic of the materials for her help in polishing and mounting of my specimens.
- My parents for their confidence and encouragement from miles away.

I would also like to thank CERECAM and the FRD for their financial support.

ABSTRACT

The deformation response and subsequent tearing of built in plates subjected to central impulsive loading has been investigated experimentally in the past. Theoretical predictions of the structural response have also been made and compared to these experiments. In this thesis, a new method is developed whereby the strains within the deformed plates were measured using micrographs of the grain structure of the plate. The aim of the thesis was to gain a fuller understanding of the internal deformation of blast loaded plate so as to enable more accurate theoretical predictions of plate deformation and tearing.

The dimensions of the grains of the plate material both in the virgin state and after deformation were measured by image analysis of scanning electron micrographs. These measurements were processed and averaged at various points within the structure. This enabled the strain distribution throughout the deformed plate to be analysed.

Tensile tests were undertaken in order to calibrate this method of strain measurement. The tests were arrested during the loading, after the specimen had undergone a known amount of strain. The strain measured from the microstructure was then compared to the strain measured during the tensile tests. The method was found to give a satisfactory measurement of the strain in the tensile tests.

The strain data obtained from the metallurgical investigation was analysed in order to provide information about the deformation of the plates. The strain distribution along the radius of the plate was plotted and it was found that the strains tended to rise to their highest values at the plate boundary and centre. This was particularly noticeable in plates which underwent large impulses. It was also found that at high impulses, in thinner plates, most of the elongation of the plate occurred at the boundary and centre of the plate, or near the cap when failure occurred. The total elongation and plastic work of the plate was also calculated from the grain data.

Numerical modelling was undertaken using ABAQUS general finite element package. Models were made of both the tensile tests and the blast loaded plates. The strain values obtained from these models were compared to the measured strains. They were found to compare favourably especially in plates which had not failed.

It was concluded that this method provides important information as to the straining of blast loaded plates. It shows that there are large variances of strain along the radius of deformed plate which has been difficult to measure in the past. This method could be used to provide further strain data, which would aid the prediction of deformation and tearing of blast loaded plates.

TABLE OF CONTENTS

LIST OF FIGURES

NOMENCLATURE

a	Loading radius
A	Grain area
D, D_s	Damage variable
H	Beam thickness
I	Impulse
k	Exponential constant
L	Beam length
M_0	Applied moment
P_0	Applied pressure
R	Radius of plate
t	Plate thickness
u	Displacement
V_0	Applied velocity
w	Deflection
W_f	Final mid-point deflection
ρ	Density
$\frac{W_f}{t}$	Deflection thickness ratio
ϕ	Dimensionless impulse: $\frac{I}{\pi R t^2 (\rho \sigma_0)^{1/2}}$
μ	Mass per unit area
ν	Poisons ratio
ε_m	Rupture strain
α_r	Grain aspect ratio
γ	Grain orientation
ε^{gr}	Strain of single grain
$\ddot{u}$	Acceleration

τ	Blast loading time
σ_0	Static yield stress
σ_{true}	True (Cauchy) stress
σ_{nom}	Nominal stress
$\varepsilon_{\ln}^{pl}$	Logarithmic plastic strain
ε_{nom}	Nominal strain
ω	ABAQUS damage parameter
$\dot{\varepsilon}^{pl}$	Plastic strain rate
$\bar{\varepsilon}^{pl}$	Equivalent plastic stain (peeq)
$\dot{u}$	Velocity

CHAPTER 1

INTRODUCTION

1.1 Background

Impulsive loading of circular plates has been an ongoing field of research since the Second World War. Research has been of both an experimental as well as a theoretical nature with the emphasis being on the understanding and predicting of the deformation process. There are numerous examples in engineering where understanding of impulsive behaviour of thin plates is crucial. Examples are: the blast resistance and crashworthiness of aircraft, motor vehicles and ships as well the ability of high risk installations such as nuclear power plants and factories producing volatile chemicals to withstand catastrophic events.

The study of blast loaded structures is highly complex. Two of the most important complications are, the nature of the loading and the response of the structure. The loading is highly transient as the time of the loading event is about 2-20μs for blast loaded plates. The precise load shape and time history of the loading is unknown due to the very high load magnitude and transient nature of the loading. The structural response is also difficult to access as the deformation takes place in approximately 250μ s for 100mm diameter plates and the deformation response is therefore very difficult to determine. The material is also acutely affected by the very high strain rates and the inertia effects in the structure become significant.

The study of blast loaded plates can be placed into two main loading configurations: firstly, uniformly loaded plates and secondly; central locally loaded plates. Within each of these two categories, there are many different areas of study such as the effect of thickness, load magnitude, boundary fixation conditions and modes of failure. The bulk of studies both experimental and theoretical have been on uniformly loaded plates. The prediction of mid-point deflection has been the main focus of most studies. Some investigations have moved into other areas such as evaluating the deformation energy, assessing the effect of the fixation conditions and understanding the mechanisms of failure.

Recent investigations have been undertaken into the response of circular plates to central localised blast loads. Other than deformation profile and the mid point deflection, the effect of the plate thickness and the loading diameter have been considered. It has been found that the failure of centrally loaded plates occurs in two possible ways. The failure either occurs at the boundary or at a central cap of the plate or at both. The position of the failure is dependant on the magnitude of the impulse as well as the load diameter.

The failure of blast loaded plates is not well understood and predictions of failure have proved inadequate. This is largely due to the difficulty in understanding the stress and strain conditions within the structure during the deformation. This study attempts to provide more information into the strain response of the structure by using a metallurgical investigation to determine the strain within the structure. The grain structure and its response to the global deformation is considered and this used to infer the local strain. Numerical modelling is also used to provide a comparison and supplement the metallurgical analysis.

1.2 Objectives

The objectives of this project are to:

a) To investigate the grain elongation in blast loaded plates by studying electron micrographs of sections of the plate.

b) Find a method of relating grain elongation to localised strain that could be applied to grain aspect ratio data obtained from micrographs.

c) Consider the distribution of strain along the radius and through the thickness of the blast loaded plates.

d) Determine the areas of the plate undergoing the largest elongation and deformation.

e) Identify the failure mechanism of blast loaded plates by investigating the failure surfaces and the grain structure near to it using a scanning electron microscope.

f) Investigate the use of a uniaxial rupture strain criterion for predicting the strain at which blast loaded plates would fail.

g) Set up a numerical model to make comparisons with the findings of the metallographic analysis.

1.3 Structure of the Thesis

The report begins with a review of the literature presented on the topic of blast loaded plates and their failure. In the literature review, experimental work that has been undertaken is briefly described and theoretical work on the deformation of blast loaded plates is reviewed. Studies that have been undertaken on the numerical modelling of blast loaded plates are reviewed. Finally theories of ductile necking and failure are considered.

The experimental method for blast loading of the plates is described. The technique of specimen preparation and the analysis of the microstructure of the plates is explained. The method used to obtain numerical strain data from the metallurgical analysis is explained.

The results of the metallurgical analysis are given in the fourth chapter. Firstly, the method of correlating the strain to the grain aspect ratio using both a simple strain theory and tensile tests is described. Results of the investigation are given in which the strain distribution along the radius and through the thickness of the plate are shown. The elongation distribution across the plate is also discussed. Some consideration is given to the total elongation and the deformation energy. At the end of the section, micrographs of the failure surface are shown and discussed.

The method of the numerical modelling is presented for both tensile tests and blast loaded plates. Topics such as loading, meshing, symmetry and material properties are discussed. The results of the numerical modelling are reported. Details of the strain profiles, strain history, deformation history and failure modelling are given.

Finally, conclusions are drawn from the study and recommendations are made for further work based on the results of this study.

CHAPTER 2

LITERATURE REVIEW

2.1 Experimental Work on Impulsively Loaded Plates.

2.1.1 Introduction

Experimental work on the impulsive loading of plates has been an on going field of research for the last fifty years. Experiments have been carried out where plates have been impulsively loaded using indentors, underwater blasts, air blasts and sheet explosive blasts. The types of plates used have also been varied, with circular and rectangular plates of various dimensions being used. In most cases the primary objective of the experiments were to measure the final deformed shape, but some of the experiments measured the impulse and attempted to measure the time deflection history.

Over the years, many methods have been used to obtain more information from the experiments than just the final deformed shape. The reason that data and observations have been difficult to obtain is the high speed of the loading (2-20μs) and the deformation of the plate (approximately 200μs). Methods that have been used to record the transient plate response include; high-speed photography, strain gauges, stereophotogrammetric techniques, condenser microphones and light interference methods [1].

Nurick and Martin present a review article [1] in which experimental work up to 1988 is reviewed. The review article compares some of the experiments by comparing the

damage number (a number that incorporates loading, material properties and dimensions) and the displacement-thickness ratio (a dimensionless number related to the mid point deflection). Nurick and Martin showed that this method of comparison gave good correlation between the experimental data that was examined.

The experimental work, which is of the most relevance to this investigation is that which was done using sheet explosive blasting of circular plates. Florence and Wierzbicki [2] and Duffey and Key [3] carried out experiments on edged-clamped circular plates with uniform loading using sheet explosives. Duffey and Key used high-speed photography and strain gauges to obtain a deflection time history.

Jones *et al.* [4] used a ballistic pendulum to measure the impulse on fully-clamped rectangular plates and the impulse was related to the midpoint deflection. Jones *et al.* also showed that using an attenuator (neoprene or foam) to prevent spalation did no affect the results of the tests but the attenuator used did affect the impulsive velocity.

Bodner and Symonds [5] performed experiments to investigate the response of fully clamped circular plates. The deflection thickness ratios obtained in theses experiments were 0.9-6. They measured the deflection time history by placing a condenser microphone near the centre of the plate. They also measured impulse using a ballistic pendulum. This enabled the deflection-time history and the impulse to be recorded simultaneously. Nurick [6] used a light interference technique to measure the time-deflection history during the deformation as the deflection thickness ratios obtained (4-12) were too large for the use of condenser microphones. This light interference technique was used to measure the time-deflection history in experiments on fully clamped circular and rectangular plates [7,8].

Experimental work by Menkes and Opat [9] found three distinct modes for the deformation of beams under uniformly distributed impulsive loads. These modes have since been found to be valid for plates as well [10]. According to the magnitude of the impulsive load, the plates will deform and fail in one of these modes. The modes presented by Menkes and Opat are:

Mode I	Large inelastic deformation;
Mode II	Tearing (tensile failure) of the material at the support;
Mode III	Transverse shear failure of material at the supports.

2.1.2 Recent Experimental Studies

a) Experimental Method

The experiments carried out in refs [10- 14] all use very similar experimental techniques for mounting the sheet explosive and measuring the impulse and will therefore be described at this point before presenting the experiments.

The sheet explosive was attached to a foam pad that was attached to the surface of the plate to be blast loaded. Figure 2.1. shows two loading configurations for fully clamped plates and Figure 2.2 shows the configuration for built-in plates. In all cases the detonation was at the centre of the disk of explosive.

Figure 2.1 Fully clamped plates with (a) loading over entire plate, (b) central loading.

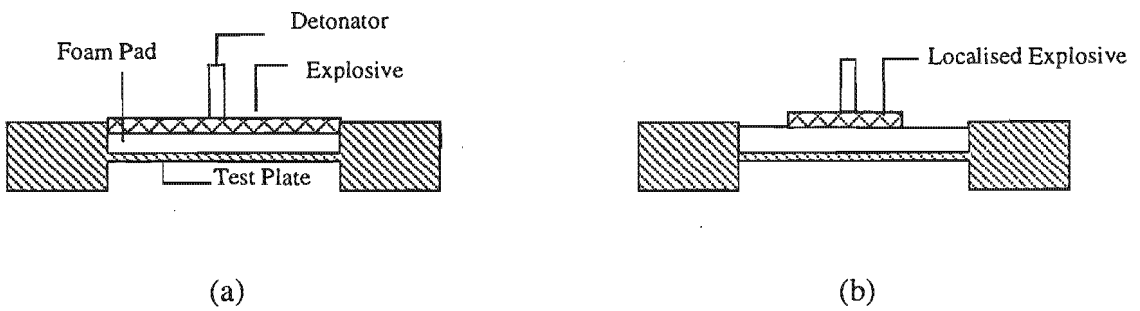

Figure 2.2 Built-in plate with (a) loading over entire plate, (b) central loading.

A ballistic pendulum was used in all the experiments to measure the impulse. The force of the explosion displaces the pendulum and this displacement is recorded. The impulse is then calculated knowing the mass of the pendulum.

b) Uniform Loading

Teeling-Smith and Nurick [10] carried out experiments on fully clamped plates with uniform loading over the plate. The impulse was increased over the range of tests so as to obtain all the deformation modes of Menkes and Opat [9]. The three modes of deformation were found to be applicable for explosively loaded plates. In mode II and mode III failure, where complete tearing occurred, the velocity of the disk was obtained using two fuse wires that were broken by the disk as it pulled away from the plate. The impulse, deformation and disk velocity were then used in energy balance calculations.

c) Boundary conditions

A comparison of the mid-point deflection and profiles of built-in and fully clamped plates was performed by Thomas and Nurick [11]. It was noticed that for mode I deformation, the deformation appeared to be independent of fixation conditions. For Mode II failure however it was found that deformation and failure were highly dependent on boundary conditions.

Nurick, Gelman and Marshall [12] carried out further experiments to determine the effect of boundary fixation on the onset of necking and failure. These experiments use sharp edged and rounded clamps and illustrate how sharp boundaries indent the plates and induce necking. It was found that the onset of necking was retarded by as much as 87% when a 3.2mm edge radius was used on the clamp. It was found that the impulse needed to be increased by 15% from about 22 to 25.25 in order to produce mode Ib failure (defined below).

Nutick *et al.* [12] extended the modes of Menkes and Opat to describe their observations of boundary failure:

Mode Ia Large inelastic deformation with no necking at the boundary

Mode Ib Large inelastic deformation with necking around part of the boundary

Mode Ic Large inelastic deformation with necking around all of the boundary.

d) Central Localised Loading

Nurick and Radford [13] performed a series of experiments on clamped plates with a localized central blast load. Explosive diameters of 18mm, 25mm, 33mm, 40mm were used on 100mm diameter 1.6mm thick plates. The applied impulse was varied to give a range of deflection responses. It was found that a new mode of failure occurred for central loading i.e. necking and tearing at a cap in the central region of the plate. Nurick and Radford found that capping does not occur for loading diameters of greater than 40mm. Further additions were made to the deformation modes of Menkes and Opat to account for cap failure:

Mode Itb Large inelastic deformation with thinning at central area:

Mode II*c Partial tearing at central area

Mode IIc Complete tearing at central area

Chung Kim Yuen [14] carried out experiments on built-in plates with 1.6mm, 2.6mm, 3.6mm thicknesses. These plates were loaded with varying impulses and over 25mm, 33mm, 40mm loading diameters. These tests showed that at smaller load diameters, a higher impulse was required for failure. The trend in tearing pattern did not appear to change with plate thickness. Petalling after failure at the cap was observed in plates with very high impulses. Petalling failure is defined as the tearing of the plate parallel to the radius of the plate. The experiments performed by Chung Kim Yuen are discussed further in chapter 3.

2.2 Theoretical Analysis of Impulsively Loaded Plates

2.2.1 Mid Point Deflection

There are many theoretical models describing the dynamic response of circular plates recorded in the literature. They are based on differing assumptions that results in each model giving adequate predictions only over specific ranges of load, thickness and deflection-thickness ratio. Nurick and Martin [15] present a review paper of many of these theoretical models. Nurick and Martin use a dimensionless damage number and the deflection-thickness ratio to compare the theoretical models.

Nurick and Martin [15] report that the first theoretical models by authors such as Hudson [16] and Wang [17] considered only bending effects and ignored the membrane effects. This resulted in these models being limited to plates with small final deformations (less than 2 plate thicknesses). Other authors such as Boyd [18] and Frederik [19], considered just the membrane effects and discovered that these methods give reasonable predictions of true behaviour at larger deformations (3-7 plate thicknesses).

a) Membrane Mode Methods

Martin [20] and Martin and Symonds [21] were the first to use membrane mode approximation solutions with rigid plastic material behaviour to predict the deformation of plates under impulsive loads. These methods were used to solve the exact solutions of Lee and Symonds [22] and Hopkins and Prager [23]. Originally the membrane mode approximation technique was used only for small deflections.

Guedes Soares [24] took the analysis of Martin and Symonds [20] used for small deflections (deflection thickness ratios of less than 2) and extended it for finite displacements. Guedes Soares [24] was able to do this as it was noticed that the mode shape did not change significantly during the response of the plate. Guedes Soares thus formulated the following theoretical model for midpoint deflections:

$$W_f = \left(\frac{0.0681 I^2}{t^2 R^2 \rho \sigma_0} + I^2 \right)^{\frac{1}{2}} - t \tag{2.1}$$

The dimensionless form of the deflection thickness ratio is given as:

$$\frac{W_f}{t} = (0.673\phi^2 + 1)^{1/2} - 1 \tag{2.2}$$

Symonds and Wierzbicki [25] calculated the mode shape by solving a linear eigenvalue problem. The solution of Symonds and Wierzbicki accounted only for membrane effects, as a result of this their predictions tended to underestimate deflections for small deflections. For large deflections, where the energy dissipated in the membrane effect is significant, the predictions are well supported by experimental results. The theoretical model of Symonds and Wierzbicki is as follows:

$$W_f = 1.0186t \left(\frac{2\rho V_0^2 R^2}{3\sigma_0 t^2} \right)^{\frac{1}{2}} \tag{2.3}$$

and

$$\frac{\delta}{t} = 0.666\phi \tag{2.4}$$

Jones [26] includes both membrane and bending effects in a theoretical model. Jones considers two phase of motion of the plate, the first is the response during the loading of a square pressure pulse for time the second phase is the inertia response. The theoretical model predicted by Jones is as follows:

$$W_f = t \left[\left\{ 1 + \frac{2\lambda}{3} \right\}^{\frac{1}{2}} - 1 \right] / 2 \tag{2.5}$$

where $\lambda = \mu V_0^2 R^2 / M_o t$

Jones [26] then simplified equation 2.5 for membrane effects only but included a strain rate sensitivity term for large deformations of strain hardening materials. The theoretical model which predicts the response for strain rate hardening materials is shown in equation 2.6:

$$W_f = t\left(\frac{2\rho V_0^{\,2} R^2}{3n\sigma_0 t^2}\right)^{\frac{1}{2}} \tag{2.6}$$

where $n = 1 + \left\{\frac{V_0 W_f}{3\sqrt{2}DR^2}\right\}^{\frac{1}{q}}$ (2.7)

and D and q are the strain rate sensitivity constants.

Nurick *et al.* [7] used an iterative solution where the mode shape was made to vary at each time step as the geometry of the deforming plate changed. The approach was essentially the same as that of Symonds and Wierzbicki [25] except that the mode shapes were recalculated at each time step. This mode shape is defined as:

$$u = u_c \phi \tag{2.8}$$

ϕ = mode shape recalculated at each time step

u_c = midpoint displacement.

This approach was compared to the predictions of Symonds and Wierzbicki [25], Perrone and Bhadra [29], Duffey [27] and Guedes Soares [24] and found to give better correlation with experimental results.

The approach above was extended by Nurick *et al.* [8] to include in plane deformations. This method assumes that a point on the surface of the plate moves perpendicular to the surface in its position at that particular time step and not perpendicular to the undeformed surface as other predictions assume. This model tends to predict slightly larger displacements than that of the model using transverse displacements only. This model

predicts a radial strain distribution which compares adequately with the measured strain profile. It predicts the maximum strain at the centre of the plate and lower strains towards the boundary.

b) Energy Methods

Nurick and Martin [15] report that Duffy [27] and Westine and Baker [28] used simplified energy approaches in which the kinetic energy imparted was equated with strain energy stored in the deformed system. Westine and Baker assumed a sinusoidal deformed shape and Duffey used polynomial and sinusoidal forms which were fitted to experimental data. Duffey used the following energy equation to define the energy of deformation:

$$E_{def} = \pi t \int_0^R \frac{\sigma_0'}{\left(1-\nu+\nu^2\right)^{\frac{1}{2}}} \left(\frac{\partial w}{\partial r}\right)^2 r dr \tag{2.9}$$

where $w = w_0 \gamma(r)$ with $\gamma(r)$ being the shape function
and w_0 the mid point deflection

And calculated the midpoint deflection to be

$$W_f = \frac{0.242 I (1-\nu+\nu^2)^{\frac{1}{2}}}{tR(\rho\sigma_0)^{\frac{1}{2}}} \tag{2.10}$$

and

$$\frac{\delta}{t} = 0.761\phi(1-\nu+\nu^2)^{1/2} \tag{2.11}$$

Perrone and Bhadra [29] used an energy approach that accounted for plastic rate sensitivity with large deformations. They also simplified the system by ignoring circumferential and bending effects, considering just the membrane effects. In the

procedure the authors used the energy balance between the input kinetic energy of the impulse and plastic work done by the stretching of the system. These predictions correlated well with experimental evidence. The mid point deflection prediction was given by:

$$W_f = \frac{0.212I}{tR(\rho\sigma_0)^{\frac{1}{2}}} \tag{2.12}$$

and

$$\frac{\delta}{t} = 0.368\phi \tag{2.13}$$

Teeling-Smith and Nurick [10] used experimental data for mode I and mode II deformations to find a best-fit curve of deformation energy. This best-fit curve was then equated with the kinetic energy input in the same manner as Duffey [27]. The kinetic energy of the ruptured disc was also recorded and was considered in the energy equation. Teeling-Smith and Nurick were thus able to predict an energy required for the transition to mode II and mode III deformations.

c) Deformation of Centrally Loaded Plates

Wierzbicki and Nurick [30] considered the deformation of plates loaded with a central localized load. In order to provide a simple usable solution, Wierzbicki and Nurick assumed that the final deformation is larger than several multiples of plate thickness and that the material particles move in a transverse direction only. The plate material is further assumed to be rigid-perfectly plastic, however the flow stress can be adjusted for strain hardening and strain sensitivity

Wierzbicki and Nurick divided the deformation of the plate into two distinct phases. The motion of first phase was governed by plastic wave theory and the second phase was studied using the mode approximation techniques of Symonds and Martin [20]. Figure 2.3a shows these two phases of deformation. Phase I shows a central bulge of

approximately the same radius as that of the loading. Phase II motion is characterized by the constant shape of the velocity, displacement and acceleration profiles. The final deformation profile is found by summing the contribution of the two phases (Figure 2.3 b):

$$\overline{w}_f(\overline{r}) = \overline{w}_I(\overline{r}) + \overline{w}_{II}(\overline{r}) \tag{2.14}$$

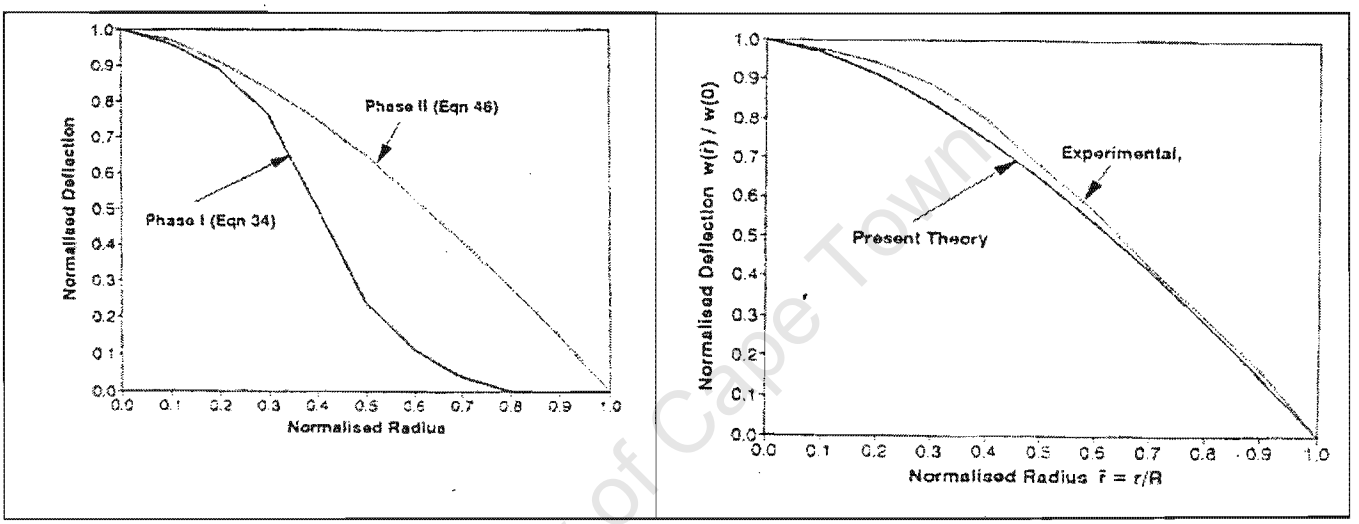

Figure 2.3 Deformation of centrally loaded plate. [30] a) Phases of motion, b) Combined deformation

Wierzbicki and Nurick [30] noted that there are two distinct failure modes, the first is the formation of a disc at the centre of the plate and the second is a tearing failure at the clamped edge. The authors hope that this model would eventually lead to precise calculation of strains within the material in order to predict the onset of necking and failure. Wierzbicki and Nurick noted a difficulty in assuming the initial pressure distribution and hence the initial velocity profile. This will receive further attention in the next section.

2.2.2 Loading Conditions

Due to the short duration and very large forces of the explosion, the exact initial loading conditions of sheet explosive loaded plates is not known. The understanding of exactly how the plates are loaded is necessary for any reliable theoretical prediction. Plates with central localized loads are most affected by this problem. Various assumptions and predictions have been made, some of which will be discussed here.

Wierzbicki and Nurick [30], showed that the shape of the initial velocity shape profile (a function of loading pressure) had an important effect on the predictions of phase I deformation. They proposed the use of various velocity profiles. The proposed profiles were a central constant velocity with either a linear or an exponential decay radially outwards. A continuous profile was also proposed.

Radford et al [31] used a step-wise velocity field, assuming that the explosive burns as a set of discretised rings spreading outwards. Cubic shape functions are used to define velocity fields for each step. Using this method Radford et al were able make predictions of final deformation shapes of the blast loaded plate and found correlation with experimental results to within two plate thicknesses.

Loading the plate using constant central pressure load with exponential decay was found by Bimha [32] to give fairly accurate loading conditions. The loading profile is shown in figure 2.4.

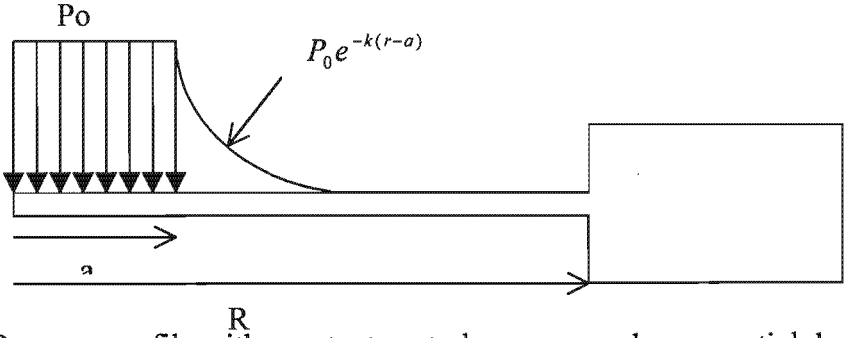

Figure 2.4 Pressure profile with constant central pressure and exponential decay.

A constant pressure Po was found such that integrating the pressure over the surface of the plate would give the measured impulse. The impulse was found from the pressure using the following equation:

$$I = t2\pi\left[\int_0^a P_0 dr + \int_a^R P_0 e^{-k(r-a)} dr\right] \tag{2.15}$$

The exponential constants k for a load radius to plate radius ratios were calculated by comparisons with experimental data by Bimha [32]. Bimha proposed the following empirical relationship for calculating the exponential constant.

$$k = 130 - 261\left(\frac{a}{R}\right) + 948\left(\frac{a}{R}\right)^2 \tag{2.16}$$

Grobbelaar [33] used the ABAQUS finite element code to model the explosion using the equation of state for explosives. The explosive elements deform as the pressure within them increases. The plate is loaded as the explosive elements come into contact with it. Good preliminary results have been reported and the model shows satisfactory correlation with experiments results of Radford [31].

2.3 Numerical Analysis on Impulsively Loaded Plates

Olson *et al.*[48] used a dedicated code to predict the response of square plates. The code used Kirchhoff thin plate theory and included geometric and material non-linearity. Mode I predictions were found to be accurate. For Mode II predictions, the high local strains at the boundary were modelled using hinge lines. Failure was modelled using a rupture strain based model. Good predictions of mode II failure were made.

Farrow *et al.*[35] used the general purpose ABAQUS finite element code to model circular plates loaded over the entire surface. Farrow *et al.* also used Kirchhoff thin plate elements and both implicit and explicit solution schemes. The explicit scheme was found to be computationally less time consuming. Uniform and triangular initial velocity profiles were used. The material was modelled using the von Mises yield criterion with isotropic hardening and Cowper-Symonds strain rate sensitivity. Predictions were made of the deflection profile and the stress and strain through the plate and found to compare satisfactorily with experimental data.

Gelman [12,34] used ABAQUS to model plates loaded over the entire surface continuing the work done by Farrow *et al.* The main aim of this analysis was to model the effect of boundary fixation conditions on deformation and failure. An explicit solution scheme and axisymmetric elements were used. Gelman found that fixation conditions had little effect on the mode I response but had a significant effect at high impulses where failure occurred at the boundary. The model was found to give good predictions of the strain through the plate and the plate thinning. A material rupture model based on equivalent plastic strain was used to try and model mode II failure but correlation with experimental data was found to be poor. Gelman recommended that more reliable parameters be obtained for the failure model and that the effect of strain rate on these parameters should be ascertained.

Gelman [34] considered the effect of the fillet radius at the boundary of fully built-in plates. It was found that a sharp boundary with no fillet caused stress concentrations at the boundary of the plate where a smooth fillet reduced the stress at the boundary considerably. Figure 2.5 shows the strain contours of the plate at the boundary and it can be seen that the strain is significantly higher at the boundary with no fillet radius.

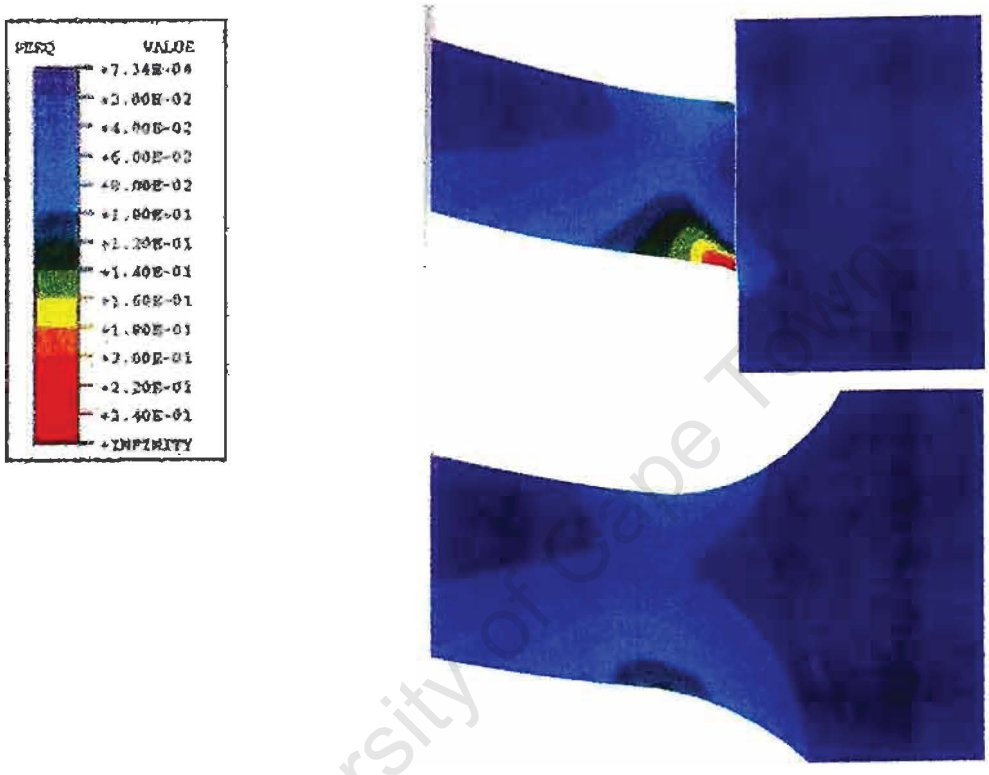

Figure 2.5 Comparison of the strain at the boundary of a built-in plates with and without a fillet radius. [34]

2.4 Necking and Failure

2.4.1 Theory of Necking

Rajendran and Bless [36] report that necking was first observed by Considere in 1885. It was observed in a conventional tensile test that an instability occurred at maximum load because the increase in strength due to strain hardening cannot compensate for the increase in stress caused by a reduction in area. Most of the plastic deformation takes place in the localized region as the neck develops.

Hill [37] considered the necking of thin sheets and noted '.. for a localized neck to be able to develop ... the hardening produced by the first increment in strain in the incipient neck should not be so great as to inhibit its immediate development and cause deformation only to continue elsewhere.'

As a result of necking, uniaxial stress-strain data obtained from tensile tests is not valid beyond the necking point. This is because the stress required to continue the straining of the material decreases due to the change in area at the point of necking. Bridgman [38] developed an analytical expression in order to obtain the effective stress and strain in the necked region. 'Bridgman Analysis' uses geometric dimensions of the necked region to relate effective stress and strain to the measured values. Rajendran and Bless [36] used finite element modeling to extend the Bridgman analysis for use at very high strain rates with the split Hopkinson Bar. Using these methods, stress strain data could be obtained to over 70% strain.

The problem of necking under combined tension and bending was considered by McClintock *et al.*[40]. This is relevant to the failure of plates at their restrained boundaries as a combination of bending and tension occurs there. McClintock *et al.* found that bending decreases the magnitude of tension required for tensile instability (necking). It was found that for a radius of curvature of greater than the order of the thickness,

bending decreased the tensile necking force by 7-17%. This analysis was performed for materials with power-law kinetic hardening. For isotropic hardening material, the allowable curvature would be lower.

2.4.2 Ductile Failure – Microscopic consideration

On a microscopic scale most structural material fails by a process known as microvoid coalescence (Ewalds and Wanhill [39]). This process is shown in figure 2.6. Microvoids form at internal discontinuities such as grain boundaries, intermetallic particles and precipitates (a). Under loading, the voids grow as the local stress increases (b), then coalesce (link) (c + d) and finally a continuous fracture surface is formed.

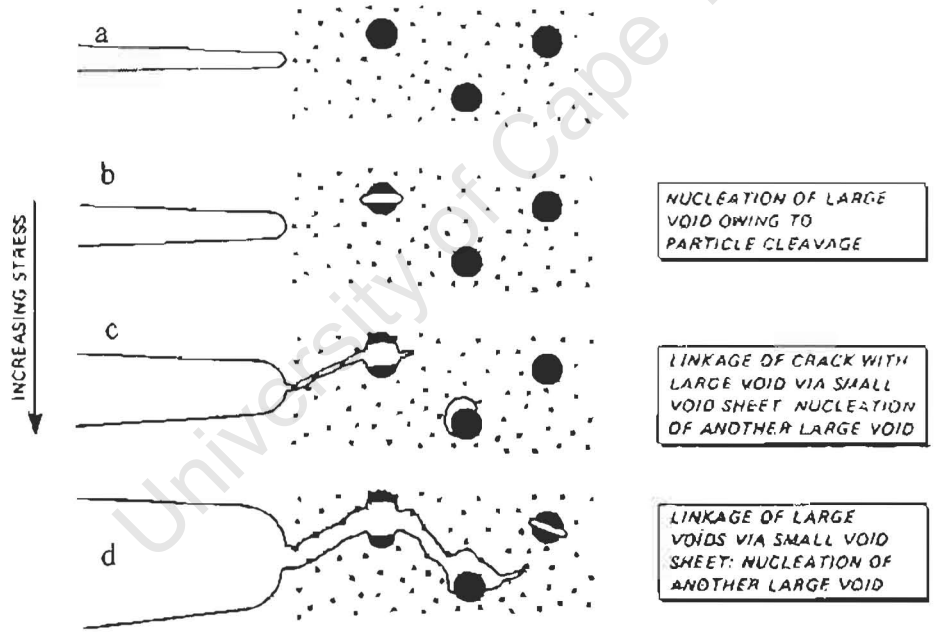

Figure 2.6 Crack growth due to microvoid coalescence [39]

This process results in a dimpled appearance of the fracture surface. Figure 2.7a shows an example of a dimpled failure surface with both small and large dimples. On a macroscopic level, the failure appears dull and contraction (necking) may be visible.

The exact appearance of the ductile failure surface is dependant on the type of loading that caused the failure. Figure 2.8b shows the effect of loading on the fracture surface. For uniaxial tension, the voids will be symmetrical. Failure caused by shear loading will cause parabolic shaped dimples which are in the opposite direction on the opposite fracture surface. Tensile tearing will result in parabolic dimples which are reflected on the opposite surface.

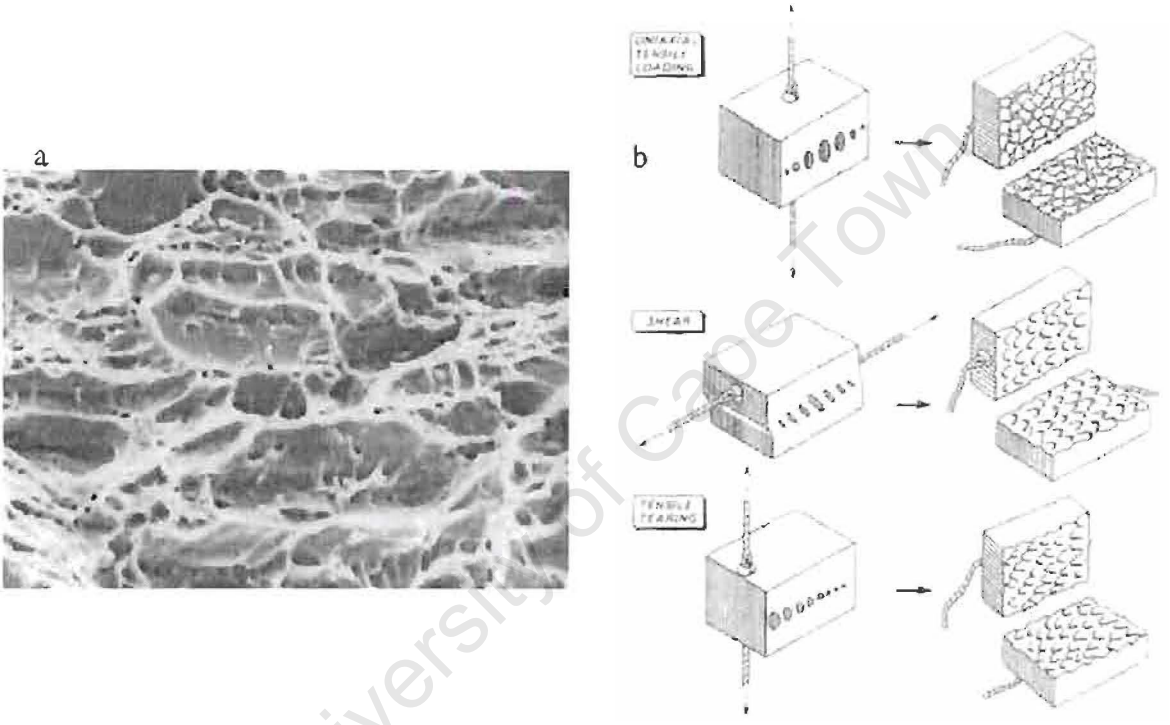

Figure 2.8a) Micrograph of a dimpled fracture surface, b) Schematic drawing of dimple formation due to various types of uniaxial loading. [39]

2.4.3 Damage Mechanics

Recent developments in the area of understanding and predicting necking and failure have centered mainly on the field of damage mechanics. The theory of damage mechanics is based on defining an internal damage variable of the material based on the void growth within the material. Varying approaches to the subject are presented by

Gurson [41], Lamaitre[42], Becker *et al* [43], Needleman and Tvergaard [44]. These authors deal with topics of flow localization, stress triaxiality and void growth to failure.

Two of the classic theories of damage mechanics are those of Gurson [41] and Lamaitre [42]. Gurson defined a damage variable D as the void volume fraction, where D = 1 corresponds to the sound (undamaged) material and D = 0 to the fully damaged state with complete loss of load carrying capacity.

Lamaitre defined a damage variable D_s:

$$D_s = \frac{S - \tilde{S}}{S}$$

where S is the total cross sectional area and $\tilde{S}$ is the load carrying area. In this case D_s=0 corresponds to the undamaged state and D_s=1 corresponds to rupture of the material element. For a more complete description of the two models and their numerical implementation see de Souza Neto *et al.*[45].

2.4.4 Predictions of Plate Failure

Jones [46] considered the mode II failure of beams as described by Menkes and Opat [9]. This analysis continued on the work done on the dynamic response of a fully clamped beam subjected to a uniformly distributed pressure pulse. Jones calculates the total tensile strain in the plastic hinge at the support in terms of the mid-point deflection as:

$$\varepsilon_m = 2\{(W_f / H)^2 + L/H - 1\}(H/2L)^2 \qquad (2.17)$$

If ε_m were set to be the strain at which the material failed in a tensile test, the initial velocity impulse for failure would be given by:

$$V_0 = 2\left[1+(2)^{\frac{1}{2}}\left\{2+\varepsilon_m(2L/H)^2-2L/H\right\}^{\frac{1}{2}}\right](H/2L)(\sigma_0/\rho)^{\frac{1}{2}}/3^{\frac{1}{2}} \qquad (2.18)$$

This method does give reasonable agreement with the experimental work of Menkes and Opat [9]

Nurick and Teeling-Smith [47] considered the failure of circular plates and Olson *et al.*[48] the failure of square plates. They used experimental data to predict the onset of necking and failure in plates loaded over the entire surface. It was found that in some cases failure would occur at a particular impulse while at slightly higher impulses no failure would occur. This made predictions of impulse to failure difficult. Nurick and Teeling-Smith found that failure occurred in the range of deformations of 17-18 plate thickness. Olson *et al.* predicted rupture strains of 0.204 - 0.3 and that high strain rates lowered the failure strain. Strain localization was not considered by Olson *et al.*

Shen and Jones [49] used an energy density failure criterion to predict mode II and mode III failure. This method used the total plastic work at the support and the plastic strain through the membrane to calculate a value for the total dimensionless plastic work per unit area. The strain energy density for failure was then calculated from tensile stress strain data. The total dimensionless plastic work per unit area and the strain energy density criterion were then compared and a failure prediction was made. The predictions made for critical impulse to failure were found to be poor when compared to experimental results of Teeling-Smith and Nurick [10]. This discrepancy was thought to be as a result of the boundary conditions not being adequately considered by the failure model.

2.4.4 Grain Elongation in the Study of Failure Strain

A new method for estimating failure strain was developed by Ohashi [50]. The method was able to provide an accurate estimate of fracture strain. The procedure was as follows: A metallographic study was performed of a polished and etched surface through the cross section of the fracture surface. The average aspect ratio of the grains immediately below the fracture surface were measured (as shown in figure 2.9a). These measurements were then calibrated using a calibration curve that was established by measuring the plastic strain using a detailed metallographic examination. Once calibrated, the method was used to estimate the fracture strain of notched specimens and was found to give accurate predictions.

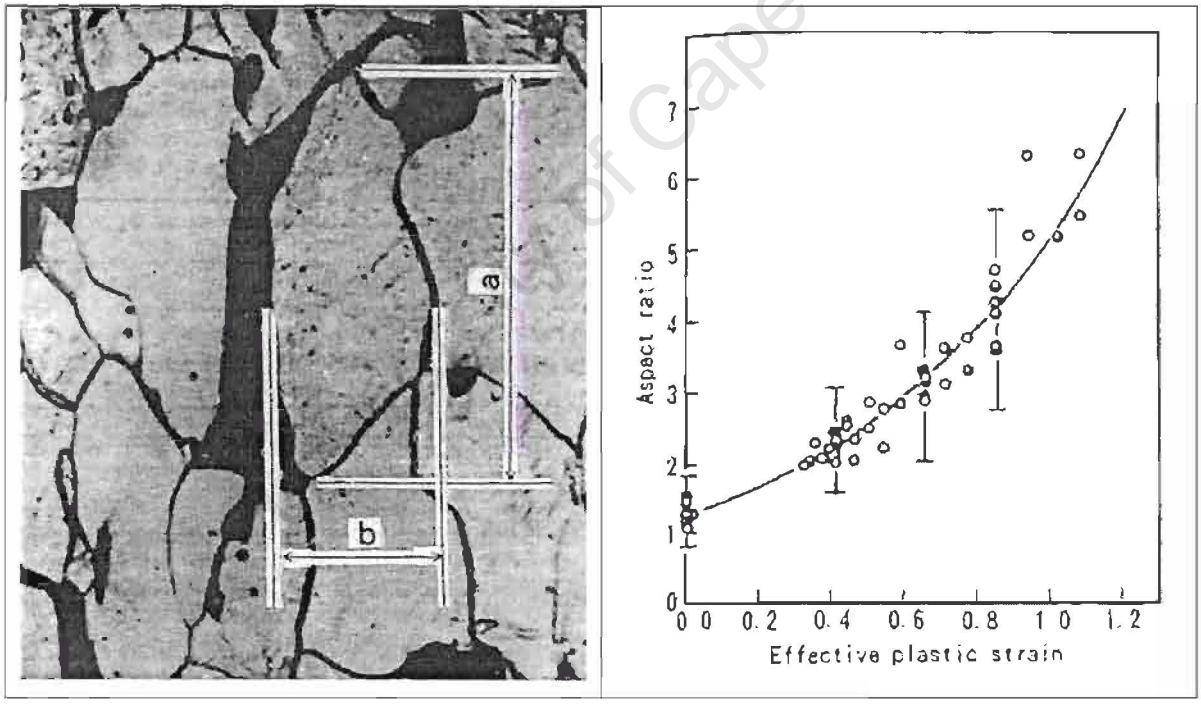

Figure 2.9 a)Grain aspect ratio Measurement, b)Calibration curve to relate aspect ratio to plastic strain. [50]

Nurick *et al.* [12] showed through microstructural analysis of uniformly loaded plates that the normalized grain elongation was highest at the boundary and centre. Correlation was observed between modes of failure and areas of highest grain elongation. Their analysis was of a qualitative nature with observing trends being the emphasis of the study.

The work described in this thesis extends the work discussed hence by using the grain elongation to determine the local strains and thus aid the understanding of the deformation and failure processes within plates subjected to central, blast loads.

CHAPTER 3

METHOD OF METALLOGRAPHIC ANALYSIS

3.1 Preparation and Blast Loading of Plates

The plates that are analyzed in this study were taken from experimental tests undertaken by Chung Kim Yuen [14]. In these experiments, built-in plates of 1.6mm, 2.6mm and 3.6mm thickness were blast loaded. The explosive loading was applied locally at the center of the plate with loading diameters of 25mm, 33mm and 40mm. A total of sixty plates were tested. For the purpose of this study, fifteen plates were chosen. Only plates with a loading diameter of 33mm were studied using 5 from each of the three plate thicknesses.

3.1.1 Preparation of the Undeformed Plates

The built in plates were machined from a 20mm thick and approximately 200mm square mild steel plate. A circular region was machined out from the centre of either side of the plate leaving a plate of the appropriate thicknesses (1.6mm, 2.6mm and 3.6mm) in the centre. After machining, the plates underwent a normalising heat treatment to relieve residual stresses and provide an equiaxial grain structure.

3.1.2 Loading of the Plates

The plates were bolted to a ballistic pendulum in order to facilitate the measurement of the impulse. The plates were then centrally loaded using a plastic explosive (PE 4). The mass of the explosive was measured and the explosive was shaped into the appropriate size disc and attached to a foam polystyrene pad (see fig. 3.1). The detonator is placed at the center of the disc with a 1g pig-tail of explosive. The pad of 12mm thickness is fitted to the plate. The foam pad disintegrates on detonation. It attenuates the shock transmitted to the plate, provides a uniform impulse and prevents spalation of the specimen. The explosive has an approximate burn speed of 7500m/s.

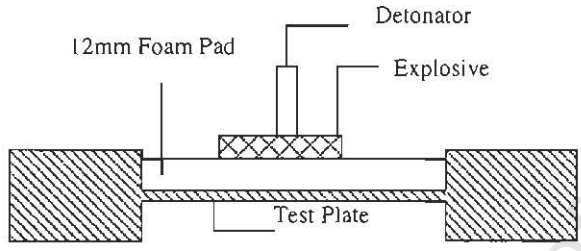

Figure 3.1 Plate and loading configuration

3.1.3 Measurements Taken During Experimentation

During each of the blast tests, the following measurements were taken:

Impulse: The impulse, the measure of the magnitude of the load, was measured by measuring the displacement of the ballistic pendulum.

Mid-point deflection: The deflection of the midpoint of the plate from its initial position.

Burn diameter: The diameter of the area on the loaded side of the plate discoloured by the explosive.

Cap diameter: The size of the blown out fragment of the plate when cap failure has occurred.

Point of inflection diameter: The point on the radius of the plate where change of curvature occurs.

A summary of these measurements for the plates studied is given in Appendix I.

Photographs were taken of the deformed plates. The deformation profiles of the deformed plates can be seen in figure 3.2.

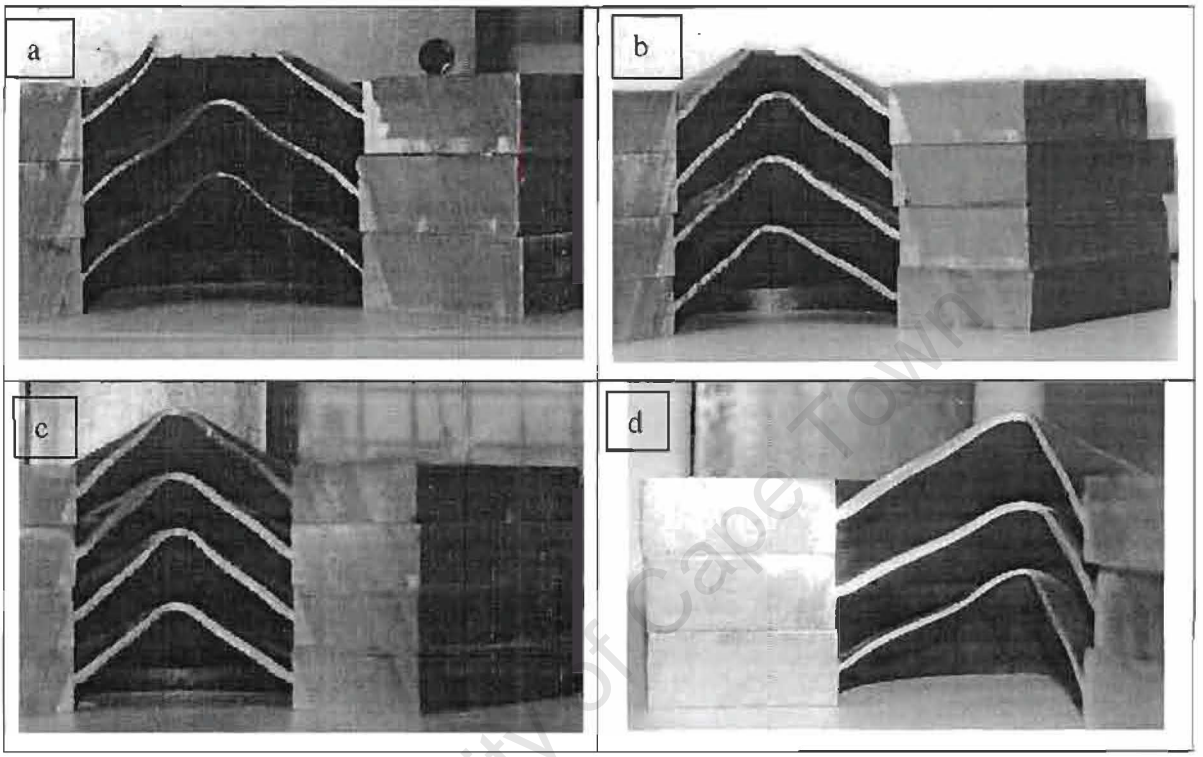

Figure 3.2 Deformed plate a)1.6mm plate b)2.6mm plate, c)3.6mm plate d)plate thinning at boundary – all three thicknesses

	a	b	c	d
Thickness (mm)	1.6	2.6	3.6	1.6, 2.6, 3.6
Impulse (Ns)	8.8 – 10.8	12 – 19.5	15.8-34.2	9.5, 16.9, 21.4
Deflection (mm)	24.5 (unfailed)	20.1-28.1 (unfailed)	20 – 28.9 (unfailed)	24.7, 28, 26

3.2 Specimen Preparation

Fifteen plates were selected from the experiments performed by Chun Kim Yuen [14]. From each plate a specimen was cut, first across the plate radius and then the radial sections were cut into specimens approximately 20mm in length in order to mount. The positions of the cuts are shown in figure 3.3. The plate sections were then hot pressure mounted in a polymer resin.

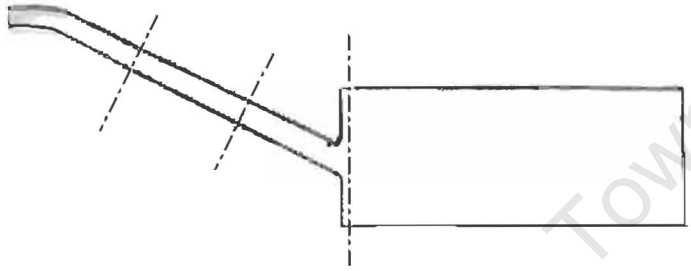

Figure 3.3 Position of cuts before mounting

Once mounted, the specimens were ground and polished to a .25µm finish. The polished surface was etched using a 2.5% nital solution. The specimen was held in the solution for approximately 5 seconds. An example of the polished and etched surface as seen under a scanning electron microscope is shown in figure 3.4.

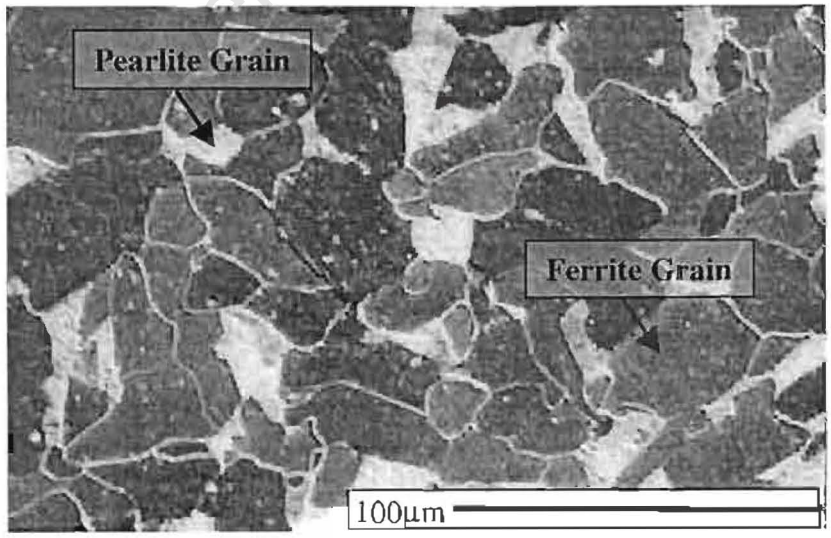

Figure 3.4 Polished and etched surface of a specimen.

The specimen mount was pasted to an aluminum stub and conductive silver paint was used to connect the surface of the plate specimens to the stub to allow conduction. Finally the top surface of the specimen was gold palladium coated to further aid conduction and increase resolution when the surface was examined under the microscope. A grid was pasted to some of the specimens in order to allow for tilt correction in the scanning electron microscope (this will be discussed further in the next section).

3.3 Microscopy

All the microscopy performed in this study was done using the Cambridge S220 scanning electron microscope of the University of Cape Town's Electron Microscopy Unit.

An accelerating voltage of 15 kV was used at all times. The secondary electron detector of the microscope was used to obtain the images. The specimen is inserted in the specimen holder and the tilt angle is set to 35 degrees to tilt the specimen towards the secondary electron detector. This is done to improve resolution and reduce shadowing. As a result of the foreshortening effect due to the tilt angle, the tilt correction must be set in order to give accurate dimensions [51]. This is done by attaching a copper microscopic grid to the sample and adjusting the tilt correction control until the grid is symmetrical (figure 3.5 shows a micrograph of the grid).

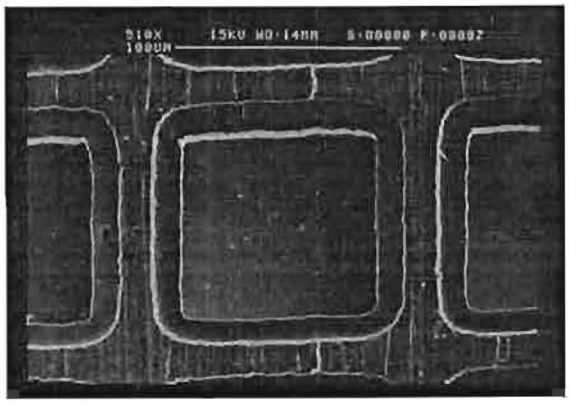

Figure 3.5 Grid used to calibrate the tilt correction

Micrographs were taken at various points over the radius of the plate at approximately 4mm intervals and at areas of interest such as cracks and bends. Between 14 and 22 micrographs were taken per plate. The micrographs taken for the purpose of quantitative analysis were all taken at approximately 500 times magnification. Additional micrographs of failure surfaces were taken at higher magnification. The photographs were taken at a resolution setting of 8 and with a 50 second photograph scan.

3.4 Data Capture

The micrographs needed to be analyzed to give quantitative data of aspect ratio, orientation and area for each grain. This was done using a Joyce-Loebel Image analyzer controlled by JLGENIAS software.

In order to facilitate recognition of grain boundaries, each micrograph was traced so that only grain boundaries of the ferrite grains are shown (an example of a micrograph and trace is shown in figure 3.6).

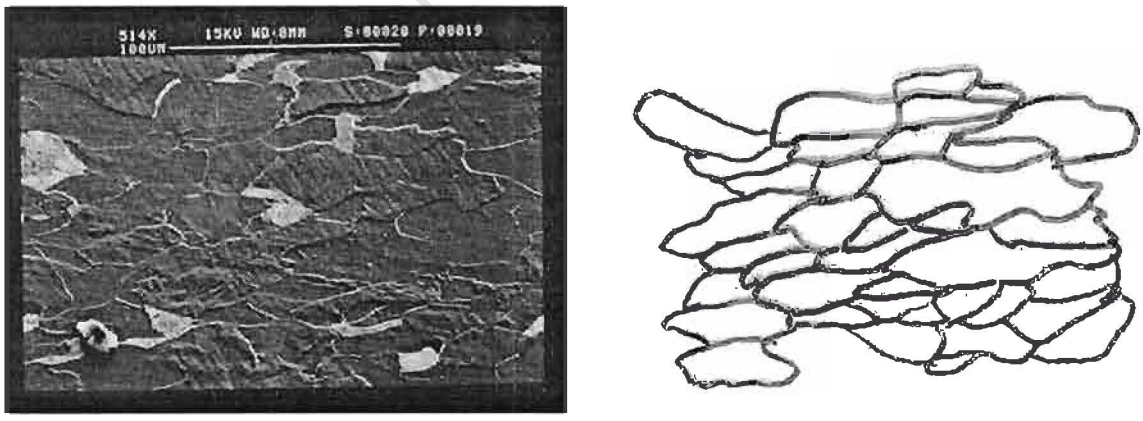

Figure 3.6 a)Micrograph showing grain structure and (b) Trace of ferrite grains

After the image had been captured, the software was used to make measurements of various dimensions of the grains. There were between 40 -70 grains per micrograph that were each measured separately by the computer. The dimensions that were measured

were; area, length, breadth and orientation. The length is defined as the maximum feret diameter across the grain (ϕ max), the breadth is the shortest feret diameter (ϕ min)and the orientation is the angle (γ) of the largest ferret diameter [52]. These dimensions are shown in figure 3.7. The dimensions the grains of each micrograph were stored to separate ASCII files for analysis.

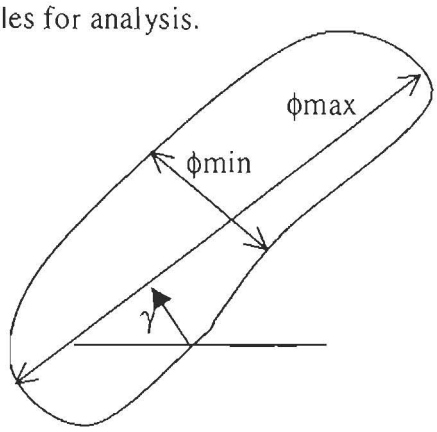

Figure 3.7 Grain dimensions

3.5 Data Analysis

The data pertaining to the grain dimensions of each micrograph had to be processed to provide average grain aspect ratios which were meaningful for further analysis. As each micrograph represented a particular material point an average value of grain aspect ratio was required for each micrograph to enable comparisons between each point.

The virgin (undeformed) material had a completely random grain structure. For the analysis, an initial grain aspect ratio of 1 was required to represent the virgin state. The aspect ratio (length/breadth) could therefore not be averaged without considering the orientation of the grains. An algorithm was used which would sum the aspect ratio of grains that were orientated in a preferred direction and subtract those which were at right angles to that direction. This ensured that micrographs with randomly orientated grains had an average aspect ratio of approximately 1.

Conversely, micrographs taken at points in the material that had undergone deformation had average grain elongations of greater than one as the grains had elongated in a preferred direction.

In calculating the average grain aspect ratio, the contributions of each grain to the average was weighted according to area. This ensured that the larger grains whose deformations were most significant were weighted accordingly.

A program was written for MATLAB to perform this algorithm repetitively. The source code is given in Appendix V. The equation used to calculate the average grain aspect ratio is:

$$\alpha_r = \sum_n (\alpha_r^n - 1)\cos(2\times\gamma^n)\left(\frac{A_n}{\sum A}\right)+1 \qquad (3.1)$$

Associated with each grain are 3 properties; Aspect ratio, Orientation and Area. The variation of these properties from the mean or from the virgin state are considered in the following way:

- $(\alpha_r^n - 1)$ is the difference between the virgin state aspect ratio and the aspect ratio of the deformed grain.
- $\cos(2\times\gamma^n)$ is the orientation weighting of each grain where $\gamma'' = |\gamma_g - \bar{\gamma}|$ is the angle between the orientation of the individual grain and the average orientation of the entire micrograph. Grains parallel to the average have a weighting of 1 and grains perpendicular have a weighting of –1.
- $\left(\frac{A_n}{\sum A}\right)$ is the area weighting where A_n is the area of the individual grain and A is the total area of all the grains on the micrograph.

The product of these grain properties are summed for each micrograph as shown in equation 3.1.

CHAPTER 4

RESULTS OF METALLURGICAL STUDY

4.1 Theoretical Basis

The method of analysis as discussed in chapter 3 provides the average aspect ratio of the grains at any point in the material being analysed. A theoretical method was required to relate the aspect ratio to the strain. In order to verify this theory, tensile tests were performed in which the loading was arrested at various strains before necking occurred. The strain was therefore known and could be related to the grain aspect ratio.

The theoretical method assumes plane strain conditions[1]. This assumption is valid for the plates if motion is assumed to be in the transverse direction only as lateral motion would cause circumferential strains. Most of the theoretical plate deformation theories make the assumption that deformation is in the transverse direction only.

If the original grain structure is considered to be equiaxial, a grain representing the average grain in the undeformed condition can be considered as square with sides of length a_0.

[1] If three dimensional strains were to be considered, the grain elongation would need to be measured in two planes and the strain equation would need to include all the poison effects of strain in the circumferential direction.

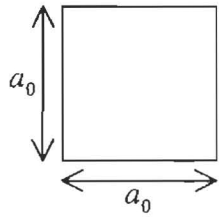

Figure 4.1 Undeformed grain

A grain in the deformed condition can then be considered as a rectangle with sides a_1 and b_1.

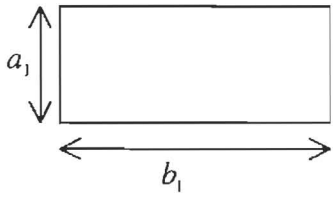

Figure 4.2 Deformed grain

If plane strain is assumed, then the thickness of the grain remains constant, then by constancy of volume, the area of the grain in the undeformed condition is the same as that in the deformed condition and thus:

$$a_0^2 = a_1 b_1 \tag{4.1}$$

As the strains considered in this study are large, the strains are considered as finite and hence logarithmic strains are used. The strain in the grain is then:

$$\varepsilon^{gr} = \ln\left(\frac{b_1}{a_0}\right) \tag{4.2}$$

The grain aspect ratio is defined as:

$$\alpha_r = \frac{b_1}{a_1} \tag{4.3}$$

Rearanging these three equations, to relate aspect ratio to strain gives:

$$\varepsilon^{gr} = \frac{1}{2}\ln(\alpha_r) \qquad (4.4)$$

or $$\alpha_r = e^{2\varepsilon^{gr}} \qquad (4.5)$$

This relationship (eqn. 4.5) is plotted below and shows how at higher strains, a small increase in strain causes a large increase in aspect ratio. The complete derivation of the equation is given in appendix II.

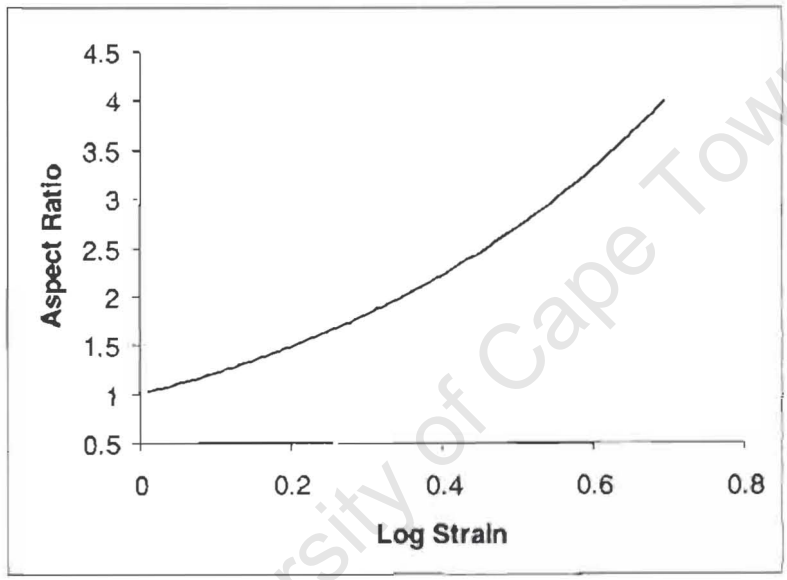

Figure 4.3 Theoretical relationship between aspect ratio and strain

4.2 Tensile Tests

A series of tensile tests were carried out in which the specimens were extended to a specific amount of strain and then the tests were stopped. Four tests were stopped before necking, one was stopped after necking and one was stopped after failure. The overall strain was measured and then the specimens were sectioned for microstructural analysis. The grain aspect ratio was measured at six points on the plane of the section using the method described in chapter 3.

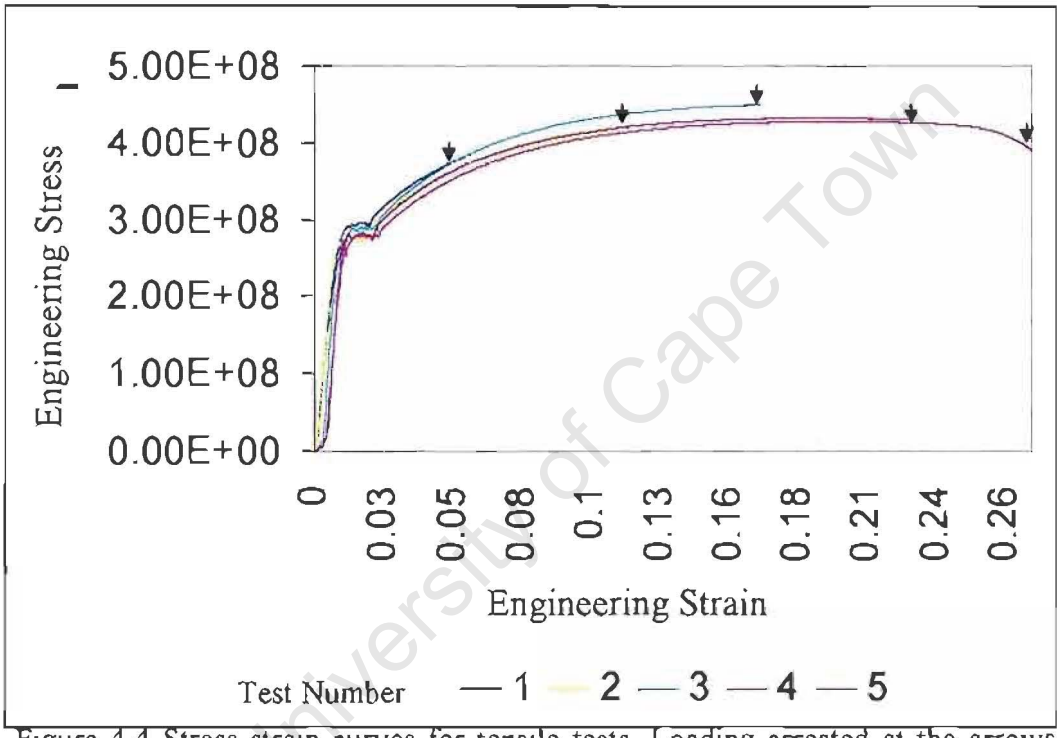

Figure 4.4 Stress strain curves for tensile tests. Loading arrested at the arrows. Overall strain: 1) 0.046, 2) 0.105, 3) 0.174 4) 0.234, 5) 0.272. Arrows mark where the tests were arrested.

The six aspect ratios measured from the micrographs for each of these tests were plotted against the overall strain measured. The strain is constant across the specimen before necking as strain hardening causes the strain to increase evenly through the specimen. These results are plotted in figure 4.5. The relationship of equation 4.5 is plotted for comparison. All of the tensile test data is given in Appendix III.

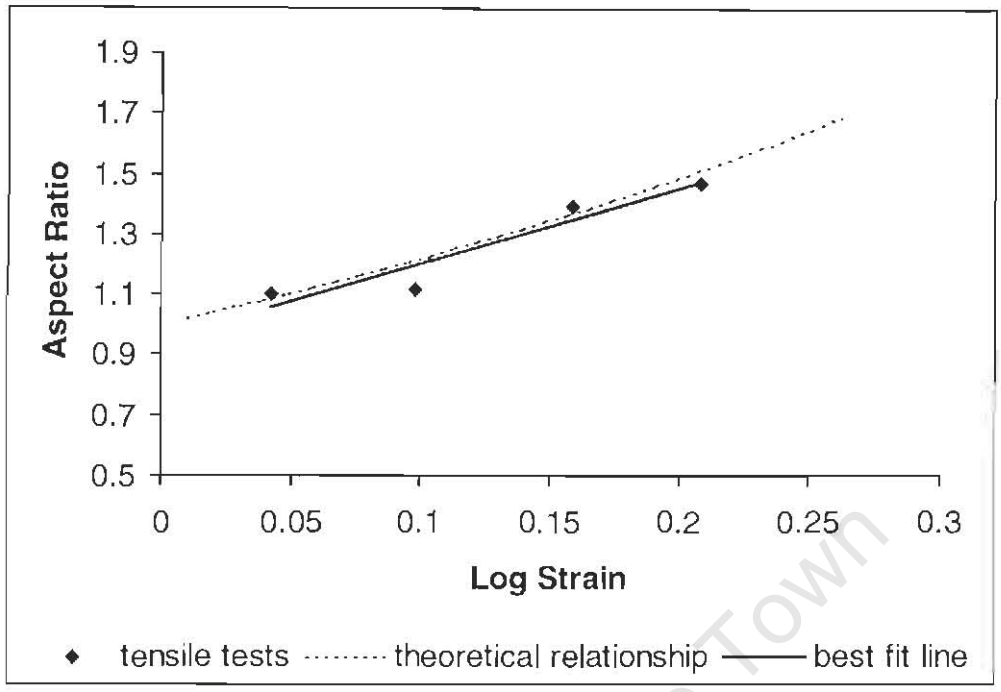

Figure 4.5 Graph of aspect ratio (α_r) vs. log strain for tensile tests and theoretical prediction

Each of the data points shown on the graph are the average of six micrographs. Each micrograph gives the average aspect ratio of between 40 and 60 grains. Therefore each data point is based on the measurement of approximately 300 grains. From all these measurements, the standard deviation of the aspect ratio measurements was calculated to be 0.12, this corresponds to a standard deviation in the strain of 0.04 (ie. the strain deviates by 0.04. from the mean.)

As can be seen, satisfactory correlation was obtained between the tensile test and the theoretical relationship for the strain - aspect ratio relationship. This equation will be used in the rest of the analysis as the method of relating the grain aspect ratio to strain.

Analysis of the tensile tests showed that necking started a strain of 0.23. By measuring the aspect ratio of the area adjacent to failure in a specimen that was strained until failure, the failure was found to occur at a localised log strain of 0.70. A value for the rupture strain of 0.7 could therefore be tested in the numerical model.

4.3 Blast-Loaded Plates

The method discussed in the foregoing sections was used as the basis from which to study the radial strain distribution in plates that had been deformed by explosive loading. Knowledge of the internal strain distribution would facilitate more accurate predictions of plate deformation and failure behaviour.

4.3.1 Radial Strain Profile

a) Strain vs. Radius graphs

Aspect ratio measurements obtained through micrograph readings were made at approximately 4mm intervals along the radius of the plate. These measurements were then converted to an equivalent log strain using equation 4.4. Five plates of each of the three thickness were analysed. Not all the results are shown here and the reader is referred to appendix IV for all of the results. The reader is referred to appendix I for data such as midpoint deflections and impulses relating to the blast loading experiments.

In all cases the distance along the radius is normalised to the original radius of the plate of 50mm. Measurements of the elongated radius will be discussed in the next section.

The strain along the radius for two 1.6mm plates with different impulses (I) was plotted as shown in figure 4.6. The overall strains are higher with larger impulses, and lower for smaller impulses. The graph shows that the strain is very high at the boundary (the area of the plastic hinge). The strain then evens out over the outer area of the plate and then increases towards the centre. The strains at the boundary and at the centre are greater than the necking strain (strain of 0.24) measured in the tensile tests. This corresponds to the necking and failure observed in the experiments. The strains directly adjacent to the failure surface were not measured in all cases. The maximum values of strain measured along the failed plates increase to a value approaching the 0.7 strain measured at the failure surface of the tensile test.

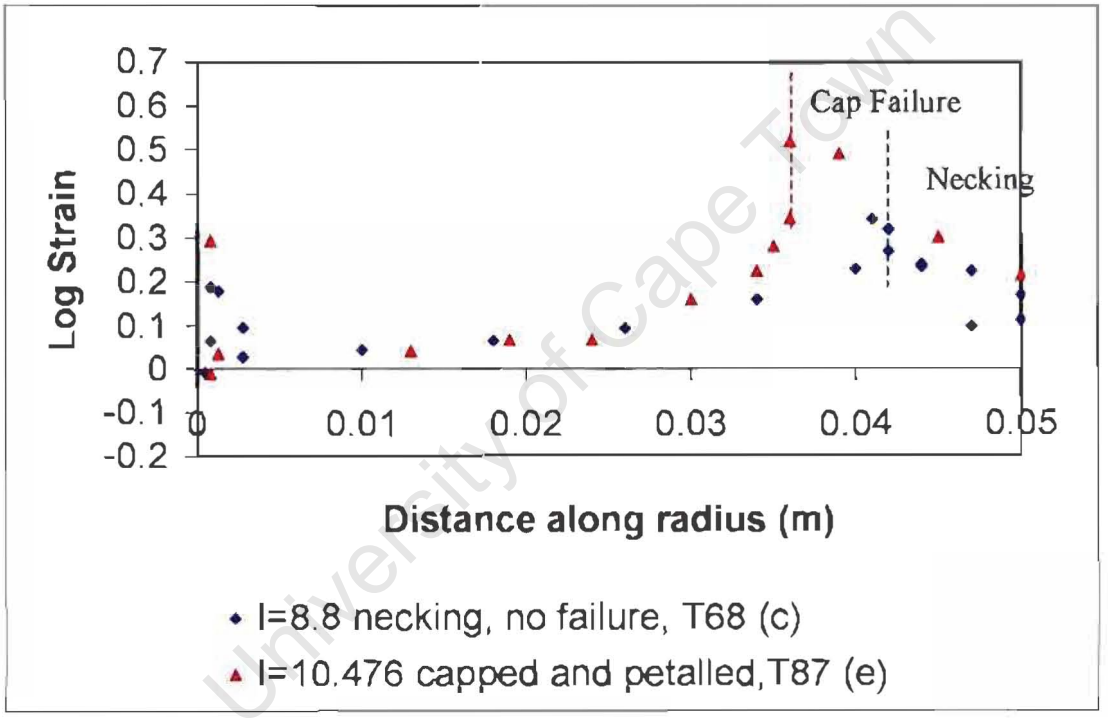

Figure 4.6 Graph showing strain measurements along the radius for two1.6mm plates

Similarly, the strain distribution along the radius of two 2.6mm plates is shown in figure 4.7. The strain distribution profile for the 2.6mm plates exhibits similar characteristics to that of the 1.6mm plates. Again the strain is high at the boundary. The plate loaded with a 14.34Ns

impulse appeared to have a constant strain towards the centre of the plate. This corresponds to the experimental observation where no necking was observed. For the plate loaded with a 17.983Ns impulse, the strain increases towards the centre of the plate to where the failure strain is reached at the cap radius At this point tensile failure occurred.

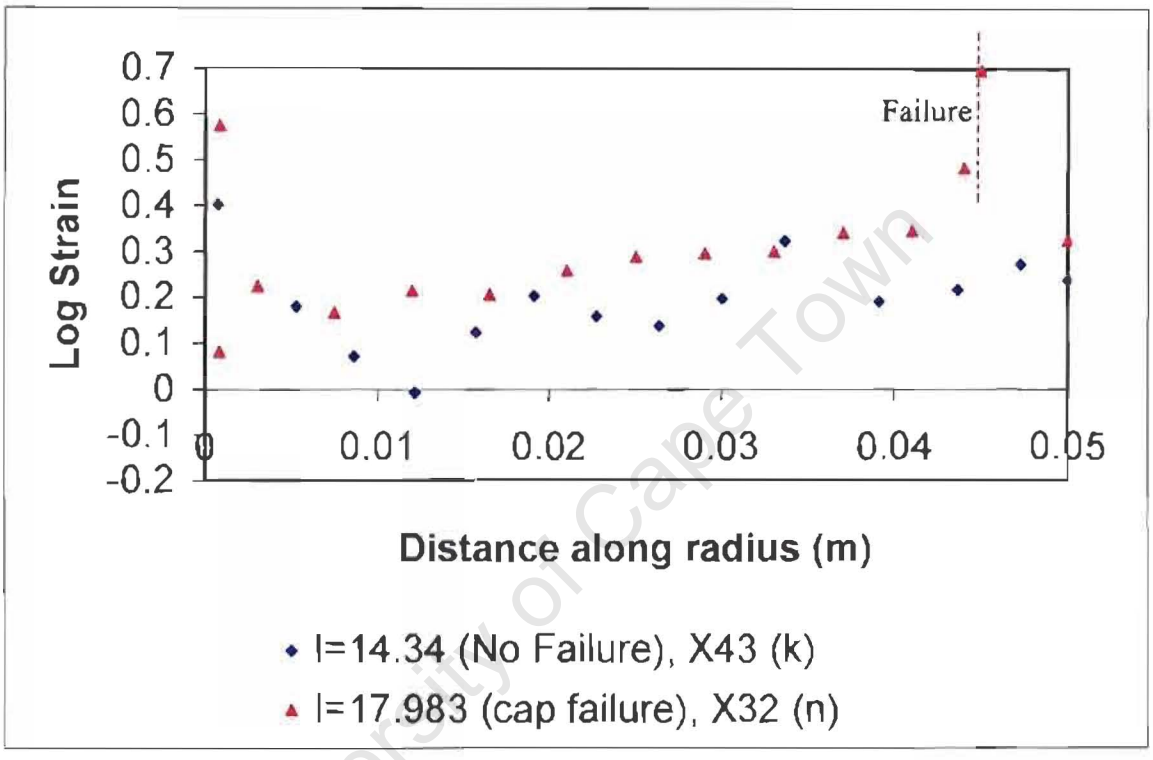

Figure 4.7 Graph showing strain measurements along the radius for two2.6mm plates

The 3.6mm plates appeared to have a significantly different strain profile as shown in figure 4.8. The strain is high at the boundary and the centre of the plate, but in the outer area of the plate there seems to be very little strain. It is therefore evident that bending at the plastic hinges at the plate boundary and centre contribute significantly to the overall strain.

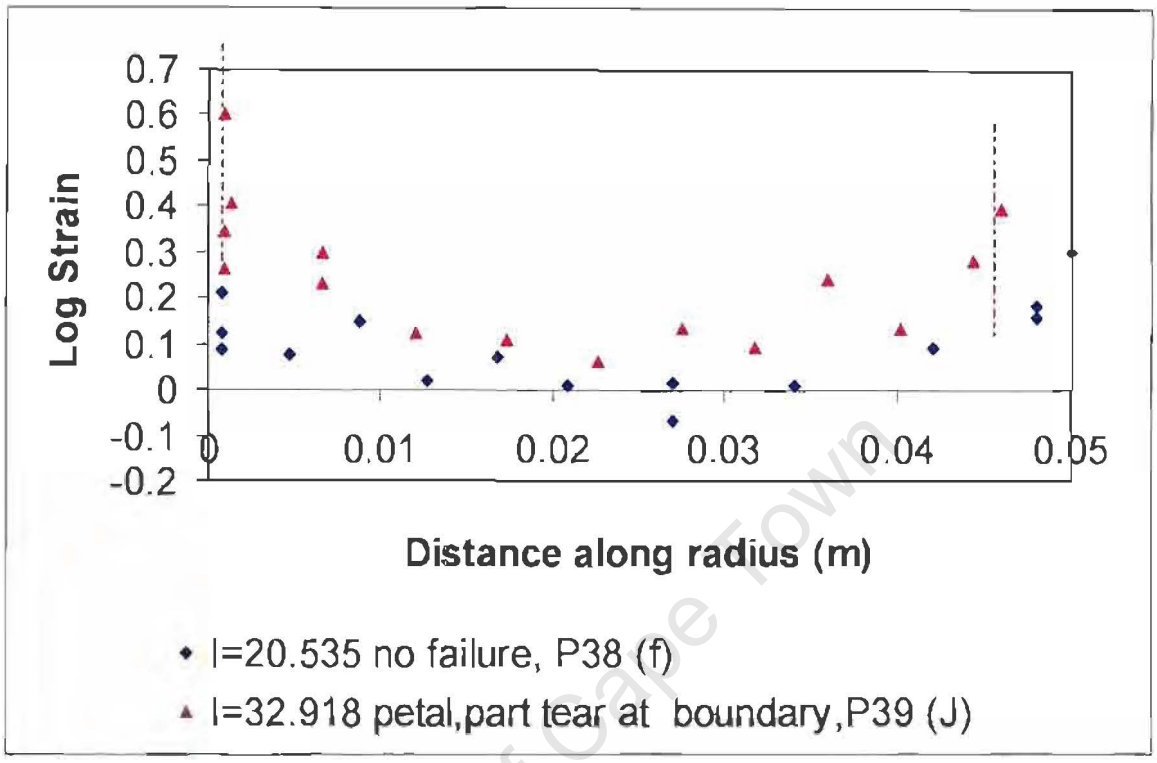

Figure 4.8 Graph showing strain measurements along the radius for two3.6mm plates

b) Elongation distribution over radius

In order to establish which areas of the plate underwent the most strain during the loading, it was necessary to divide the analysis of the elongation along the radius of the plate into 10mm sections. The contribution of each section to the overall elongation (Δl) could then be seen and the areas of highest elongation could be determined. The effect of plate thickness and impulse magnitude on the elongation distribution was determined.

In order to determine the elongation over sections of the radius, a polynomial was fitted to the strain profiles described in the previous section (as shown in figure 4.9).

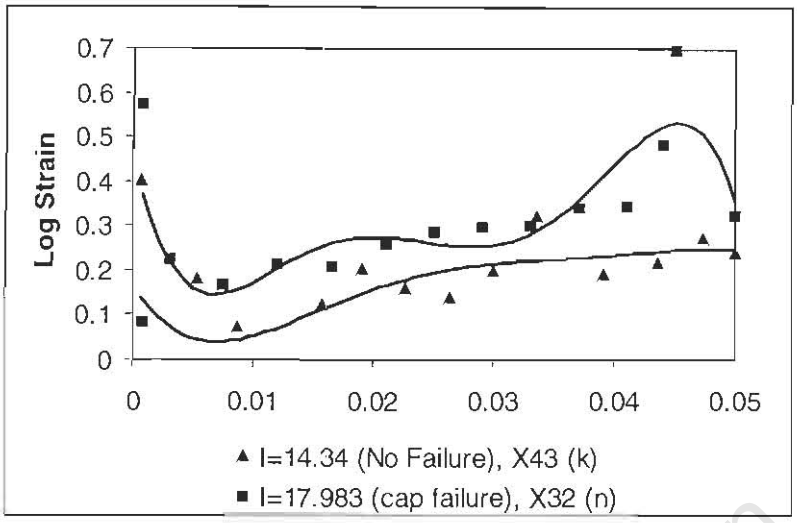

Figure 4.9 Best-fit fifth order polynomials fitted to 2.6mm plate strain data

The equation of the polynomial $\varepsilon(r)$ was integrated over sections of the radius in order to obtain the contribution of 10mm radius sections of plate to the overall elongation as described by equation (4.5).

$$Elongation_{\Delta r_1} = \int_{r}^{r+\Delta r_1} \varepsilon(r)dr \tag{4.6}$$

Where Δr_1 is the section of the radius being considered.

Figures 4.10-4.12 show the elongation contributions along the plate radius. At low impulses, the 1.6mm and the 2.6mm plates' elongation increases towards the boundary and centre of the plate. For higher impulses on the 1.6mm and the 2.6mm plates, a large amount of the elongation occurs nearer the centre of the plate. In the 3.6mm thick plate, the elongation occurs predominantly near the centre of the plate and at the boundary.

From this analysis it is evident that at high impulses and at large thicknesses, the elongation varies significantly across the plate and justifies the consideration given to it in recent attempts to understand failure of blast loaded plates.

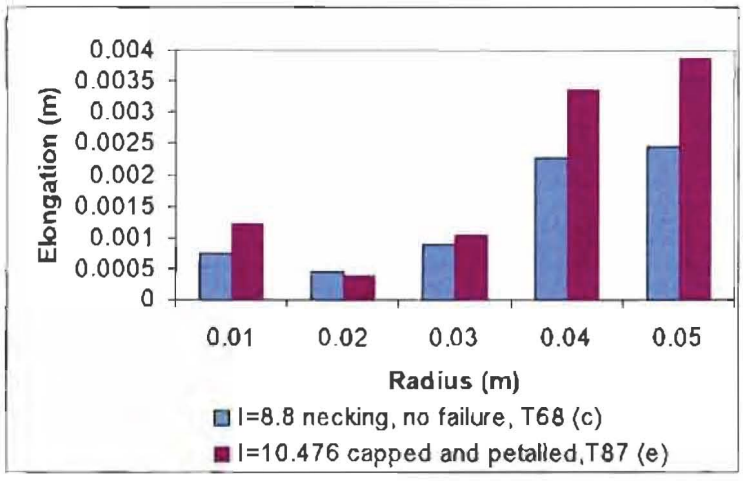

Figure 4.10 Elongation across the plate radius –1.6mm thick plate

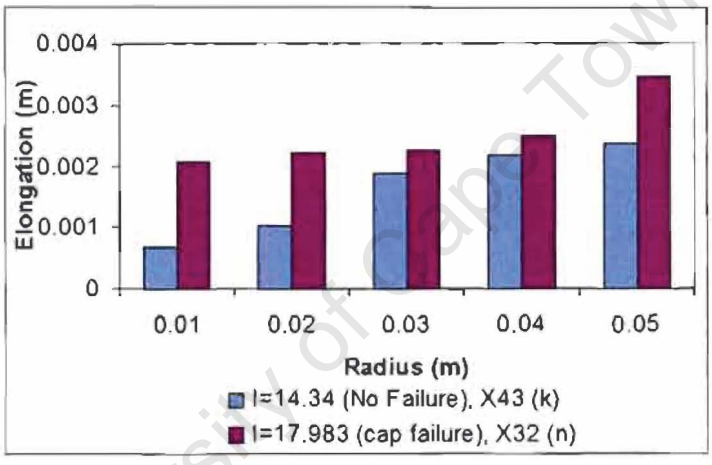

Figure 4.11 Elongation across the plate radius –2.6mm thick plate

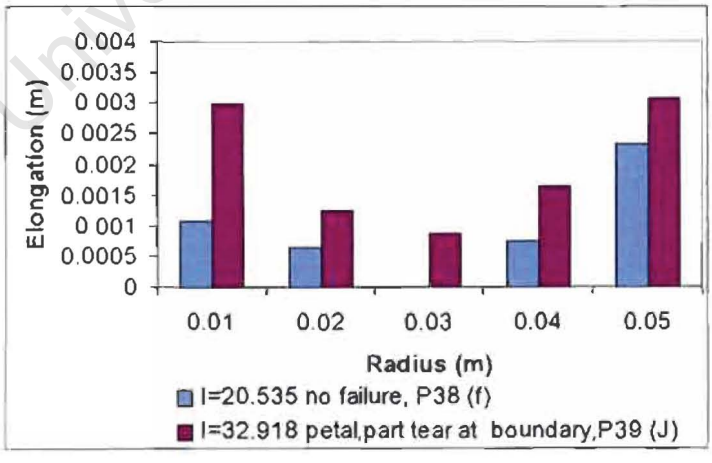

Figure 4.12 Elongation across the plate radius –3.6mm thick plate

4.3.2 Estimate of Total Elongation and Plastic Work

This section of the study uses the strain profiles to estimate the total elongation and the deformation energy of the plates. It is intended as qualitative exercise and further analysis would be required to validate the results.

a) Total Elongation

Fifth order polynomials were fitted to the strain data obtained from the metallographic study. This was done by calculating the least-squares best-fit polynomial through the data points using the following equation:

$$\varepsilon(r) = b + c_1 x + c_2 x^2 + c_3 x^3 + c_4 x^4 + c_5 x^5 \tag{4.7}$$

where b and c_1, c_2, c_3, c_4, c_5 are constants.

The area under this curve was calculated in order to determine the total elongation over the specimen, since the elongation Δl is defined as:

$$\Delta l = \int_0^R r\varepsilon(r)dr \tag{4.8}$$

Here, $\varepsilon(r)$ is the strain distribution given by the polynomial obtained from the metallographic data. And is thus used to calculate the overall elongation.

The results for the total elongation of the plates are shown in figure 4.13. It can be seen that the amount of elongation increases to a maximum at the point of failure as the impulse increase. In the plates that have failed the total amount of elongation seems to decrease as the impulse gets greater. This is thought to be due to the fact that the plate stops deforming at the centre after the cap has blown out. As the impulse became larger, the failure occurred earlier and thus at very high impulses, the elongation was less than in plates which have lower impulses. This reduction of deformation at high impulses was

also observed for uniformly loaded plates by Teeling-Smith and Nurick [10]. The overall elongation was not measured at the time of the blast loading experiments and therefore there is no experimental data for comparison.

In order to compare the elongations calculated using the grain aspect ratio, to theoretical elongations found in the literature, the average strain prediction of Symonds and Wierzbicki [25] is used. Symonds and Wierzbicki predict an average strain throughout a deformed plate using the mode approximation technique. Their method allows for localised central loading. They predict the radial average strain for 0.033mm loads be:

$$\varepsilon_r^{avg} = \frac{I^2}{R^4 t^2 \rho \sigma_0}, 0.07986 \qquad (4.9)$$

Thus the elongation is:

$$\Delta l = \frac{I^2}{R^4 t^2 \rho \sigma_0}, 0.07986.R$$

It can be seen in figures 4.13 (a-c) that the calculated strain is in general higher than the predicted strain. At low impulses this difference is the least. The membrane mode approximation does not take into account the high strains at the areas of necking. Therefore when the impulse is large and necking accounts for a significant part of the elongation, the prediction tends to under predict the elongation. The details of the calculation are given in Appendix II.

b) Deformation Energy

As plastic work is a function of the stress and strain only, it was possible to calculate the approximate deformation energy. Rigid plasticity was assumed and the strain over the plate was calculated from the best-fit polynomials.

Duffey [3] and Teeling-Smith and Nurick [10] used the mid-point deflection and an assumed mode shape function to calculate the deformation energy of uniformly loaded plates. This work is extended here to make use of the strain distribution to calculate the deformation energy. From the original continuum definition of plastic strain energy:

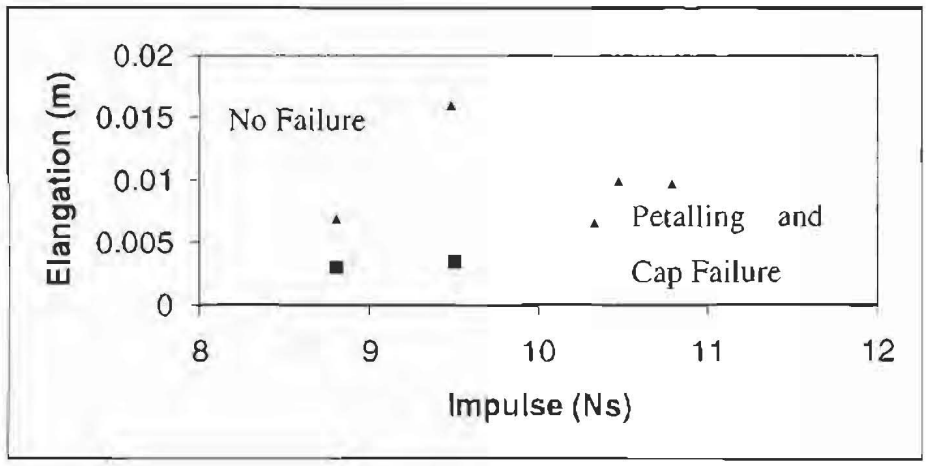

Figure 4.13a) Elongation vs. Impulse for 1.6mm plate,▲ Experimental,■ Prediction.

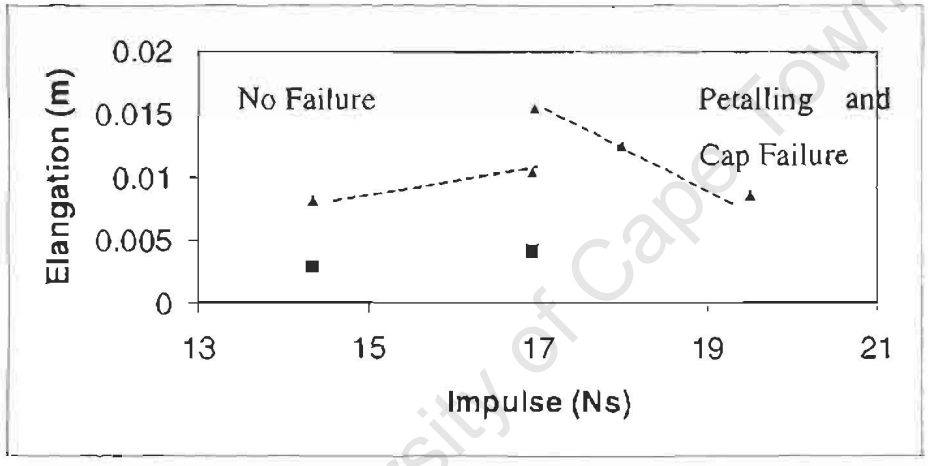

Figure 4.13b) Elongation vs. Impulse for 2.6mm plate,▲ Experimental,■ Prediction.

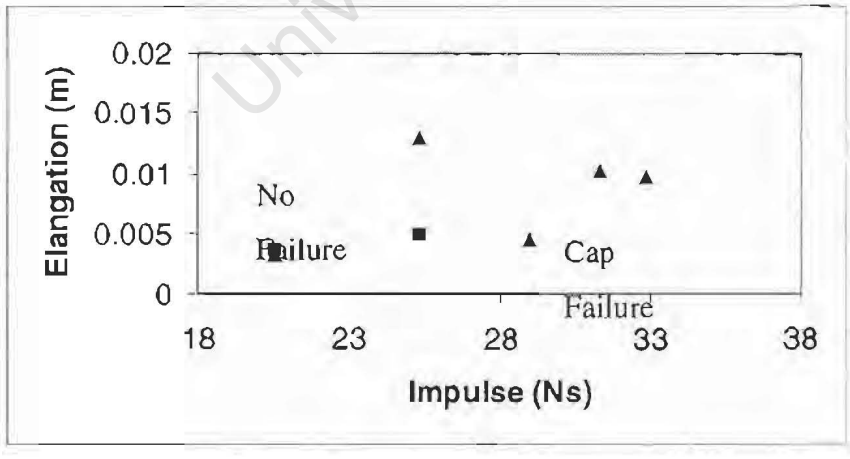

Figure 4.13c) Elongation vs. Impulse for 3.6mm plate,▲ Experimental,■ Prediction.

$$E_p = \int_v (\int \sigma^{ij} \varepsilon \; d\varepsilon^{ij}) dv \tag{4.9}$$

They calculated the deformation energy to be:

$$E_p = 2\pi t \int_0^R \sigma_{rr} \varepsilon_{rr_0} dr \tag{4.10}$$

$$\text{where } \varepsilon_{rr_0} = \frac{1}{2}\left(\frac{\partial w}{\partial r}\right)^2 \tag{4.11}$$

with $w = w(r)$ being the assumed mode shape.

The radial yield stress σ_{rr} is assumed to be:

$$\sigma_{rr} = \frac{\sigma_0^1}{(1 - \nu + \nu^2)^{\frac{1}{2}}} \tag{4.12}$$

with σ_0^1 being the rigid plastic von mises yield stress adjusted for strain rate sensitivity.

In the present analysis, the strain profile is calculated from the best-fit polynomials fitted to the metallurgical data. The strain along the radius is given by $\varepsilon_{rr_0} = \varepsilon(r)$. So the deformation energy equation becomes:

$$\boxed{E_p = 2\pi t \int_0^R \frac{\sigma_0^1}{(1 - \nu + \nu^2)^{\frac{1}{2}}} \varepsilon(r) dr} \tag{4.13}$$

Assuming a static yield stress of 450MPa and a strain rate[1] of 2000s^{-1}, σ_0^1 for was calculated to be 870MPa.

The results of the calculations for the three plate thicknesses are shown in figure 4.14. It can be seen that the deformation energy increases with increasing impulse until cap failure occurs. The deformation energy then decreases at higher impulses.

[1] Assuming average strain across the plate 0.12, deformed in 80μs.

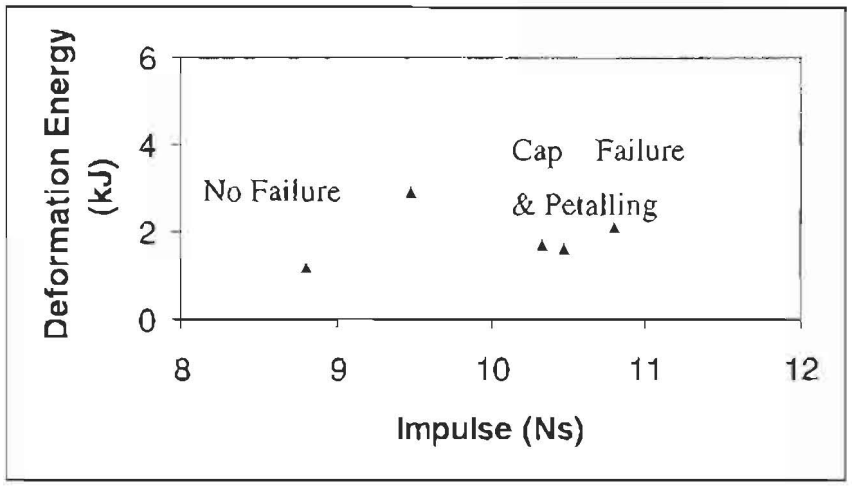

Figure 4.14a) Deformation Energy vs. Impulse for 1.6mm plate

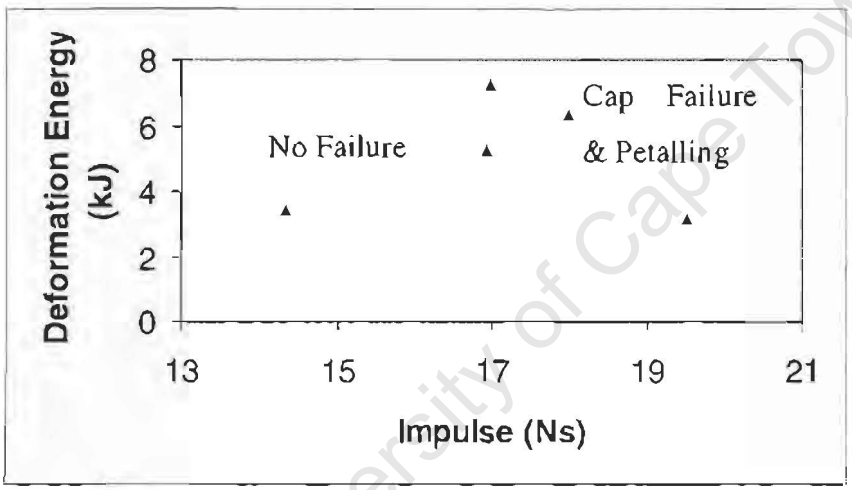

Figure 4.14b) Deformation Energy vs. Impulse for 2.6mm plate

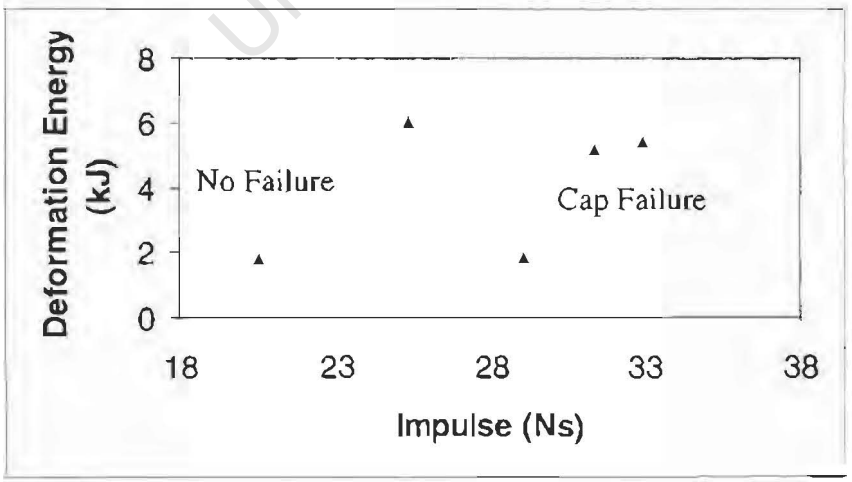

Figure 4.14c) Deformation Energy vs. Impulse for 3.6mm plate

4.3.3 Through Thickness Strain Variation

As the plates are loaded, they undergo both bending and tension in the radial direction. The bending strains are greatest on the outside of the bend and are compressive on the inside of the bend. When considered in conjunction with the tensile strain, the bending strains cause an increase in the strain on the outside of the bend. The strains on the inside of the bend were reduced. Figure 4.15 shows the strain distribution across a 1.6mm plate, where the strains have been measured near the top and bottom surfaces of the plate.

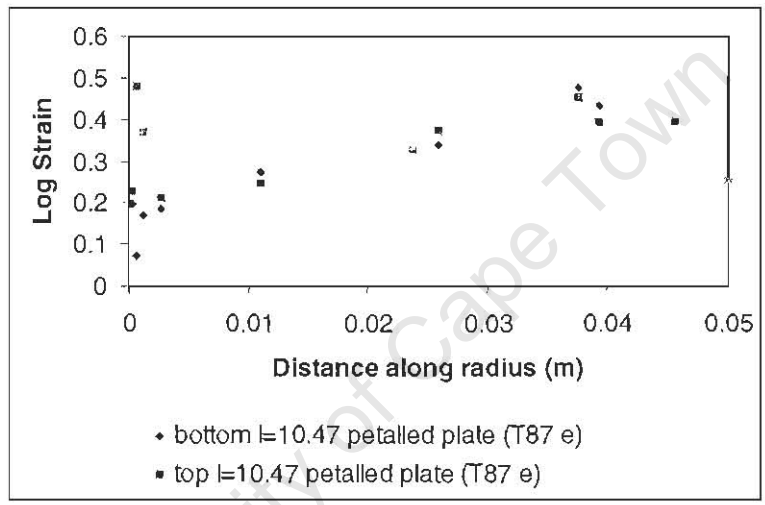

Figure 4.15 Strain distribution across 1.6mm plate showing through thickness differences

In figure 4.15, the top surface is the surface to which the loading was applied. The top surface is on the outside of the bend at the boundary and consequently is shown to have the highest strain at the boundary. Near the centre of the plate, the plate undergoes a change in curvature at the inflection diameter. The bottom surface then becomes the outer surface of the bend and the highest strains are thus found on this surface.

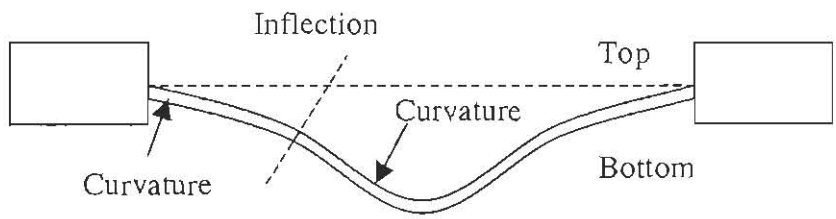

Figure 4.16 Diagram showing curvature of plate.

4.4 Failure Analysis

The failure surfaces and the grain structure adjacent to the failure surface were studied under a scanning electron microscope in order to determine the type of failure that occurred. This was done for both the tensile test and the blast loaded plates.

4.4.1 Tensile Tests

a) Micrographs

The micrographs shown in figure 4.16 shows the failure surface of tensile test specimen. It can be seen that the surface is dimpled which is typical of ductile failure by microvoid coalescence. The dimples are not smeared in any direction which shows that the voids grew under pure tension. Figure 4.16 a & b show the same dimpled fracture surface with figure b being at a higher magnification.

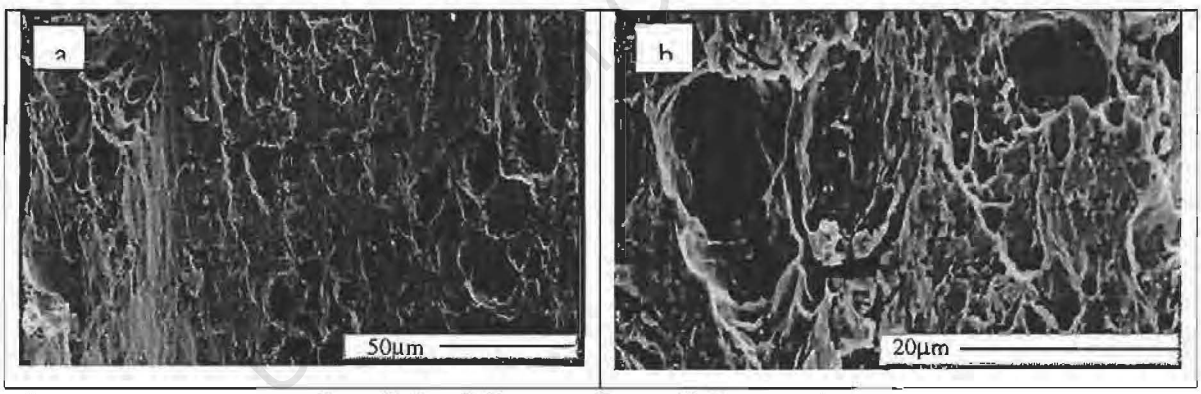

Figure 4.16 Micrographs of the failure surface of the tensile test specimen. a) 551×, b)2200× magnification.

b) Failure Strain

The grain aspect ratio was measured adjacent to the failure surface. The aspect ratio was found to be 4.41 which corresponds to a strain of 0.70. This value will be compared with numerical models using this strain value as a failure criterion will be investigated.

4.4.2 Blast Loaded Plates

The micrographs of the failure surfaces of the blast loaded plates are shown in figure 4.17. The following discussion refers to these micrographs.

a-c. Micrographs a-c are of a crack that started to grow on the outside of the bend at the boundary of the plate. Micrograph a is at very low magnification and shows the bend and the grain structure around it. Micrograph b is at the start of the crack near the outer surface of the bend. The grains are highly deformed and are orientated parallel to the crack. This is due to the combination of shear, bending and tension experienced at this point in the material. Micrograph c is at the crack tip. The process of microvoid coalescence can be seen and voids can be seen opening up ahead of the crack. There are very few voids other than those in the crack path and it thus appears that void growth occurs just before the failure. The grains seem to be at about 45 degrees to the crack, indicative of the combined loading being experienced.

d. Micrograph d is at the tip of a crack forming at the cap of the plate. It can be seen that the grains are highly elongated and that the elongation is perpendicular to the crack. This shows that necking has occurred and that the grains are experiencing a pure tension type of loading.

e-g. Micrographs e-g are of the grain structure adjacent to the failure surface at the cap of a plate. The highly elongated grains are again evident. Micrograph e and f are taken at relatively low magnification. Voids can be seen in the grains and at their boundaries. Micrograph g shows, at higher magnification, the void growth in a grain and at its boundary.

h. Micrograph h is of the failure surface at the cap failure. It shows the presence of dimples on the surface which is indicative of ductile failure. The dimples are far smaller than those found on the tensile specimen.

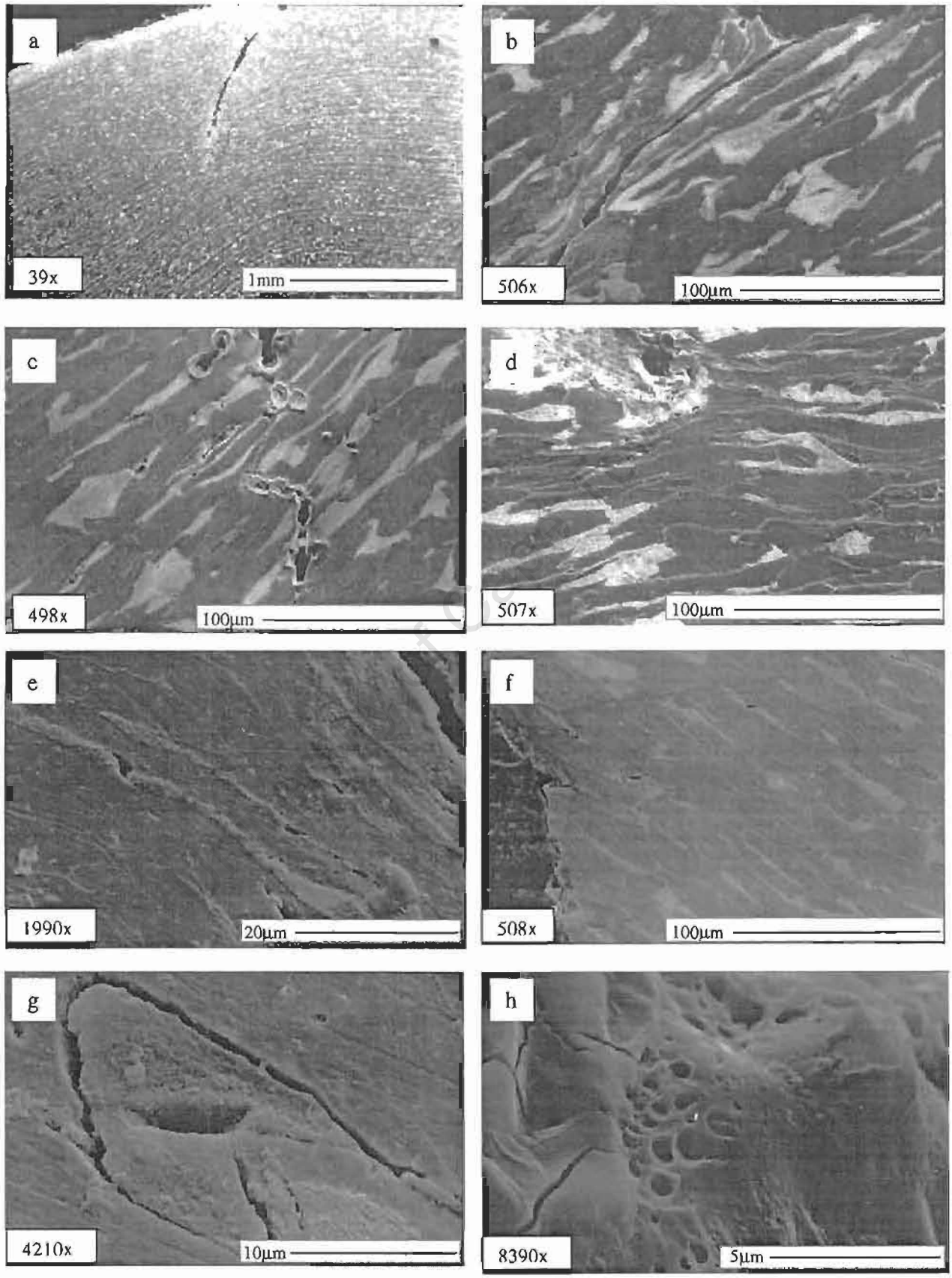

Figure 4.17 Micrographs of the failure surfaces of the blast loaded plates.

CHAPTER 5

METHOD OF NUMERICAL ANALYSIS

5.1 Introduction to ABAQUS/Explicit

The numerical modeling undertaken in this study used the ABAQUS/Explicit finite element package. This package allows the modeling of dynamic processes and is ideally suited to modeling of the dynamic response to rapidly applied loads.

The ABAQUS/Explicit program uses an explicit dynamic finite element solution procedure. This procedure is based upon the implementation of an explicit integration rule together with the use of diagonal (lumped) mass matrices [53]. The equations of motion of the body are calculated using the explicit central difference integration rule:

$$\dot{u}^{(i+\frac{1}{2})} = \dot{u}^{(i-\frac{1}{2})} + \frac{\Delta t^{(i+1)} + \Delta t^{(i)}}{2} \ddot{u}^{(i)} \tag{5.1}$$

$$u^{(i+1)} = u^{(i)} + \Delta t^{(i+1)} \dot{u}^{(1+\frac{1}{2})} \tag{5.2}$$

Where u = displacement

$\dot{u}$ = velocity

$\ddot{u}$ = acceleration

Δt = the stable time increment of the increment

The acceleration $\ddot{u}$ is calculated using the diagonal element mass matrices which results in high computational efficiency. The calculation of $\ddot{u}$ is as follows:

$$\ddot{u} = M^{-1} \cdot (F^{(i)} - I^{(i)}) \tag{5.3}$$

where M is the lumped mass matrix, F is the applied load vector and I is the internal force vector.

The stable time increment Δt is calculate at each time step using:

$$\Delta t \leq \min\left(L^{el} \sqrt{\frac{\rho}{\lambda + 2\mu}} \right) \tag{5.4}$$

where L^{el} a characteristic element length and λ and μ are material constants.

5.2 Modelling the Tensile Tests

A numerical model was made of the tensile tests carried out in section 4. A quarter of the dog-bone tensile test specimen was modeled as shown in figure 5.1

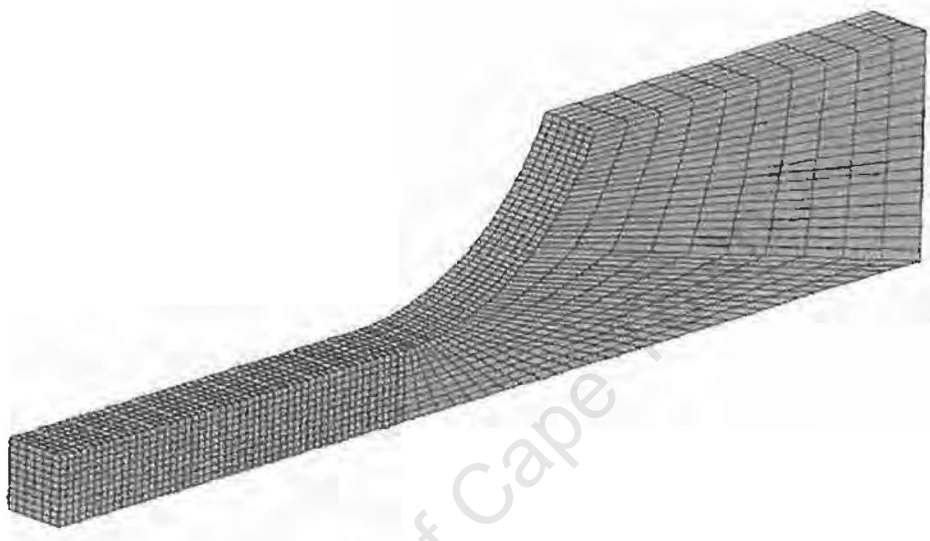

Figure 5.1 Model of tensile test specimen.

5.2.1 Elements

Three dimensional continuum elements were used in this model. Three dimensional elements were used as a fine mesh was required to model strain localization after necking. The strains through the thickness of the tensile test specimen needed to be calculated and therefore a mesh which contained numerous elements through the thickness was used.

The element used was ABAQUS/Explicit element type C3D8R. This is an 8-node linear brick element with reduced integration and hourglass control. The default settings for the hour glass control were used. A diagram of the element and its node numbering is given in figure 5.2 [54].

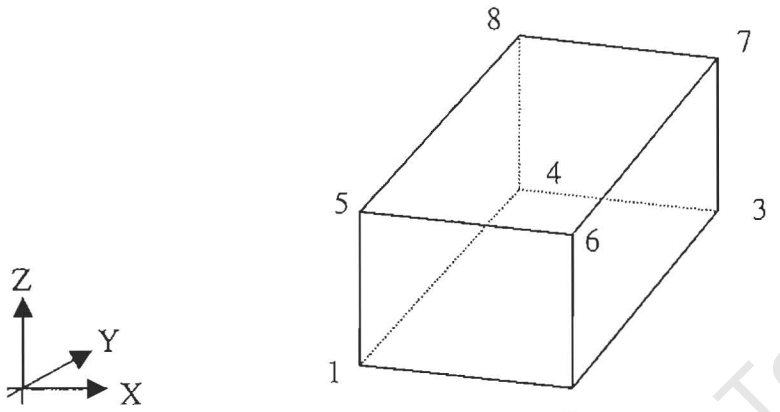

Figure 5.2 Node ordering of 3-D brick element.

5.2.2 Materials

The material description for the model is an elastic plastic material with isotropic strain hardening. The elastic properties were:

Young's Modulus E = 210GPa

Poisson's ratio v = 0.3

Density ρ = 7800kg/m^3

The plastic properties are taken from discretized data from tensile tests. The 'true' (Cauchy) stress and log plastic strain were required by ABAQUS. The true stress vs log strain curve is shown in figure 5.3. Equations 5.5 and 5.6 were used to convert the measured stress and strain to the true stress and log strain [54]:

$$\sigma_{true} = \sigma_{nom}(1 + \varepsilon_{nom}) \tag{5.5}$$

$$\varepsilon_{\ln}^{pl} = \ln(1 + \varepsilon_{nom}) - \frac{\sigma_{true}}{E} \tag{5.6}$$

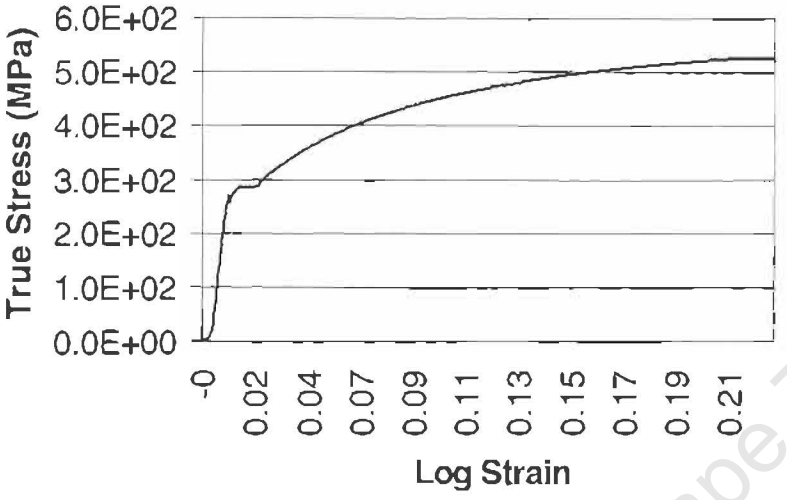

Figure 5.3 Graph showing true stress vs. log strain material properties

Strain rate sensitivity was ignored as the tensile tests were performed at a very slow strain rate and were thus assumed to be quasi static. The cross-head speed of the tensile testing machine was 2mm/minute for all of the tensile tests. This gives a strain rate for the tensile test of approximately $6.5 \times 10^{-4}\ s^{-1}$.

5.2.3 Boundary Conditions

X - symmetric and Y - symmetric boundary conditions are applied to the surfaces where symmetry is enforced. The boundary conditions are shown on the meshed tensile test specimen in figure 5.4.

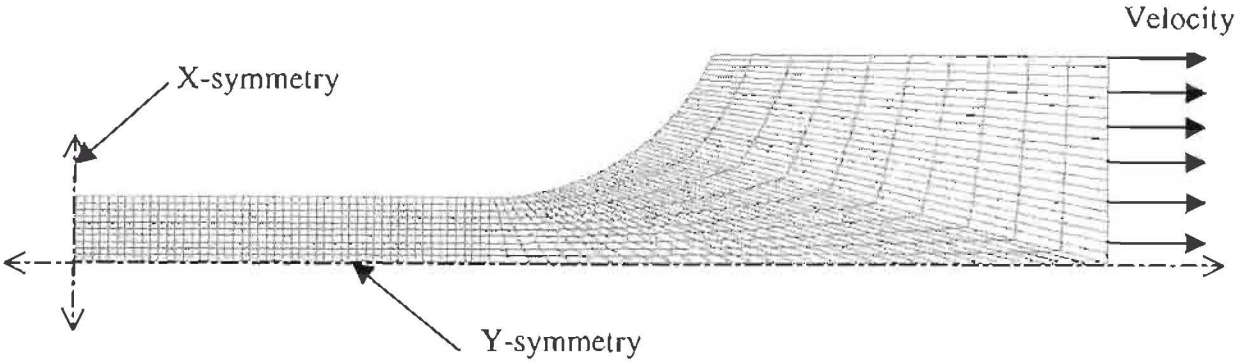

Figure 5.4 Symmetry boundary conditions of the tensile test model

5.2.4 Loading

The tensile test specimen is loaded by displacing the right hand edge of the specimen with a constant velocity for a set time (See figure 5.4). A displacement velocity of 0.3 m/s (1.8×10^4 mm/minute) was used to displace the boundary. The loading velocity of the model was required to be far greater than that of the actual tests as the stable time increment of the explicit solution scheme was small and therefore the solution was computationally slow. The loading velocity was therefore increased to improve the computational efficiency. As strain rate sensitivity was excluded, it was found that increasing the velocity of displacement had little effect on the response of the model. The time period of velocity loading was adjusted to give the displacement as recorded from the tensile tests.

5.3 Modelling the Blast Loaded Plates

The model of the blast loaded plates were required to show: a) the global deformations, b) the strain distribution through the thickness and along the radius, c) strain localization and necking and d) the failure of the plate. A cross-section of the plate was modeled axisymmetrically as all of these effects could be seen by modeling the plate along its radius. The area of the plate modeled is shown in figure 5.5. The size of the area modeled as the 'built-in' boundary was reduced from reality in order to decrease the number of elements. This was shown to have no influence on the response as the straining did not extend as far as the edge of the new boundary. All three plate thicknesses were modeled using the same number of elements and just changing the overall dimensions.

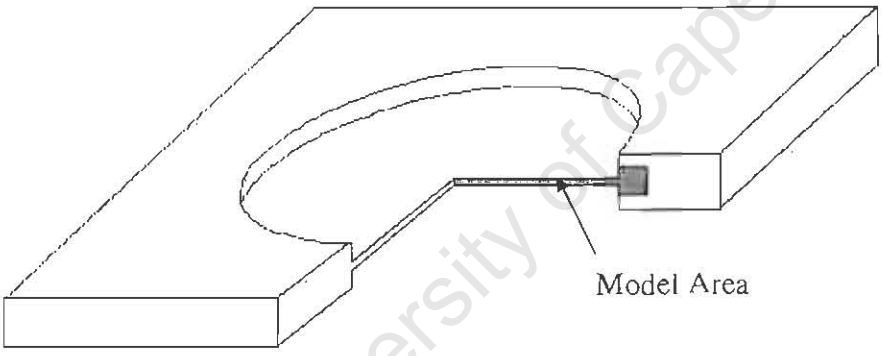

Figure 5.5 Diagram of the plate showing the area included in the axisymmetric model

Six models were investigated in total, two for each plate thickness. For each thickness one model had an impulse that was not sufficient to cause failure and the other had a large impulse that caused the plate to fail.

5.3.1 Elements

As described above, the model was defined axisymmetrical and thus axisymmetric elements were used. The element chosen was ABAQUS/Explicit element type CAX4R. This is a 4-node bilinear axisymmetric element with reduced integration and hourglass

control. Again the default settings for hourglass control were used. A diagram of the element and its node numbering is given in figure 5.6 [54].

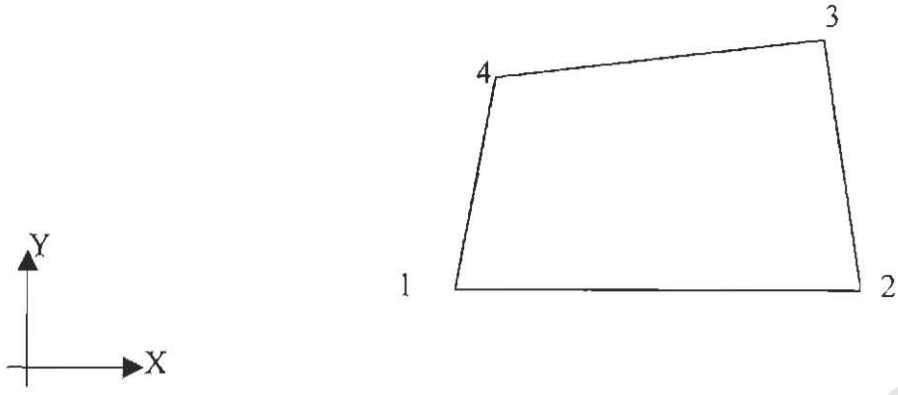

Figure 5.6 Element type CAX4R

5.3.2 Materials

A material model for an elastic plastic isotropically hardening material was used. The properties assumed are the same as for the tensile test and the reader is referred to section 5.2.2 for details of these properties.

During the response of blast loaded plates, strain rates of the order of 10^3 are encountered. Strain rate sensitivity effects are therefore significant and could not be ignored. The rate dependant material behaviour modeled by ABAQUS was used to describe the strain rate sensitivity. This material model is based on the Cowper-Symonds power law relationship:

$$\frac{\sigma_y}{\sigma_0} = 1 + \left(\frac{\dot{\varepsilon}}{D}\right)^{\frac{1}{q}} \tag{5.7}$$

In equation 5.7, $\dot{\varepsilon}$ is the strain rate and D and q are material parameters. These parameters have values of $D = 40s^{-1}$ and q=5 for mild steel. [46]

A material rupture model is introduced to model the failure of the plate at both the cap and the boundary. ABAQUS 5.8 has introduced a new failure model which is different to

that used by Gelman [34]. This model simply defines a rupture strain such that when the equivalent plastic strain in an element reaches that value it is said to have failed and can no longer carry any stress. A damage parameter ω is defined as :

$$\omega = \sum \frac{\Delta \bar{\varepsilon}^{pl}}{\bar{\varepsilon}^{pl}_{f}} \tag{5.8}$$

where $\Delta \bar{\varepsilon}^{pl}$ is the equivalent plastic for one time increment and $\bar{\varepsilon}^{pl}_{f}$ is the rupture strain.

$$\bar{\varepsilon}^{pl} = \int_{0}^{t} \sqrt{\frac{2}{3} \dot{\varepsilon}^{pl} : \dot{\varepsilon}^{pl}}\, dt \tag{5.9}$$

An element has failed when $\omega = 1$ in that element [53]. For first-order reduced-integration solid elements, failure at only one integration point is required for failure of that element.

This failure model is the recommended method of defining failure in high-strain-rate problems in ABAQUS, while the Gurson model is recommended for quasi static problems [56].

Previous attempts to model the failure of plates using a simple rupture strain failure criterion have proved unsuccessful. This new failure model is incorporated into this study in order to evaluate if it is any more successful at modeling plate failure as well as to provide qualitative information of post-failure strain behaviour.

5.3.3 Boundary

The center line of the plate is at the center of the axisymmetric model and is thus given y-symmetric loading condition. The upper and lower surfaces of the built-in boundary are fixed in space using an encastre boundary condition. The mesh and boundary conditions are shown in figure 5.7.

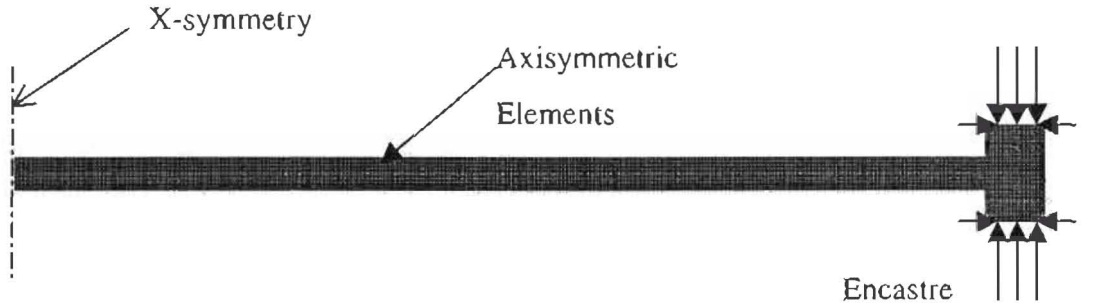

Figure 5.7 Boundary conditions of the plate model

5.3.4 Loading

Understanding the exact loading in blast loading problems is an ongoing field of research as described in section 2.2.2. In the setting up of this model three of the methods suggested in section 2.2.2 were attempted before one was decided upon and used. The three methods tried were a) a central pressure load, b) modelling the explosive using the equation of state and c) a constant central pressure with a exponentially decaying pressure over the rest of the plate.

a) Central Pressure Load

A central pressure load was applied for the duration of the burn time of the explosive. The magnitude of the impulse was calculated from the measured impulse using the following simple equation.

$$P = \frac{I}{A\tau} \tag{5.10}$$

where P is the central pressure, I is the total impulse and τ is the burn time of the explosive.

This pressure was then applied to the model of the plate using the distributed load option in ABAQUS.

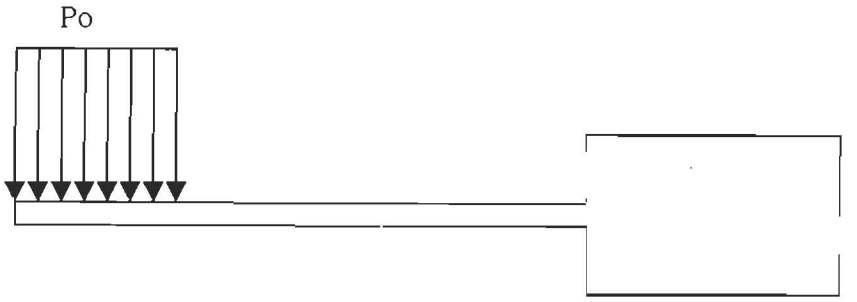

Figure 5.8 Constant pressure load on central area of plate

Using this method of loading was found to cause excessive necking at the central cap. This was thought to be due to the load being applied over an unrealistically confined area.

b) Explosive Modelling using the Equation of State

Grobbelaar [33] has modeled the explosive material and the response of plates and hemispherical bowls using the equation of state and has reported good preliminary results. This method was extended for use in this study.

The mass of explosive is modeled using solid elements. As the explosive elements deform, as defined by the equation of state, it comes into contact with the plate and applies a pressure load to it. The plate response under this contact pressure loading is modelled in the same manner as described above.

This method was found to give good results for coarse meshes. For fine meshes, as required in this study, problems were encountered with excessively distorted explosive elements and unrealistic local damage on the plate surface as explosive elements made contact.

c) Constant Central Pressure Load with Exponential Decay.

Loading the plate using constant central pressure load with exponential decay was found to give the most reliable and accurate loading conditions. The loading profile is shown in figure 5.9. This method was used by Bimha [32] and Grobbelaar [57].

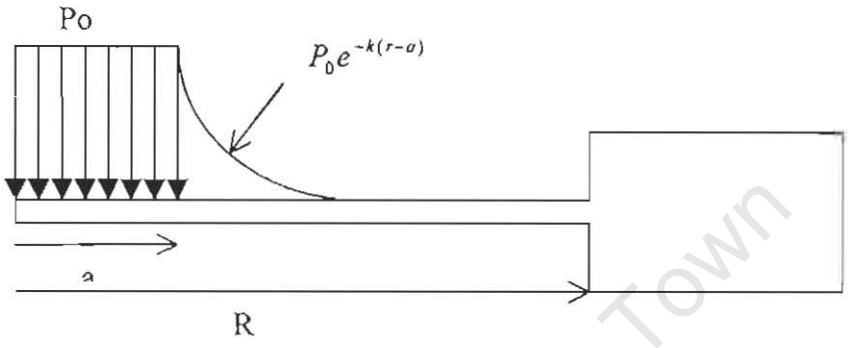

Figure 5.9 Pressure profile with constant central pressure and exponential decay.

A constant pressure Po was found such that integrating the pressure over the surface of the plate would give measured impulse. The impulse was found from the pressure using the following equation:

$$I = \tau 2\pi \left[\int_0^a P_0 dr + \int_a^R P_0 e^{-k(r-a)} dr \right] \tag{5.11}$$

This pressure loading profile was imposed by using a user defined load (vdload) in ABAQUS as described by Grobbelaar [57]. The exponential constant k was chosen by comparing the values recommended by Bimha with experimental observations and a value of 180 was chosen. The load is applied for a time step equal to the burn time of the explosive. The source code of the vdload is shown in appendix V.

This method gave accurate predictions of deformation profiles and mid-point displacements and was found to be the most reliable for this study. All plates shown in the following analysis were loaded using this method.

CHAPTER 6

RESULTS OF NUMERICAL ANALYSIS

6.1 Results of Tensile Test Model

The interrupted tensile tests were modelled as described in section 5.2. The five boundary displacements (displacement until test arrested) applied to these models were the same as those measured from the actual tests to allow for comparison. The principal strain values were recorded from the numerical model in order to compare with the strain measurements made experimentally in chapter 4.

Five models were run corresponding to the five tests shown on the stress strain curve in figure 4.4. The first four tests were strained to strains lower than the necking strain so that the strain across the specimen would remain uniform. Figure 6.1 shows the strain distribution through the tensile test specimen. The strain increases uniformly across the specimen over the first four tests. In the model of the fifth test, the specimen starts to neck once the material stops hardening. The instability caused by the difference in constraints at the boundaries was sufficient to induce necking. No additional geometric instability needed to be introduced in order to induce necking. The principal strain contours and deformed shapes of the models of these five tests are shown in figure 6.2

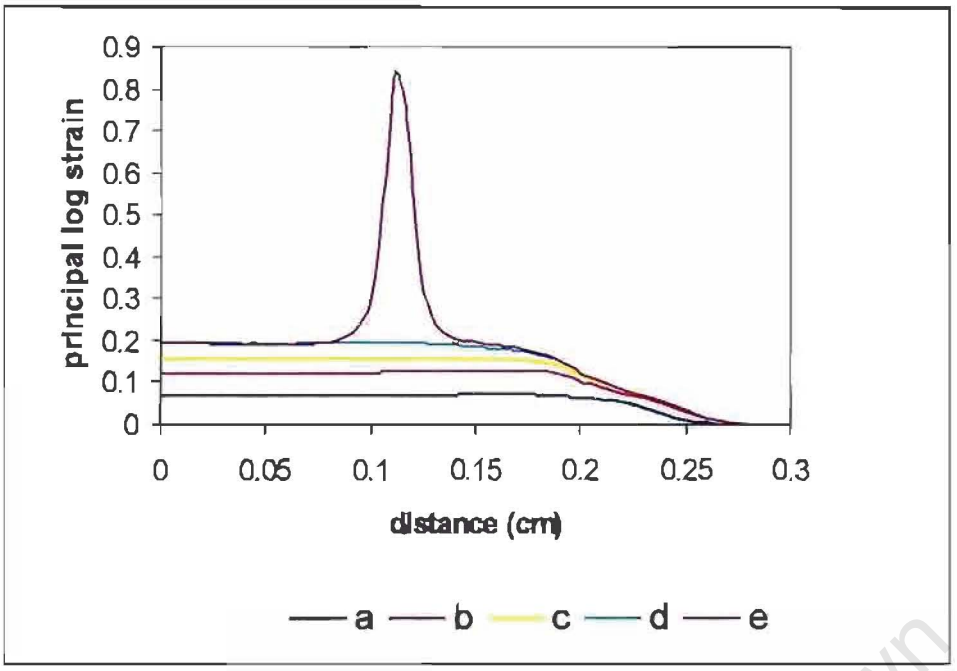

Figure 6.1 Strain across the tensile test specimen. Overall strain:
a) 0.046, b) 0.105, c) 0.174 d) 0.234, e) 0.272.

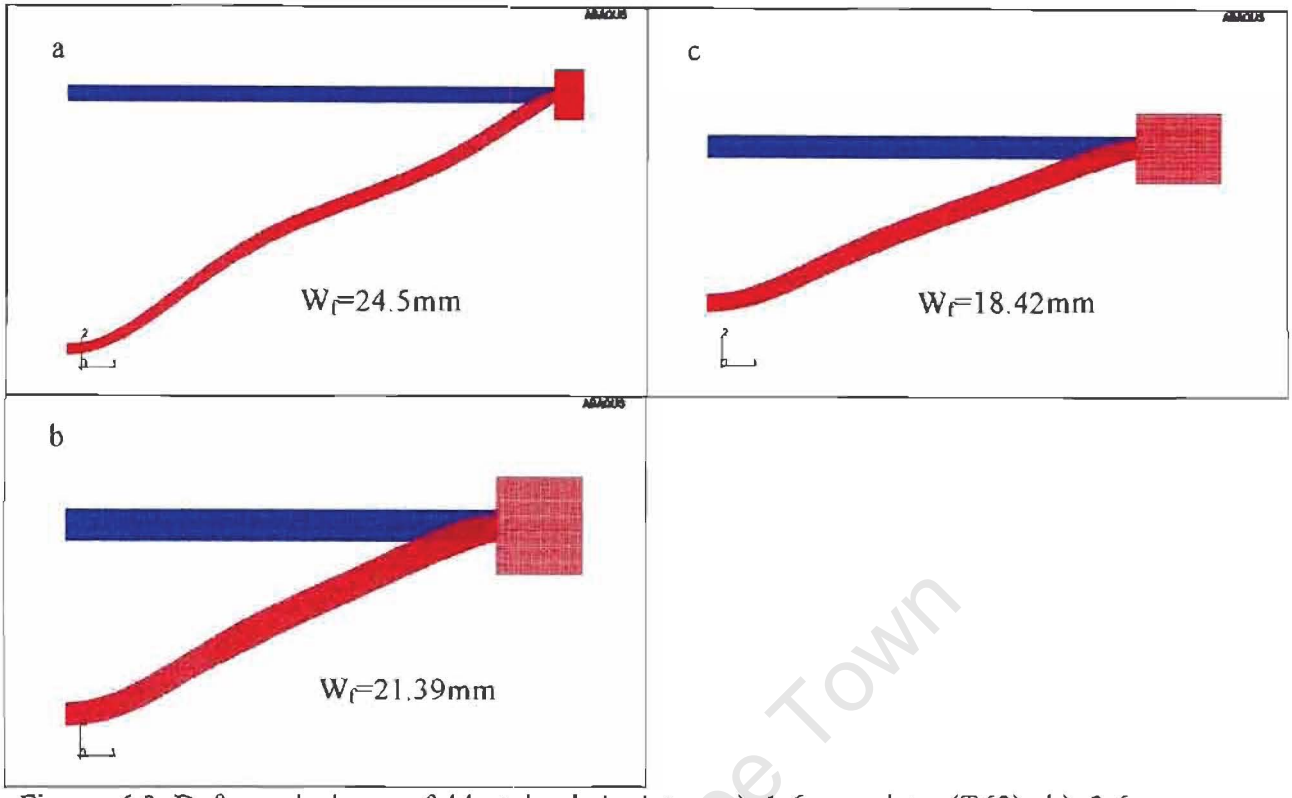

Figure 6.3 Deformed shape of blast loaded plates. a) 1.6mm plate (T68), b) 2.6mm plate(X40), c) 3.6mm plate (P38).

b) Deflection time history

The response time of the plates to the blast loading has been calculated to be of the order of 250μs [33]. The numerical model of the plate reached a state of equilibrium at about 200μs. In determining a theoretical prediction for the deformation of centrally loaded plates, Wierzbicki and Nurick [30] assumed that the plate deforms in two distinct phases. Phase I is the initial bulging at the centre of the plate during the initial blast-loading of the plate. Phase II is the response under inertia of the rest of the plate. The two phases are shown in figures 2.3a&b. The deflection and strain response over time for the modelled plates is shown in figure 6.4. These plots show how for approximately the first 30μs the deformation occurs primarily at the centre of the plate. This corresponds to the phase I response as described by Wierzbicki and Nurick. For the remainder of the response time , the plate deforms over the entire plate with plastic hinges developing at the centre and boundary of the plate. This corresponds with the phase II response.

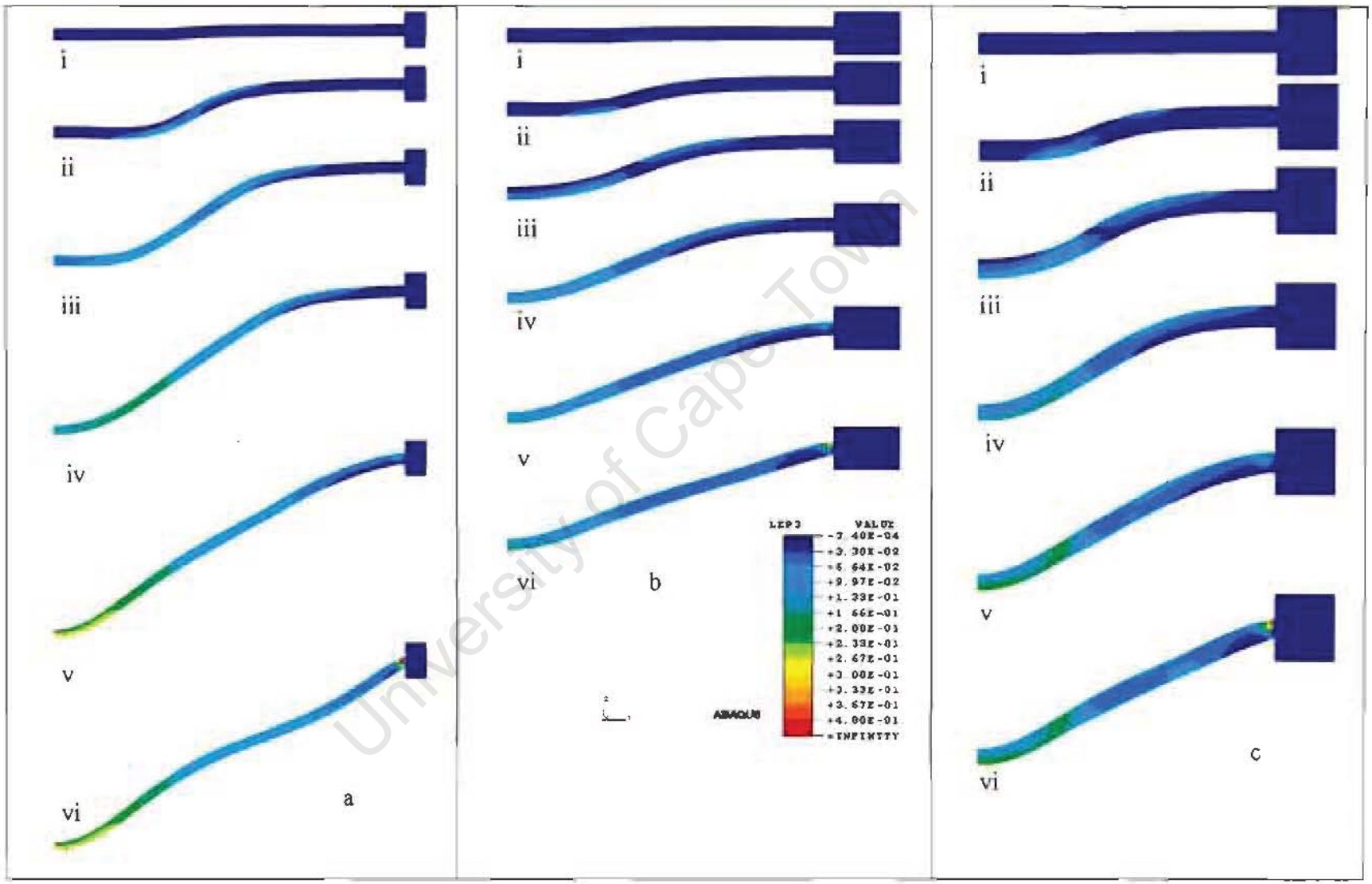

Figure 6.4 Deformed shape history of blast loaded plates. a) 1.6mm plate (T68), b) 2.6mm plate(X40), c) 3.6mm plate (P38) i) 2.4 μs, ii) 14.1 μs, iii) 25.8 μs, iv) 37.5 μs, v) 60.9 μs, vi) 236.4 μs.

c) Strain distribution

The strain distribution over the radius of the plate was recorded from the numerical model to allow comparisons with the strains measured experimentally and described in chapter 4. The strain used is the maximum principal logarithmic strain. The strain is measured through the centre of the plate The model showed that the strains were highest at the boundary of the plate and decreased rapidly and then increased evenly towards the centre where the strain reached another peak (figure 6.5). The model over predicted the strain at the boundary. This was thought to be as a result of the sharp corner which was modelled causing a stress concentration at the boundary. In the actual machined plates the milling left a fillet radius in the corner.

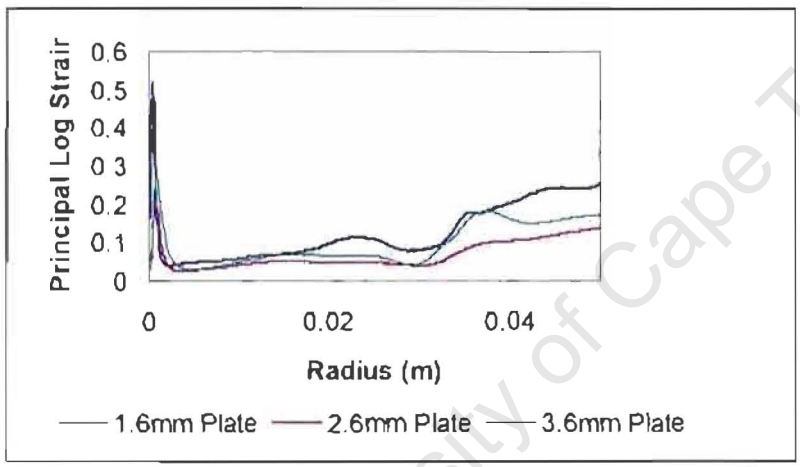

Figure 6.5 Strain distribution over the radius of the plate 1.6mm plate (T68), 2.6mm plate (X40), 3.6mm plate (P38)

d) Strain time history

The stain response over the 240μs response time for the 1.6mm plate is shown in figure 6.6. These values are measured through the centre of the plate. The strain contour plots of the time history are shown in figure 6.4. Initially the largest strain is at a radius of about the loading diameter and this trend remains for the first 30μs The strain at the centre of the plate then increases as the plastic hinge moves to the centre. By 60μs, the strain in the

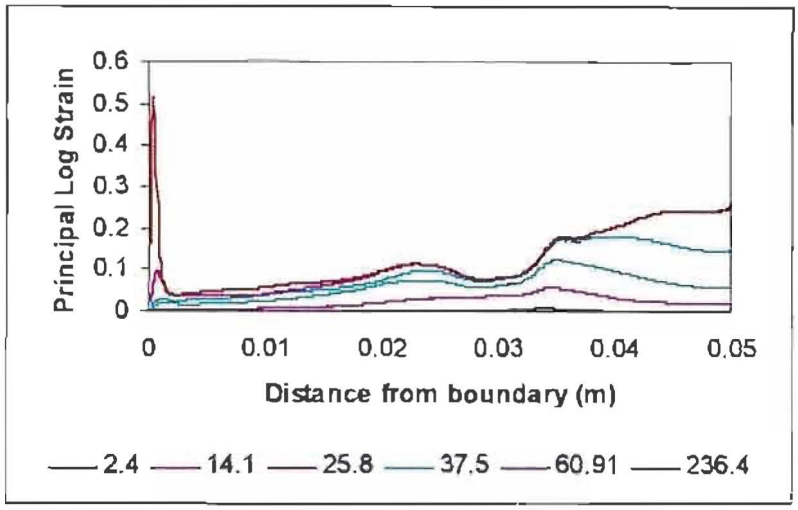

Figure 6.6 Strain time history for the 1.6mm plate (T68)

e) Through thickness strain

The strain has been found to vary through the thickness of the plate because of strain due to bending. Figure 6.7 shows the strain at various depths through the plate for the 1.6mm and 3.6mm plates. In both graphs it can be seen that the strain on the top (loaded) surface is greater than at other depths at the boundary. Along most of the plate, the strain is even through the thickness. At the middle of the plate, the strain on the bottom surface becomes greater than at other points through the thickness. It is noticeable that the difference between the strain on the top and bottom surface is greatest in the 3.6mm plate. This is because the strain differences is due to bending and the bending strain is proportional to the distance from the center line, which will be greatest for the thickest plate.

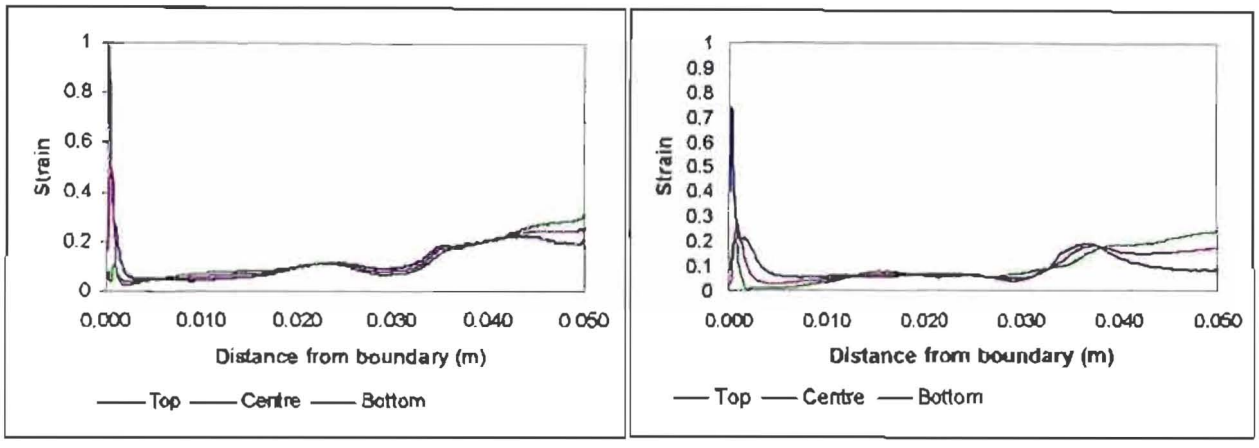

Figure 6.7 Strain across plate at different depths, a) 1.6mm plate (T68), b) 3.6mm plate (P38)

6.2.2 Failed Plates

In order to correlate the numerical models to the findings of the metallurgical investigation, the failure of the plates needed to be modelled. This would enable comparisons of the final strain states.

a) Failure

The failure is modelled using the shear failure option in ABAQUS/Explicit as described in chapter 5. A rupture strain of 1 was chosen based on the tensile tests modelled. Figure 6.8 shows the failure of the model, the failed elements are shown in blue.

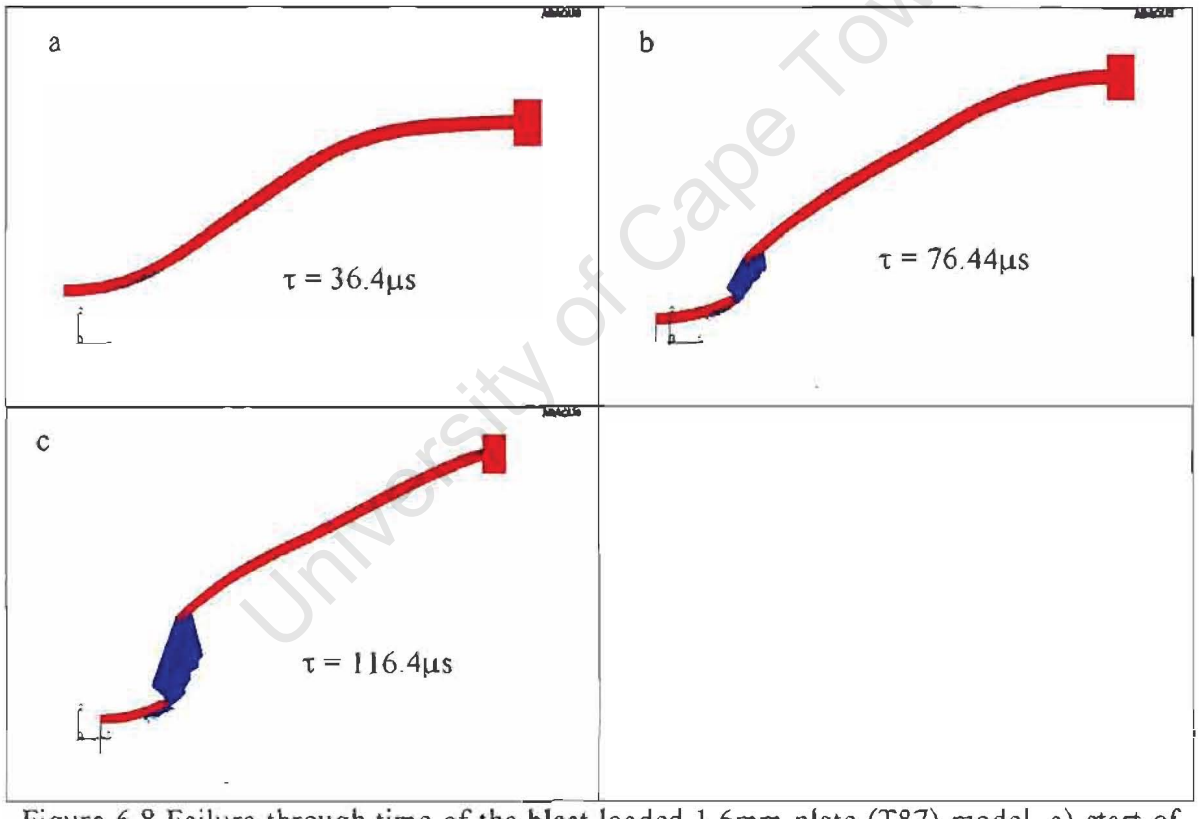

Figure 6.8 Failure through time of the blast loaded 1 6mm plate (T87) model. a) start of failure at the cap, b) cap failure, c) start of boundary failure.

It can be seen that failure at the cap starts at about 36μs The plate then fails at about 120μs at the boundary. This boundary failure does not occur in the experiments and this

failure is thought to be due the stress concentrations at the boundary due to the sharp corner. As the plate is nearly completely deformed by 110μs so the boundary failure has little effect on the overall strains modelled.

b) Deformation

The deformation of the plate before and after failure can be seen in the contour plots in figure 6.11. As with the un-failed plates it can be seen that the plates first bulges at the centre of the plate and then over the entire plate. This again corresponds to the deformation phases of Nurick and Wierzbicki.

c) Strain distribution

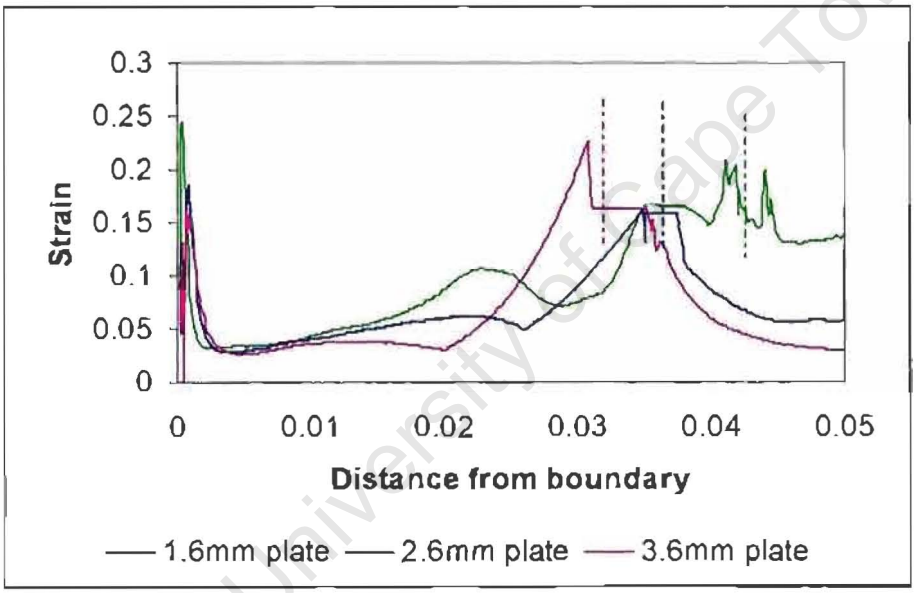

Figure 6.9 Strain distribution for the three plate thicknesses. Dotted lines show point of failure. 1.6mm plate (T87), 2.6mm plate(X32), c) 3.6mm plate (P39)

From Figure 6.9, it can be seen that the plates have their maximum strain at the area of failure at the cap radius and at the boundary. From the numerical modelling, it would appear that cap size increases with the plate thickness. It is not apparent whether this trend is as a result of the failure modelling or the geometry of the plates. The

experimental data for the cap size has a large amount of scatter and no such trends were noted there.

d) Strain time history

For the first 30μs of the deformation, the strain increases in the central region of the plate as can be seen in figure 6.10. The peak strain during this time is found on a radius approximately the same as the radius of loading. At about 30μs, the plate fails and the strain stops increasing in the centre of the plate. A plastic hinge develops at the boundary at about 100μs. The strain then increases very rapidly at the boundary and the plate fails at the boundary. This failure did not occur in the experiments and the failure of the model is thought to be due to the sharp edge boundary condition. The contour plots of the strain during the deformation process are shown in figure 6.11 where (1.6mm plate (T87), 2.6mm plate(X32), c) 3.6mm plate (P39)).

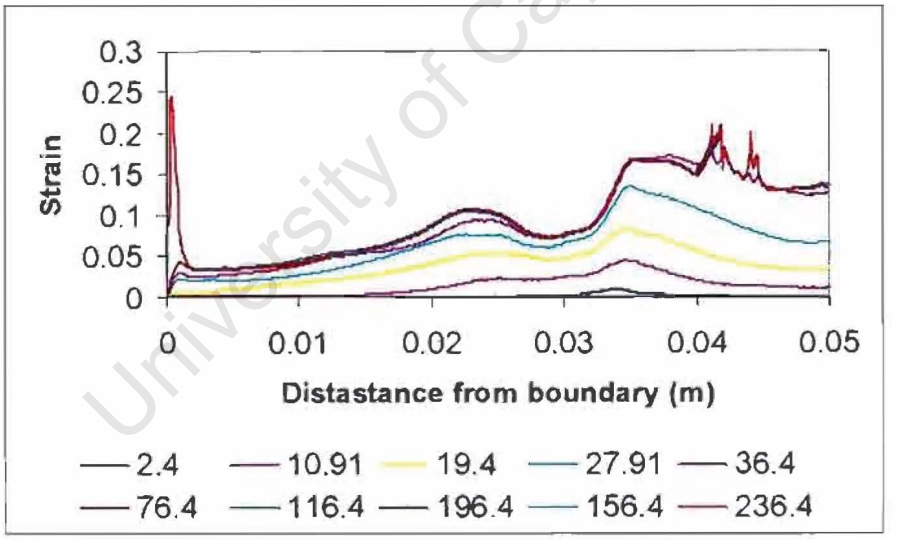

Figure 6.10 Strain time history of failed blast loaded plate. 1.6mm (T87).

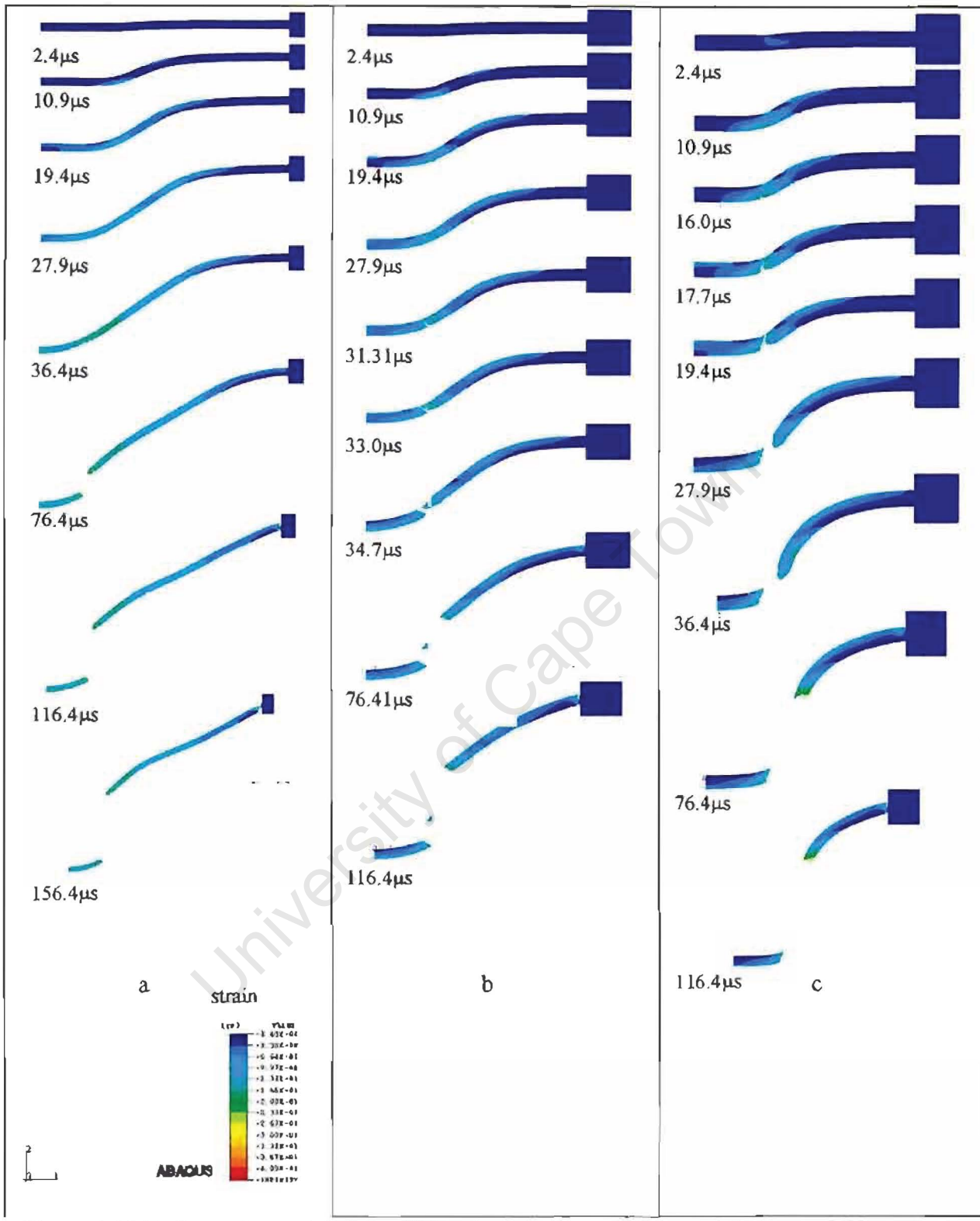

Figure 6.11 Deformation and failure of blast loaded plates. a)1.6mm, b)2 6mm, c)3.6mm.

6.3 Comparison between the Strain Profiles of the Numerical Models and that of the Metallurgical Investigation.

In order to compare the strain distribution obtained from the metallurgical investigation to the strain distribution predicted by the numerical models, the strain profiles obtained from both methods are compared on the same set of axes for each plate

6.3.1 Un-failed plates

The comparisons for the three thicknesses of unfailed plates are shown in figures 6.12-6.14. For the 1,6mm plate, the numerical prediction for the principal strain and measured values of strain showed satisfactory correlation. In both the numerical and the experimental, the strain is highest at the boundary and at the plate centre. The 3.6mm plates also show satisfactory correlation. The 2.6mm plate however shows a slightly less satisfactory correlation. The trends shown by the 2.6mm plate are similar to those predicted but the overall values of strain are measured to be much higher than the numerical model predicts.

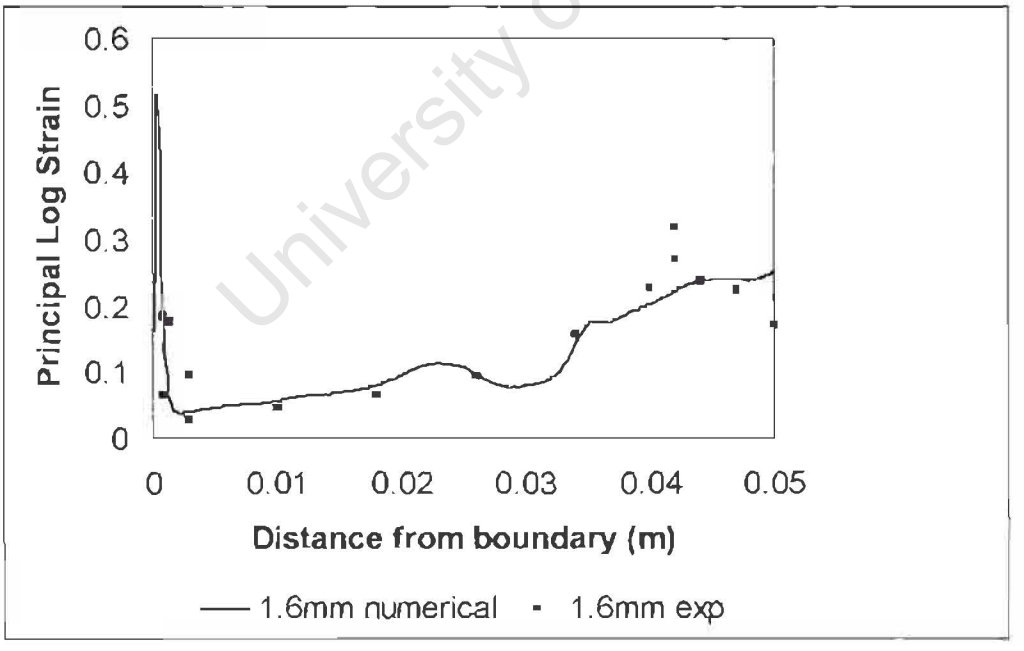

Figure 6.12 Unfailed 1.6mm plate (T68).

Figure 6.12 Unfailed 1.6mm plate (T68).

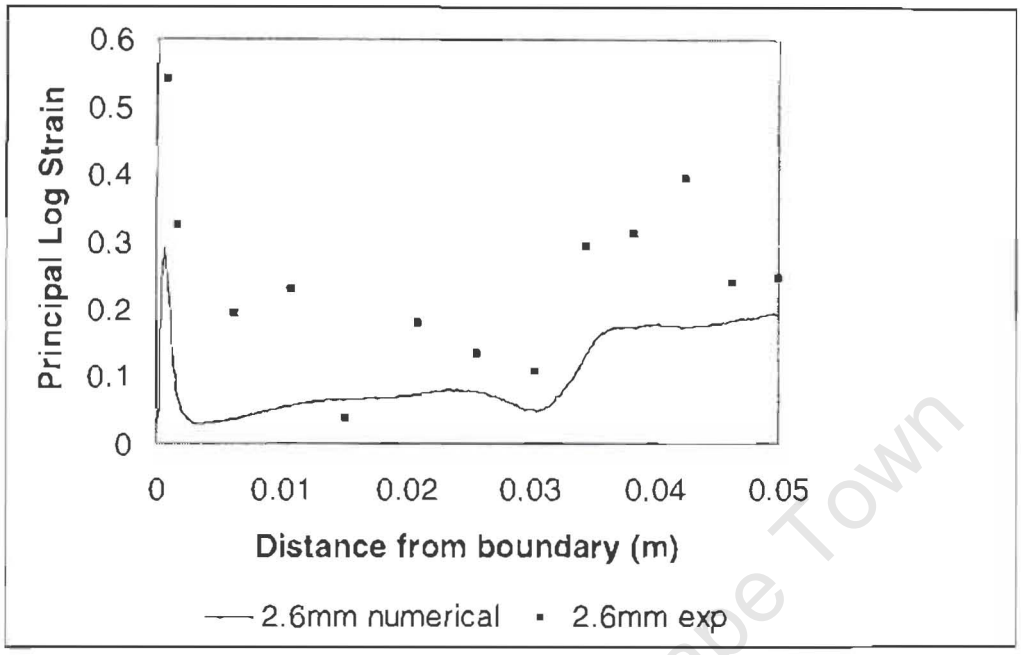

Figure 6.13 Unfailed 2.6mm plate (X40).

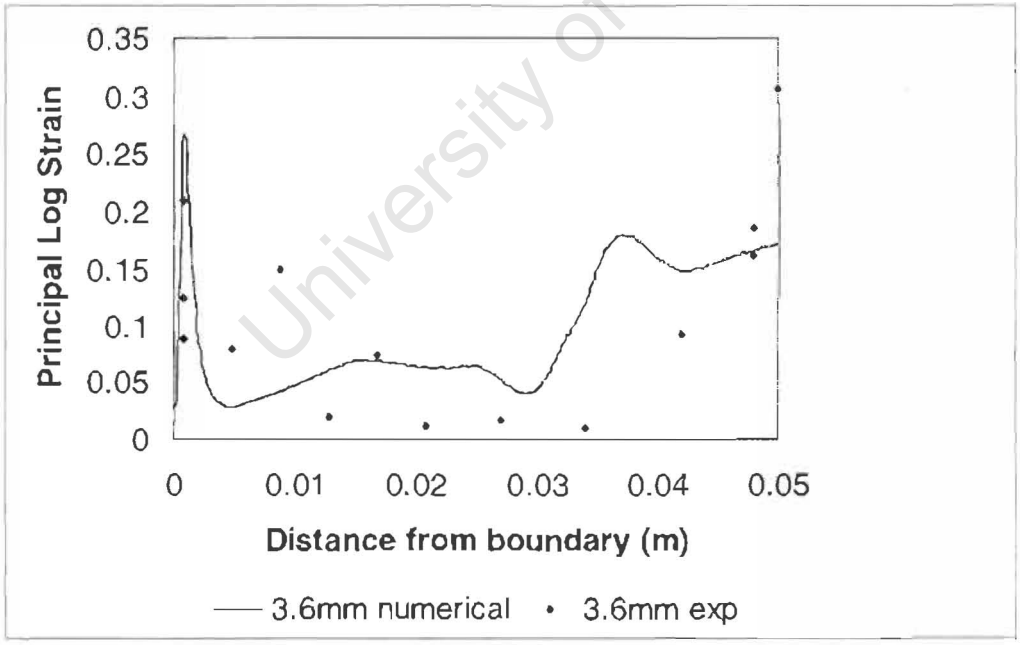

Figure 6.14 Unfailed 3.6mm plate (p38).

6.3.2 Failed Plates

The failed plates also showed good correlation for the 1.6 and 3.6mm plates. The strains near the failure at the central cap were lower in the numerical predictions than the values that were measured. This is due to the failure criterion causing failure to occur prematurely. The material model does not account for damage and softening at high strains and therefore do not soften as they do in reality. The strains measured for the 2.6mm plates are again higher than those predicted but the shape of the profile is the same.

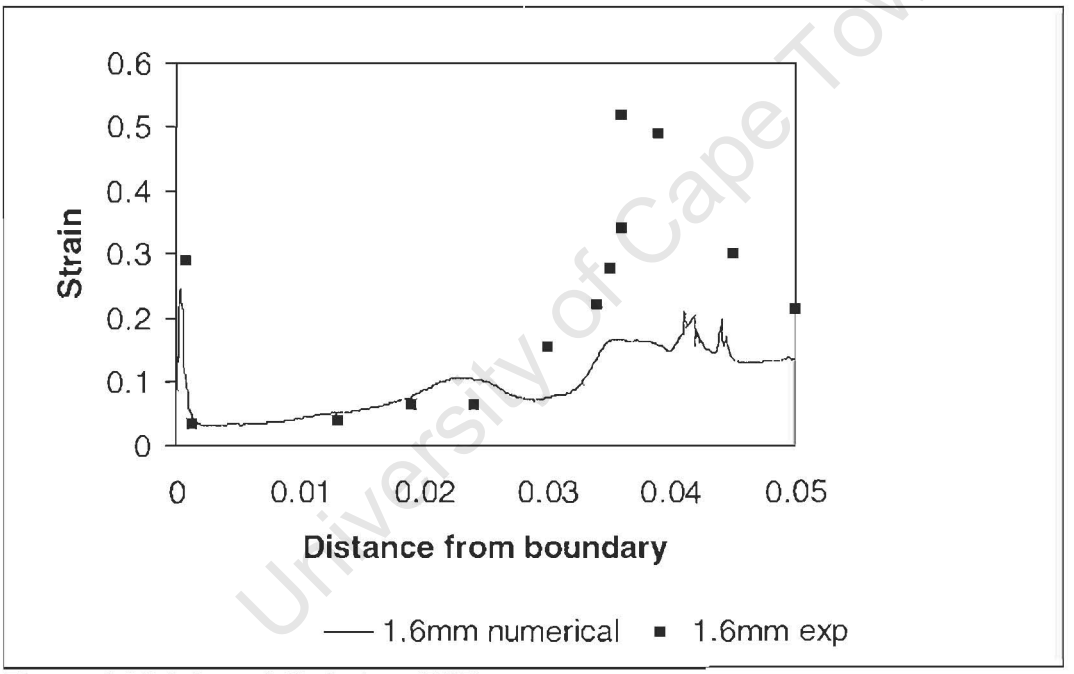

Figure 6.15 1.6mm failed plate (T87)

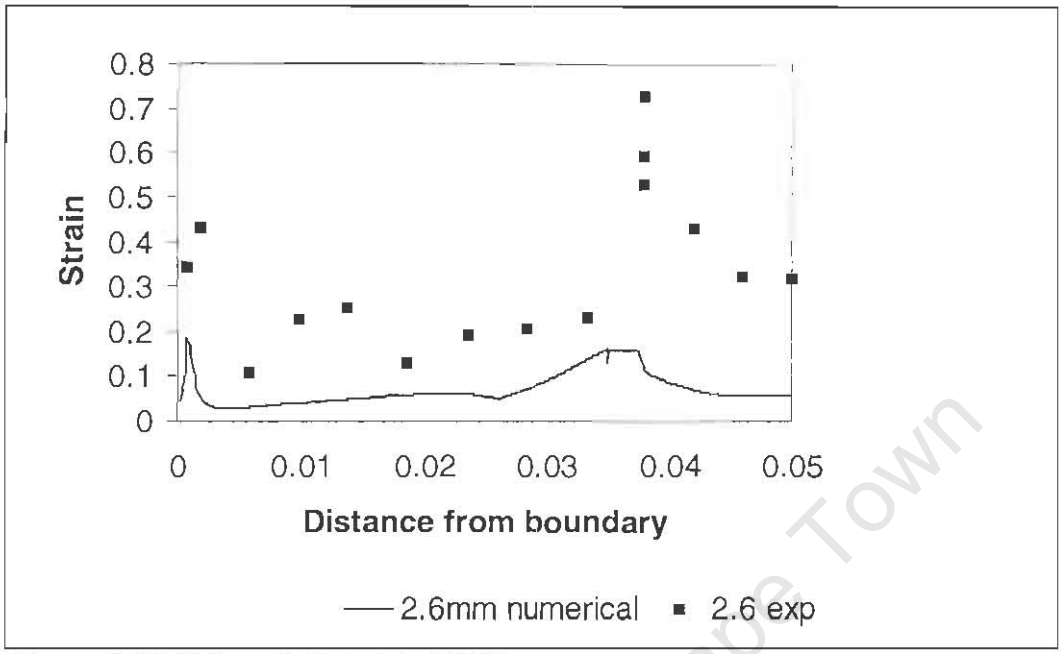

Figure 6.16. 2.6mm failed plate (X32)

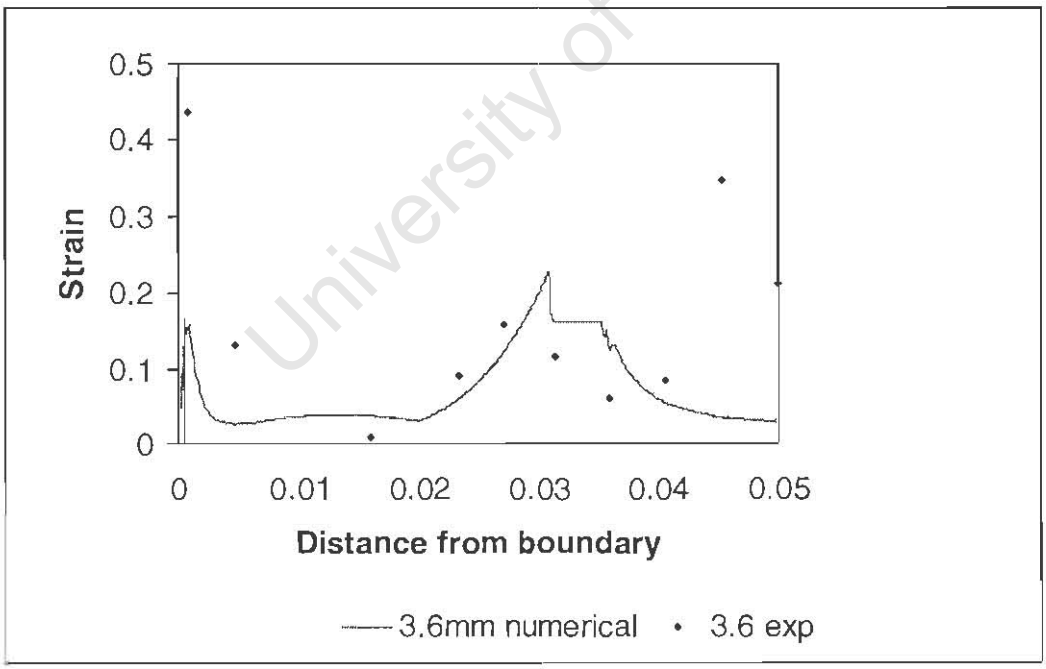

Figure 6.17. 3.6mm failed plate(P39).

CHAPTER 7

CONCLUSIONS

The results of a metallurgical and numerical investigation into the response of thin circular plates to a central localised blast load have been presented. Based on the numerical and metallurgical findings of this thesis, the following conclusions can be made:

7.1 Experimental Method (Using grain elongation as a strain measure)

A new method for measuring strain incorporating existing experimental techniques has been presented in which the grain elongation throughout a deformed metal sample is analysed and the local strain is inferred from the grain properties. This method enables the measurement of plastic strain at any material point after loading has taken place (Point *a* of objectives).

A theoretical method has been presented that relates the grain aspect ratio to the strain in the plane in which the micrograph is taken (Point *b* of objectives). The theoretical strain-aspect ratio relationship was evaluated by comparing theoretical predictions of strain from the aspect ratio to values measured from tensile tests. In these tensile tests the strain was known from the global measurement thus a comparison could be made between the strain predicted from the grain aspect ratio and the measured strain. Satisfactory correlation was found when six sampling points were used in each sample. A standard deviation of 0.1 on the aspect ratio was found. This corresponds to a deviation in the

strain measurement of 0.04. This method is intended for the measurement of large (finite) strains. It was thus decided that this method could be used as an effective means of analysing strain through a deformed structure.

The method was then used to analyse blast loaded plates. It was found to be a very useful tool with which to investigate the distribution of strain throughout the plate. The plate strain profiles showed reliable, repeatable trends and provided useful information into the plate response.

7.2 Tensile Tests

Standard quasi-static tensile tests were used as a means to verify the metallurgical experimental method as well as to investigate the modelling of strain localisation, necking and failure in a finite element program.

Comparisons between arrested experimental tensile tests and a model of the tests showed satisfactory correlation between the overall strain measured in the experiments and the strain predicted by the finite element model. The amount of overall strain required to induce localisation and necking in the model was also found to correlate very well with the experimental findings. The finite element model was thus considered to be able to adequately model strain localisation and necking in uni-axially loaded specimens.

A value for the failure strain which the finite element model would use to predict the onset of tearing was evaluated by comparing the experimentally-metallurgical strain at the failure surface and the strain predicted by the numerical model at the same point. The numerically predicted value was higher than the experimental value but due to the high degree of localisation, this was anticipated. It was decided that modelled failure strain would be used as the rupture strain predictor. The equivalent plastic strain (peeq.) and the principal strain were found to be the same in a uni-axial test, the peeq value from these tests was used. The peeq value is the rupture strain criterion used by ABAQUS.

7.3 Blast-Loaded Plates

7.3.1 Strain Profiles

The metallographic analysis provides information pertaining to the strain distribution over the plate (Point *c* of objectives). This was compared to similar data obtained from numerical models. It was found that the strain profiles obtained in these two ways compared well. For plates in which cap failure occurred, the numerical models tended to under-predict the strain around the cap. This was because the failure prediction caused the failure to occur before localisation had occurred completely at the cap in the model.

7.3.2 Elongation Distribution over the Plate

By fitting polynomials to the metallographic data, the elongation over small sections of the plate could be obtained by integration (Point *d* of objectives). This showed that at low impulses in thin (1.6mm and 2.6mm) plates, the strain distribution is fairly even with the highest values being at the centre of the plate. At higher impulses, the strain increases towards the centre of the plate and is also high at the boundary. This is because localised straining is occurring at the centre and there is a plastic hinge at the boundary. In the 3.6mm plates, it was found that the elongation occurs mostly at the centre and boundary of the plate. This is due to the greater bending effects in the thicker plates.

7.3.3 Total Elongation and Deformation Energy

The total elongation was calculated using the best-fit polynomials based on the metallographic data. The elongation predictions gave useful qualitative information. It showed how the overall elongation starts to decrease as the impulse increases in plates where cap failure occurred.

A similar method was used to evaluate the deformation energy. The strain was integrated over the entire plate and not just along a radius. Again useful qualitative information is found. It was found that the deformation energy decreases at higher impulses in plates that had failed at the cap and had petalled. Preliminary comparisons were made with theoretical energy predictions for uniformly loaded plates. This showed that for the same mid-point deflection, the deformation energy was less for localised loading than for uniform loading. This is reasonable as in central loading, most of the deformation occurs near the centre where there is a smaller perimeter and therefore less area of deformation.

7.3.4 Deformation and Strain Time Histories

The deflection time histories obtained from the numerical modelling show that the deformation of the plate does occur in two distinct phases as assumed in other studies. The numerical model showed that in the first 40μs, the deformation occurs as a central bulge and thereafter occurs over the entire plate (Point *g* of objectives).

The strain time history obtained from the numerical modelling shows that for the first 40μs the strain increases at the centre of the plate with the peak being at a radius just smaller than the loading radius. Over the last 200μs the strain increases only at the boundary

CHAPTER 8

RECOMMENDATIONS

Based on the findings of this thesis, the following recommendations are made:

Experimental

- It should be ensured that the material chosen for blast loading tests has an equiaxial grain structure to enable accurate quantitative measurements of strain from grain aspect ratio.
- It should be ensured that the grain structure of the virgin (undeformed) material of each plate specimen should be the uniform.
- The statistical variance in average grain aspect ratio data in the material should be considered in order to improve reliability of results.
- More than one micrograph should be taken at each sampling point in the material in order to reduce the uncertainty in measuring grain aspect ratios.
- Attempts should be made to measure the grain aspect ratio on two perpendicular planes in order to find the tri-axial strain state.
- Further measurements should be made of strain profile so as to further study the deformation energy under various impulses.

Numerical

- The built in boundary conditions should be carefully considered and the fillet radius at the boundary should be accurately modelled. This should prevent premature boundary failure.
- The failure criterion based on equivalent plastic strain that is used by ABAQUS is unsuitable for modelling the failure under combined loading. A failure criterion that considers the multi-axial strain state and localisation should be examined.
- Damage and softening should be incorporated into the material model.
- The plate should be modelled in three dimensions in order to consider the circumferential strains and petalling failure.

REFERENCES

1. G.N. Nurick and J.B.Martin, Deformation of thin plates subject to impulsive loading – a review part II experimental studies. Int. J. Impact Engng, 8 (2), 171-186, (1989) .
2. J. Wierzbicki and A.L. Florence, A theoretical investigation of impulsively loaded clamped circular viscoplastic plates, Int. J. Solids Struct., 6, 555-568, 1970.
3. T.A. Duffey and S.W. Key, Experimental-theoretical correlation of impulsively loaded clamped circular plates. Sandia Laboratories Research Report. No. SC-RR-68-210 (1968).
4. N. Jones, T. Uran, S.A. Tekin. The dynamic plastic behaviour of fully clamped rectangular plates. Int. J. Solid Struct., 6, 1499-1512, (1970).
5. S.R. Bodner and P.S. Symonds, Experiments on viscoplastic response of circular plates to impulsive loading. J. Mech. Phys. Solids, 27, 91-113,(1979).
6. G.N. Nurick, A new technique to measure the deflection time history of a material subject to high strain rates. Int. J. Impact Engng, 3 (1), 17-26, (1985).
7. G.N. Nurick, H.T. Pearce, J.B.Martin, The deformation of thin plates subjected to impulsive loading. Inelastic behaviour of plates and shells. (Ed. L. Bevilacqua) Springer Verlag, 597-616, 1986.
8. G.N. Nurick, H.T. Pearce, J.B.Martin, Prediction of transverse deflection and in-plane strains in impulsively loaded thin plates. Int. J. Mech. Sci. 29 (6), 435-442, 1987.
9. S.B. Menkes and H.J. Opat, Tearing and shear failure in explosively loaded clamped beams, Exp. Mech., 13, 480-486, (1973).
10. R.G. Teeling-Smith, G.N. Nurick, The deformation and tearing of circular plates subjected to impulsive loads, Int. J. Impact Engng, 11 (1), 77-92, 1991.
11. B.M. Thomas, G.N. Nurick, The effect of boundary conditions on thin plates subjected to impulsive loads, Plasticity 1995 –The 5th international symposium on plasticity and its current applications, Osaka, Japan, July 1995, 85-88.

12. G.N. Nurick, M.E. Gelman, N.S. Marshall, Tearing of blast loaded plates with clamped boundary conditions. Int. J. Impact Engng., 18 (7-8), 803-827, November 1996.
13. G.N. Nurick, A.M. Radford, Deformation and tearing of clamped circular plates subjected to localised central blast loads, Recent developments in computational and applied mechanics (ed. B.D. Reddy). A volume in honour of John B Martin, 276-301, April 1997.
14. S. Chung Kim Yuen, The effect of plate thickness on localised blast loads, BSc thesis 1997.
15. G.N. Nurick, J.B.Martin, Deformation of thin plates subject to impulsive loading – a review part I Theoretical considerations. Int. J. Impact Engng, 8 (2), 159-170, (1989).
16. G.E. Hudson, A theory of the dynamic plastic deformation of a thin diaphragm, J. Appl. Phys., 22, 1-11, 1951.
17. A.J. Wang, The permanent deflection of a plastic plate under blast loading, J. Appl. Mech., 22, 375-376, 1955.
18. D.E. Boyd, Dynamic deformation of circular membranes, AXE 92 (EM 3), 1-13, 1966.
19. D. Frederick, A simplified analysis of circular membranes subjected to an impulsive loading producing large inelastic deformations. Proc. 4th annual conf. Solid mechanics, University of Texas, 18-35, 1959.
20. J.B. Martin and P.S. Symonds, Mode approximations for impulsively loaded rigid-plastic structures. Proc. ASCE 92 (EM5), 43-66, 1966
21. J.B. Martin, Impulsive loading theorems of rigid-plastic continua. J. Engng Mech. Div. ASCE 90, 27, 1964.
22. E.H. Lee and P.S. Symonds, Large Plastic Deformations of beams under transverse impact. J. Appl. Mech. 19, 308-310, 1952.
23. H.G. Hopkins and W. Prager, The load carrying capacity of circular plates, J. Mech. Phys. Solids, 2, 1-13, 1953.
24. C. Guedes Soares, A mode solution for the finite deflections of a circular plate loaded impulsively, Rozprawy Inzynierskie Engng Trans, 29, 99-114, 1981.

25. P.S. Symonds and T. Wierzbicki, Membrane mode solution for impulsively loaded circular plates. J. Appl. Mech., 46, 58-64, 1979.
26. N. Jones, Structural Impact, Cambridge University Press, 1989.
27. T.A. Duffey, The large deflection dynamic response of clamped circular plates subject to explosive loading. Sandia Laboratories Research Report No SC-RR-67-532, 1967.
28. P.S. Westine and W.E. Baker, Energy solutions for predicting deformation in blast loaded structures. Proc. 16th Explosive safety Seminar, Hollywood Beach, Florida, 849-878, 1974.
29. N. Perrone and P. Bhadra, A simplified method to account for plastic rate sensitivity with large deformations. J. Appl. Mech., 51,505-509, 1984.
30. T. Wierzbicki and G.N. Nurick, Large deformation of thin plates under localised impulsive loading, Int. J. Impact Engng., 18 (7-8), 899-913, November 1996.
31. A.M. Radford, G.N. Nurick, ,Circular plate subjected to a localised central blast. Transient loading and response of structures, International symposium honouring Mr. Arfinn Jensenn, 1998
32. R.E. Bimha, Response of thin circular plates to central loading. 20-23, MSc thesis 1996.
33. W. Grobbelaar, Private communication.
34. M.E. Gelman, A numerical study of the response of blast loaded thin circular plates, with both clamped and integral boundary conditions. MSc Thesis 1996.
35. G.H. Farrow, G.N. Nurick, G.P. Mitchell, A Numerical study of inelastic failure of impulsively loaded circular plates, with various boundary conditions, 1st South African conference on applied mechanics '96, Gauteng, 223-234, 1996.
36. A.M. Rajendran and S.J. Bless, Determination of tensile flow stress beyond necking at very high strain rate, Exp Mech, 319-323, December 1986.
37. R. Hill, On discontinuous plastic states, with special reference to localised necking in thin sheets. J. Mech. Phys. Solids, 1, 19-30, 1952
38. P.W. Bridgman, Studies in large plastic flow and fracture, Chap 1, McGraw Hill, 1952.
39. H.L. Ewalds and R.J.H. Wanhill, Fracture Mechanics, Edward Arnold, 1984

40. A. McClintock, Qing Zhou, T. Wierzbicki, Necking in plane strain under bending with constant tension, J. Mech. Phys. Solids, 41 (8), 1327-1343, 1993.
41. A.L. Gurson, Continuum theory of ductile rupture by void nucleation and growth: Part 1- yield criteria and flow rules for porous ductile media, J. Engng. Mat. Tech.,2-15, 1977.
42. J. Lamaitre, A continuous damage mechanics model for ductile fracture. J. Engng. Mat. Tech.., 107, 85-89, 1985.
43. R. Becker, A. Needleman, O. Richmond, V. Tvergaard, Void growth and failure in notched bars, J. Mech. Phys. Solids, 36 (3), 317-351, 1988.
44. A. Needleman, V. Tvergaard, Analysis of plastic flow localisation in metals, Appl. Mech. Rev., 45 (3) (2), March 1992
45. E.A. de Souza Neto, D. Peric and P.R.J. Owen, On the numerical simulation of elasto-plastic damage at finite strains. Recent developments in computational and applied mechanics. B.D. Reddy (ed). 1997.
46. N. Jones, Structural Impact, Cambridge University Press, 327-331, 1989.
47. G.N. Nurick, R.G. Teeling-Smith. Predicting the onset of necking and hence tearing of thin plates subjected to impulsive loads – an experimental view. Structures under shock and Impact (ed P Bulson). Computational Mechanics Publications, 431-445, 1992.
48. M.D. Olson, G.N. Nurick, J.R. Fagnan, Deformation and rupture of blast loaded loaded square plates – Predictions and experiments, Int. J. Impact Engng. 13 (2), 279-291, 1993.
49. Wei Qin Shen and N. Jones, Dynamic response and failure of fully clamped circular platesunder impulsive loading. Int. J. Impact Engng., 13 (2), 1993
50. M. Ohashi, Quantitative metallographic study for evaluation of fracture strain. Exp. Mech., 38 (1), 13-17, March 1998.
51. M.T. Postek, K.S. Howard, A.H. Johnson, K.L. McMichael, Scanning Electron Microscope – A students handbook.
52. Joyce-Loebel image analysis practice and principals, A technical handbook, pg 45.
53. Hibbitt, Karlson & Sorensen Inc. ABAQUS Theory Manual. v5.7
54. Hibbitt, Karlson & Sorensen Inc. ABAQUS /Explicit User Manual. v5.7

55. Hibbitt, Karlson & Sorensen Inc. ABAQUS /Explicit on line documentation, sect 10, v5.8

56. Hibbitt, Karlson & Sorensen Inc. ABAQUS /Explicit on-line documentation, Keywords, sect 3, v5.8

57. W. Grobbelaar, Modelling of Fragmentation Damage, B.Sc Thesis,1996.

APPENDIX I

EXPERIMENTAL DATA

RESULTS OF BLAST TESTS

Specimen	Mass of Explosive	Height of Explosive	Thickness	Impulse	ϕ_c	Mass PE4/ Impulse	Mid Point Deflection	deflection/ thickness	Burn Diameter	Inflection Diameter	Cap Diameter	Comment
	g	*mm*	*mm*	*Ns*			*mm*		*mm*	*mm*	*mm*	
T68 (c)*	5	4.330	1.56	8.800	35.401	0.568	24.50	15.705	47.8	33.6	0	Mode I deformation
T65 (a)*	5.5	4.763	1.57	9.482	37.661	0.580	24.70	15.732	44.6	31.3	0	Mode I deformation
T73	5.5	4.763	1.35	9.482	50.936	0.580	0.00	0.000	46.25		29.63	Petalling
T76 (b)*	5.6	4.850	1.59	10.328	39.996	0.542	0.00	0.000	48.1	35.6	23.23	Capping + shear over part of Boundary
T86 (d)*	5.8	5.023	1.49	10.798	47.618	0.537	0.00	0.000	48		31.01	Petalling - Disregard cap diameter
T87 (e)*	6	5.196	1.50	10.476	45.583	0.573	0.00	0.000	46.4		0	Petalling - Disregard cap diameter

Table I.I Test data for 33mm loaded diameter 1.6mm thick plates. [14] * Denotes the stub number of the plates which were used for microstructural analysis

Specimen	Mass of Explosive	Height of Explosive	Thickness	Impulse	ϕ_c	Mass PE4/ Impulse	Mid Point Deflection	deflection/ thickness	Burn Diameter	Inflection Diameter	Cap Diameter	Comment
	g	*mm*	*mm*	*Ns*			*mm*		*mm*	*mm*	*mm*	
X41	7	6.062	2.55	12.034	17.446	0.582	20.06	7.867	53.7	25.9	0	Mode I deformation
X43 (k)*	8.5	7.362	2.57	14.344	20.473	0.593	22.80	8.872	53.3	30.2	0	Mode I deformation
X40 (l)*	10	8.661	2.51	16.922	25.322	0.591	26.07	10.386	55.1	27.4	0	Onset Tearing at Boundary
T2 (m)*	10.5	9.094	2.55	16.963	25.539	0.619	28.10	11.020	60.1	30.8	0	Mode I def. + onset capping
X32 (n)*	10.75	9.310	2.56	17.983	25.869	0.598	0.00	0.000	61.7	30.5	22.53	Capping
X37	11	9.527	2.53	17.594	25.912	0.625	0.00	0.000	62.4	30.5	23.68	Capping
P35 (o)*	12	10.393	2.53	19.514	29.250	0.615	0.00	0.000	66.6	30.5	23.95	Capping

Table I.2 Test Data for 33mm loaded diameter 2.6mm thick plates.[14] * Denotes the stub number of the plates which were used for microstructural analysis

Specimen	Mass of Explosive	Height of Explosive	Thickness	Impulse	ϕ_c	Mass PE4/ Impulse	Mid Point Deflection	deflection/ thickness	Burn Diameter	Inflection Diameter	Cap Diameter	Comment
	g	*mm*	*mm*	*Ns*			*mm*		*mm*	*mm*	*mm*	
T64	10	8.661	3.50	15.808	12.634	0.633	19.98	5.709	58.3	26	0	Mode I deformation
P38 (f)*	13	11.259	3.60	20.535	15.202	0.633	21.84	6.067	62.6	30.4	0	Mode I deformation
T4 (g)*	17	14.723	3.60	25.330	19.567	0.671	27.10	7.612	64	32	0	Mode I def. + localised @ cap
T27 (h)*	20	17.321	3.64	29.037	21.456	0.689	26.04	7.154	68.2	29.4	0	Mode I + onset Tearing @ boundary
T84 (i)*	23	19.919	3.56	31.333	24.205	0.734	28.86	8.107	68.9	28.7	0	Mode I + trace tearing @ Boundary
P39 (j)*	24	20.785	3.39	32.918	27.481	0.729	0.00	0.000	0	28.7	24.17	Petalled + part tearing @ Boundary
T1	25	21.652	3.52	34.234	27.050	0.730	0.00	0.000	73.2	28.7	-	Petalled

Table I.3 Test Data for 33mm loaded diameter 3.6mm thick plates [14] * Denotes the stub number of the plates which were used for microstructural analysis

APPENDIX II

DERIVATIONS AND CALCULATIONS

Derivation of the Relationship between aspect ratio and strain.

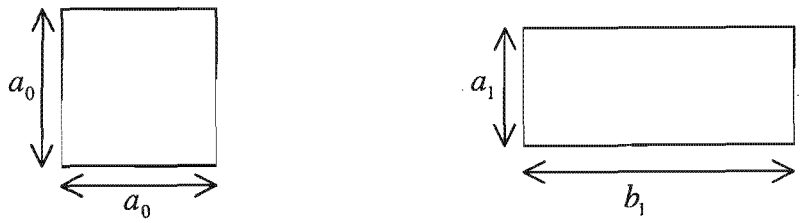

Figure II.1 a) Undeformed grain, b) Deformed grain

The area of the grain is assumed constant and is given as:

$$A = a_0^2 = a_1 b_1 \tag{4.1}$$

The strain in the grain is:

$$\varepsilon^{gr} = \ln\left(\frac{b_1}{a_0}\right) \tag{4.2}$$

and grain aspect ratio is defined as:

$$\alpha_r = \frac{b_1}{a_1} \tag{4.3}$$

Equating these three equations, to relate aspect ratio to strain:

We have from eqn 4.1:

$$a_0 = \sqrt{a_1 b_1}$$

then using eqn 4.2:

$$\varepsilon^{gr} = \ln\left(\frac{b_1}{\sqrt{a_1 b_1}}\right) = \ln\left(\sqrt{\frac{b_1}{a_1}}\right) = \frac{1}{2}\ln\left(\frac{b_1}{a_1}\right)$$

and substituting in eqn 4.3 we have:

$$\varepsilon^{gr} = \frac{1}{2}\ln(\alpha_r) \qquad (4.4)$$

$$\text{or} \quad \alpha_r = e^{2\varepsilon^{gr}} \qquad (4.5)$$

This relationship (eqn. 4.5) is plotted below:

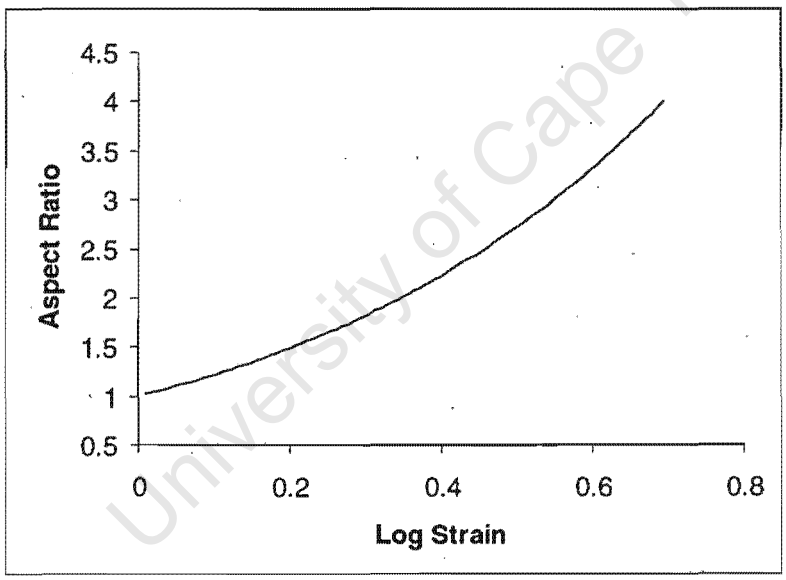

Figure II.2 Theoretical relationship between aspect ratio and strain

Calculations of Theoretical Total Elongation

The equation for the calculation of elongation based on the average predicted strain is:

$$\Delta l = \frac{I^2}{R^4 t^2 \rho \sigma_0}, 0.07986.R$$

So for example for the 8.8Ns inpulse, 1.6mm plate the predicted elongation would be:

$$\Delta l = \frac{8.8^2}{0.05^4 0.0016^2 7600.850E6} 0.07986.0.05$$

which gives: $\Delta l = 0.00299mm$

All the results are given below:

Table II.1 Theoretical Elongation Predictions.

Plate	Thickness	Impulse	Elongation
	(mm)	Ns	(mm)
T68	1.6	8.8	2.99
T65	1.6	9.5	3.47
X43	2.6	14.3	2.99
X40	2.6	16.2	4.17
P38	3.6	20.5	3.22
T4	3.6	25.33	4.89

APPENDIX III

TENSILE TEST

DATA

Graphs of the Tensile Test Results

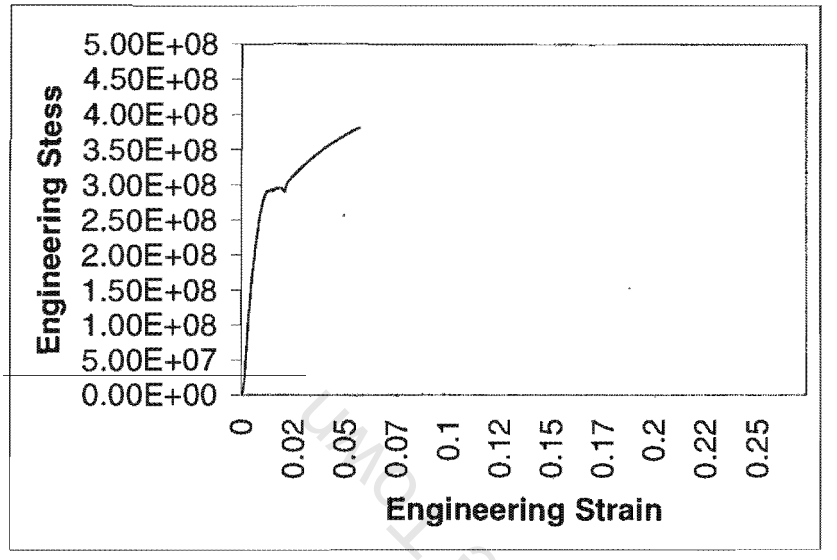

Figure III.1 Tensile test 1: 0.046 strain.

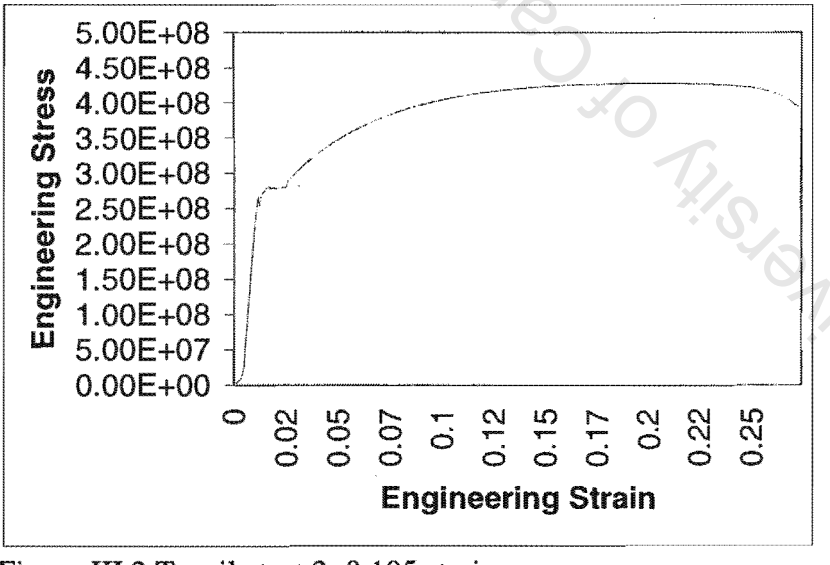

Figure III.2 Tensile test 2: 0.105 strain

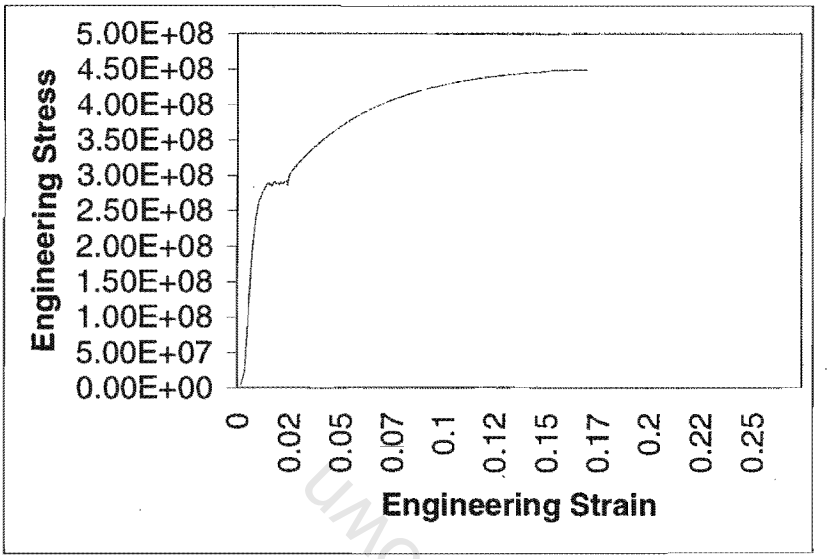

Figure III.3 Tensile test 3: 0.174 strain

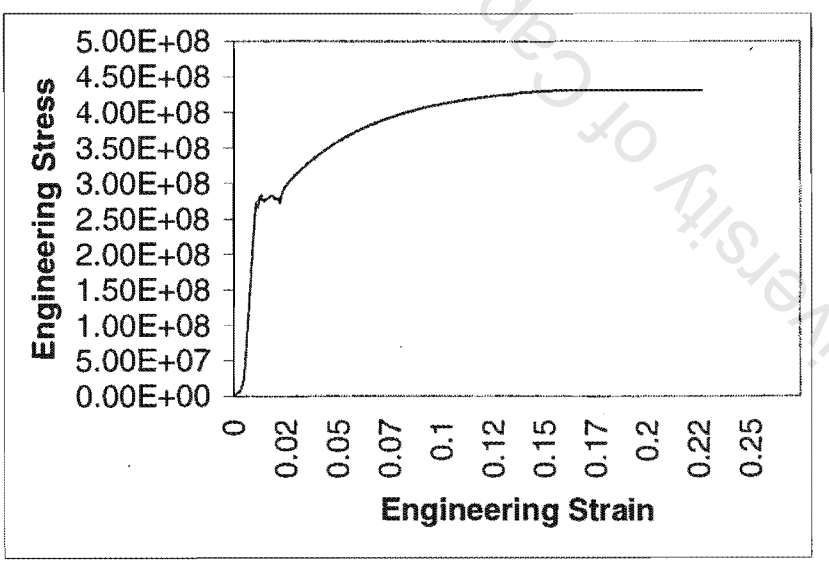

Figure III.4 Tensile test 4: 0.234 strain

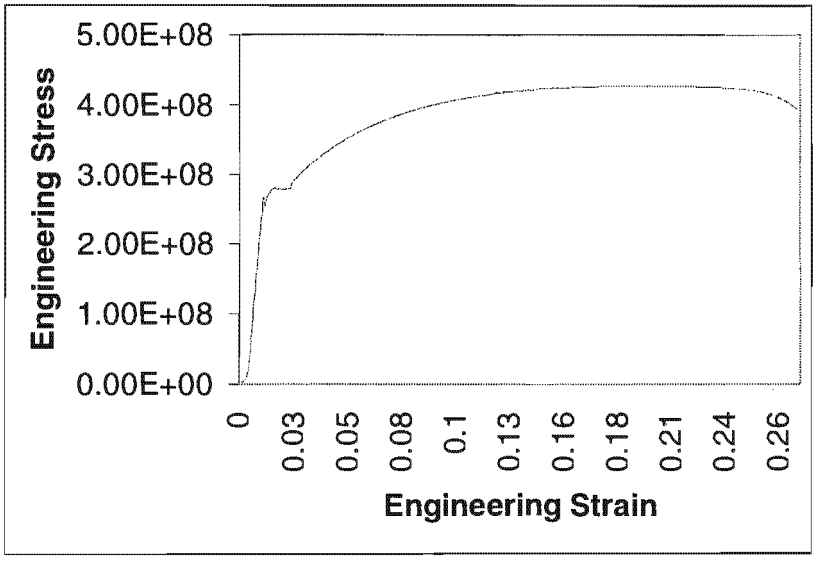

Figure III.5 Tensile test 5: 0.272 strain

Mictostructural Analysis of Tensile Tests.

Test #	Test 1	Test 2	Test 3	Test 4
Strain Applied	0.046	0.105	0.174	0.234
Aspect Ratio From Micrograph	1.17	1.16	1.41	1.47
	1.18	1.16	1.33	1.55
	0.76	1.00	1.20	1.57
	1.30	1.12	1.59	1.35
	1.12	1.16	1.41	1.39
	1.00	1.10	1.55	1.37
			1.29	1.58
Mean	1.09	1.12	1.40	1.47

Table III.1 Microstructural tensile test data

Theoretical Strain- Aspect ratio relationship

$\alpha_r = e^{2\varepsilon^{gr}}$

eg for 0.105 applied strain:

$\alpha = e^{2\times 0.105} = 1.23$

Strain	0.046	0.105	0.174	0.234
Aspect Ratio	1.10	1.23	1.41	1.59

APPENDIX IV

PLATE MICROSTRUCTURAL DATA

Possition along Radius (m)	Grain Aspect Ratio	Strain	Orientation (Degrees)	Position through Thickness (Centre unless Stated)
Plate T65 (a) 1.6mm				
-0.0018	0.9547	-0.0232	9.4932	
-0.0018	1.0417	0.0204	3.9142	
0.0003	1.5741	0.2268	21.9381	t (op)
0.0003	1.4879	0.1987	5.9758	b(ottom)
0.0007	1.1623	0.0752	0.7150	b
0.0007	2.6102	0.4797	29.7409	t
0.0012	2.0989	0.3707	29.0907	t
0.0012	1.4090	0.1715	34.4845	b
0.0027	1.4451	0.1841	22.2338	b
0.0027	1.5269	0.2116	30.8453	t
0.0110	1.6433	0.2483	26.6269	t
0.0110	1.7318	0.2746	17.6166	b
0.0129	1.0520	0.0254	-24.9724	b
0.0129	0.7895	-0.1182	-16.4390	t
0.0237	0.8787	-0.0646	-21.2555	b
0.0237	1.9244	0.3273	15.6630	t
0.0259	1.9726	0.3397	12.4874	b
0.0259	2.1185	0.3754	1.0393	t
0.0375	2.6012	0.4780	25.8645	b
0.0375	2.4666	0.4514	16.5610	t
0.0393	2.1960	0.3933	22.3743	t
0.0393	2.3718	0.4318	17.0785	b
0.0455	2.1972	0.3936	18.7942	
0.0500	1.6708	0.2566	-2.8341	

Possition along Radius Plate T76 (b)	Grain Aspect Ratio 1.6mm	Strain	Orientation	Position through Thickness
-0.0020	1.4622	0.1900	6.0946	
-0.0020	1.1238	0.0584	13.1300	
0.0008	1.3772	0.1600	16.8549	b
0.0008	2.3652	0.4304	30.1867	t
0.0018	1.9492	0.3337	28.1904	
0.0018	0.7091	-0.1719	5.9376	
0.0090	1.4030	0.1693	16.0564	
0.0175	1.3042	0.1328	12.5939	
0.0200	1.3042	0.1328	12.5939	
0.0280	1.3042	0.1328	12.5939	
0.0365	2.4308	0.4441	8.4352	
0.0425	1.8747	0.3142	14.8796	t
0.0425	2.4767	0.4535	16.3543	b
0.0435	3.2009	0.5817	20.9524	b
0.0435	3.1062	0.5667	11.8043	t

Possition along Radius Plate T68 (c)	Grain Aspect Ratio 1.6mm	Strain	Orientation	Position through Thickness
-0.0020	0.7471	-0.1458	1.2075	
-0.0020	0.6596	-0.2080	0.7925	
0.0008	0.6648	-0.2042	0.7612	
0.0008	1.1388	0.0650	1.4168	
0.0008	1.4556	0.1877	1.9953	
0.0013	1.4265	0.1776	1.6865	
0.0005	0.9840	-0.0081	1.4631	
0.0028	1.2096	0.0951	1.7457	
0.0028	1.0575	0.0279	1.0944	
0.0100	1.0929	0.0444	1.0654	
0.0180	1.1395	0.0653	1.6555	
0.0260	1.2068	0.0940	1.5685	
0.0340	1.3751	0.1593	1.7222	
0.0400	1.5794	0.2285	1.9101	
0.0410	1.9834	0.3424	2.5372	
0.0420	1.8936	0.3192	2.2919	
0.0420	1.7173	0.2704	1.5002	
0.0440	1.6177	0.2405	1.2829	
0.0440	1.5975	0.2342	1.4893	
0.0470	1.2184	0.0988	1.5833	
0.0470	1.5672	0.2247	1.2917	
0.0500	1.2556	0.1138	1.2678	
0.0500	1.4027	0.1692	1.2184	

Possition along Radius	Grain Aspect Ratio	Strain	Orientation	Position through Thickness
Plate T86 (d)	1.6mm			
0.0008	1.1719	0.0793	1.2480	
0.0008	1.8430	0.3057	2.0030	
0.0008	2.2229	0.3994	1.7183	
0.0020	1.3895	0.1645	0.9601	
0.0070	1.2962	0.1297	0.8848	
0.0120	1.1011	0.0482	1.0359	
0.0170	1.1605	0.0744	0.9023	
0.0220	1.8350	0.3035	1.5381	
0.0260	1.3797	0.1609	1.3504	
0.0290	1.8935	0.3192	1.7510	
0.0320	1.8308	0.3024	1.7474	
0.0350	1.6652	0.2550	1.4884	
0.0380	1.9748	0.3402	1.9453	
0.0410	1.9339	0.3298	1.6674	
0.0440	1.6522	0.2511	1.6303	
0.0470	1.3172	0.1378	1.1993	

Possition along Radius	Grain Aspect Ratio	Strain	Orientation	Position through Thickness
Plate T87 (e)	1.6mm			
-0.0020	1.0220	0.0109	1.1625	
0.0008	0.9767	-0.0118	1.1842	
0.0008	1.7897	0.2910	1.8986	
0.0013	1.0721	0.0348	1.2619	
0.0070	0.8549	-0.0784	1.1690	
0.0130	1.0850	0.0408	1.4457	
0.0190	1.1418	0.0663	1.1585	
0.0240	1.1421	0.0665	1.0815	
0.0300	1.3722	0.1582	1.4860	
0.0340	1.5606	0.2225	1.6518	
0.0350	1.7465	0.2788	1.5919	
0.0360	2.8208	0.5185	2.8356	
0.0360	1.9833	0.3424	1.4426	
0.0390	2.6664	0.4904	2.4361	
0.0450	1.8242	0.3006	1.7259	
0.0500	1.5375	0.2151	1.3859	

Possition along Radius Plate X43 (k)	Grain Aspect Ratio 2.6mm	Strain	Orientation	Position through Thickness
0.0007	1.5055	0.2046	-4.0331	
0.0007	2.3420	0.4033	-19.2414	
0.0016	0.6257	-0.2737	-5.5717	
0.0053	1.1755	0.1810	6.2161	
0.0086	1.4014	0.0726	0.7094	
0.0122	1.1591	-0.0072	-7.4562	
0.0157	1.4763	0.1247	-0.8262	
0.0191	1.4923	0.2040	0.3937	
0.0227	1.3615	0.1599	3.5752	
0.0264	1.2737	0.1391	7.4967	
0.0300	1.4629	0.1987	4.9652	
0.0336	1.8435	0.3243	9.0651	
0.0391	1.3492	0.1926	5.9926	
0.0436	1.5598	0.2182	9.3406	
0.0473	1.8640	0.2726	7.5379	
0.0500	1.7650	0.2397	5.9489	

Possition along Radius Plate X40 (I)	Grain Aspect Ratio 2.6mm	Strain	Orientation	Position through Thickness
0.0008	2.9215	0.5424	31.2208	
0.0008	0.9040	-0.1517	-1.5260	
0.0017	1.8493	0.3271	29.7567	
0.0062	1.1521	0.1945	13.4797	
0.0107	1.3102	0.2312	8.7240	
0.0151	1.1856	0.0386	10.8688	
0.0209	1.5239	0.1803	7.8528	
0.0257	1.2690	0.1333	15.2260	
0.0304	1.4068	0.1076	12.0055	
0.0344	1.5657	0.2951	9.5660	
0.0384	1.5411	0.3156	6.5289	
0.0425	1.8558	0.3962	4.9880	
0.0462	1.5006	0.2412	9.1954	
0.0500	1.4429	0.2467	11.8035	

Possition along Radius Plate T2 (m)	Grain Aspect Ratio 2.6mm	Strain	Orientation	Position through Thickness
0.0008	2.2618	0.3432	25.3065	
0.0008	0.5370	-0.3109	15.0657	
0.0018	2.1299	0.4298	38.2925	
0.0058	1.1243	0.1078	6.0739	
0.0098	1.3772	0.2270	13.4865	
0.0138	1.2998	0.2535	4.2364	
0.0186	1.3435	0.1286	10.0737	
0.0235	1.3916	0.1916	17.7772	
0.0284	1.4325	0.2051	5.2844	
0.0334	1.5766	0.2308	-3.8123	
0.0380	4.4196	0.7292	17.7534	
0.0380	2.6582	0.5946	16.8336	
0.0380	2.1935	0.5279	18.8120	
0.0420	1.5516	0.4309	9.2536	
0.0460	1.4954	0.3232	17.3326	
0.0500	1.7955	0.3196	20.5555	

Possition along Radius Plate X32 (n)	Grain Aspect Ratio 2.6mm	Strain	Orientation	Position through Thickness
0.0008	3.2536	0.5741	27.7091	
0.0008	2.4981	0.4487	29.5056	
0.0008	0.7944	0.0817	7.6616	
0.0030	1.4436	0.2248	17.0606	
0.0075	1.1793	0.1663	9.7950	
0.0120	1.0642	0.2150	9.7902	
0.0165	1.3393	0.2061	0.5002	
0.0210	1.3151	0.2587	-6.2122	
0.0250	1.3909	0.2880	6.2886	
0.0290	1.8868	0.2959	6.8984	
0.0330	1.7299	0.2999	17.1498	
0.0370	1.6824	0.3408	23.5563	
0.0410	1.8123	0.3446	18.1373	
0.0440	2.4150	0.4820	18.1802	
0.0450	4.1240	0.6962	16.7028	
0.0500	1.7982	0.3242	14.1964	

Possition along Radius	Grain Aspect Ratio	Strain	Orientation	Position through Thickness
Plate O35 (o)	2.6mm			
0.0008	2.0150	0.3113	27.8254	
0.0008	0.6447	-0.1721	3.3313	
0.0018	1.0614	-0.0995	11.2474	
0.0071	1.0079	-0.0127	-1.4242	
0.0125	1.1357	0.1278	8.8929	
0.0178	1.5057	0.2317	8.9665	
0.0228	1.4178	0.1853	7.4270	
0.0268	0.9966	0.0939	0.1001	
0.0308	1.1860	0.1442	12.5098	
0.0348	1.5921	0.2625	0.4856	
0.0388	1.9878	0.3033	12.6518	
0.0428	2.7365	0.4677	9.1350	
0.0434	2.8702	0.5404	5.6570	
0.0444	2.2976	0.4750	8.4255	
0.0484	2.0161	0.3599	16.3686	
0.0500	1.6088	0.2260	9.4838	

Possition along Radius	Grain Aspect Ratio	Strain	Orientation	Position through Thickness
Plate P38 (f)	3.6mm			
0.8000	1.5219	0.2100	2.7213	b
0.8000	1.1939	0.0886	6.3215	
0.8000	1.2825	0.1244	-1.2224	t
4.8000	1.1722	0.0794	-6.1132	
8.8000	1.3482	0.1494	-0.5089	
12.8000	1.0396	0.0194	9.8251	
16.8000	1.1597	0.0741	-5.4749	
20.8000	1.0229	0.0113	8.5995	
48.0000	1.4526	0.1867	1.1617	b
50.0000	1.8443	0.3061	1.1782	
48.0000	1.3838	0.1624	3.2393	
42.0000	1.2045	0.0930	-3.8781	
34.0000	1.0202	0.0100	1.1845	
27.0000	0.8774	-0.0654	-0.1113	b
27.0000	1.0328	0.0161	-1.4776	t

Possition along Radius Plate T4 (g)	Grain Aspect Ratio 3.6mm	Strain	Orientation	Position through Thickness
-2.0000	1.0270	0.0133	20.6816	b
0.8000	1.1071	0.0509	17.4511	b
0.8000	3.0150	0.5518	41.2165	t
1.3000	1.2681	0.1188	8.7422	b
1.3000	2.3476	0.4267	36.9008	
6.4000	1.5061	0.2048	2.2409	
11.5000	1.1036	0.0493	-9.4525	
17.2000	1.2139	0.0969	-3.4642	
22.0000	2.0687	0.3635	3.1527	
27.0000	1.6500	0.2504	4.2701	
32.0000	1.6061	0.2369	0.4112	
37.0000	1.6311	0.2446	3.7141	
42.0000	2.9600	0.5426	3.2434	
47.0000	1.9079	0.3230	-2.3352	
52.0000	1.8871	0.3175	3.5333	
47.0000	1.6496	0.2503	-1.2797	b

Possition along Radius Plate T27 (h)	Grain Aspect Ratio 3.6mm	Strain	Orientation	Position through Thickness
-2.0000	0.9397	-0.0311	-5.0974	
0.8000	0.8252	-0.0961	2.5470	b
0.8000	2.3964	0.4370	25.9652	t
5.0000	1.2972	0.1301	3.7752	
9.2500	0.9849	-0.0076	-2.2176	
13.5000	0.9394	-0.0313	6.9402	
17.0000	1.0165	0.0082	17.7546	
25.0000	1.1998	0.0911	7.8052	
29.0000	1.3706	0.1576	6.1564	
33.5000	1.2620	0.1163	3.2698	
38.5000	1.1280	0.0602	6.0149	
43.5000	1.1859	0.0853	3.9625	
48.5000	2.0065	0.3482	-0.0164	
50.0000	1.5294	0.2124	4.8910	

Possition along Radius Plate T84 (i)	Grain Aspect Ratio 3.6mm	Strain	Orientation	Position through Thickness
0.7000	0.8688	-0.0703	8.5525	b
0.7000	2.1387	0.3801	44.9550	
0.7000	2.4122	0.4403	36.1825	t
1.9000	1.4530	0.1868	18.5747	
9.0000	1.5633	0.2234	19.3837	
14.6000	1.5148	0.2076	15.1774	
20.4000	1.0382	0.0188	-14.8366	
26.0000	1.2326	0.1046	5.0721	
30.0000	1.6263	0.2432	13.5279	
31.5000	1.2111	0.0958	7.1594	
37.2000	1.4550	0.1875	10.7994	
42.7000	1.9942	0.3451	11.1849	
48.2000	2.1377	0.3799	13.4767	
50.0000	1.6459	0.2491	8.7841	

Possition along Radius Plate P39 (j)	Grain Aspect Ratio 3.6mm	Strain	Orientation	Position through Thickness
0.9000	3.3385	0.6028	8.0413	t
0.9000	1.9897	0.3440	15.9650	
0.9000	1.6940	0.2636	8.0672	b
1.4000	2.2516	0.4058	6.2773	t
6.7000	1.5924	0.2326	2.2829	b
6.7000	1.8095	0.2965	5.5895	t
12.0000	1.2821	0.1242	4.1192	
17.3000	1.2483	0.1109	4.7567	
22.6000	1.1335	0.0627	2.6361	
27.5000	1.3071	0.1339	17.5351	
31.7000	1.2068	0.0940	16.1612	
35.9000	1.6234	0.2423	12.0453	
40.1000	1.3141	0.1366	11.5425	
44.3000	1.7625	0.2834	11.1611	
46.0000	2.2085	0.3962	10.3286	
50.0000	2.1382	0.3800	14.9230	

Strain Distribution along Plate Radius

1.6mm Plates

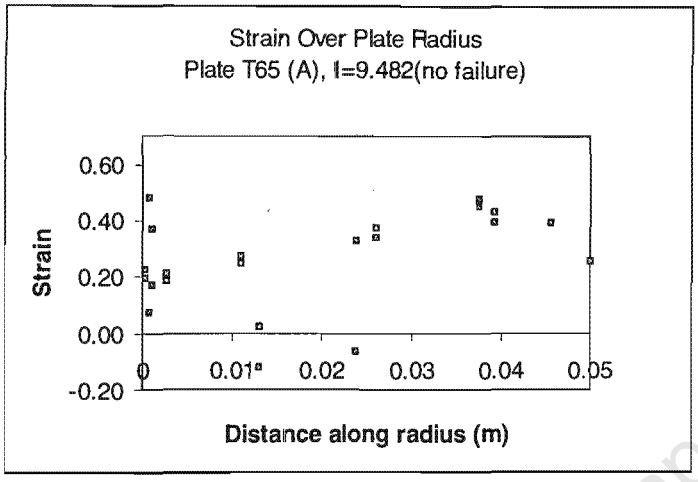

Figure IV.1 Strain Distribution Plate T65

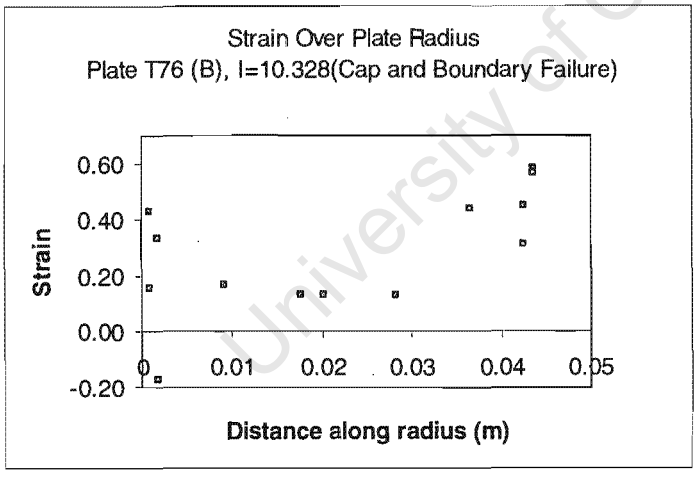

Figure IV.2 Strain Distribution Plate T76

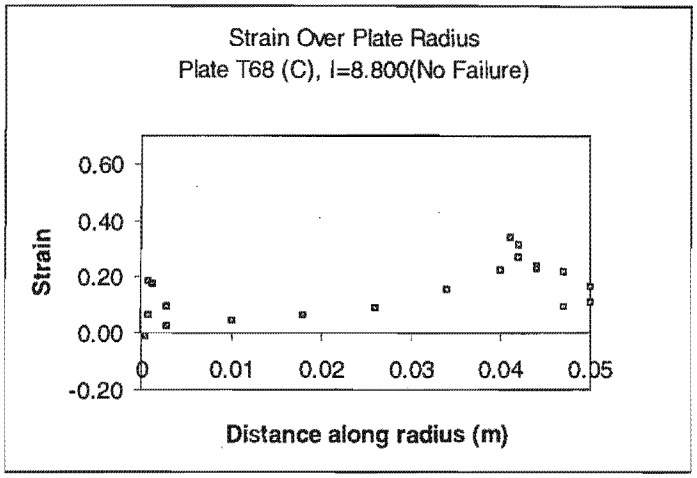

Figure IV.3 Strain Distribution Plate T68

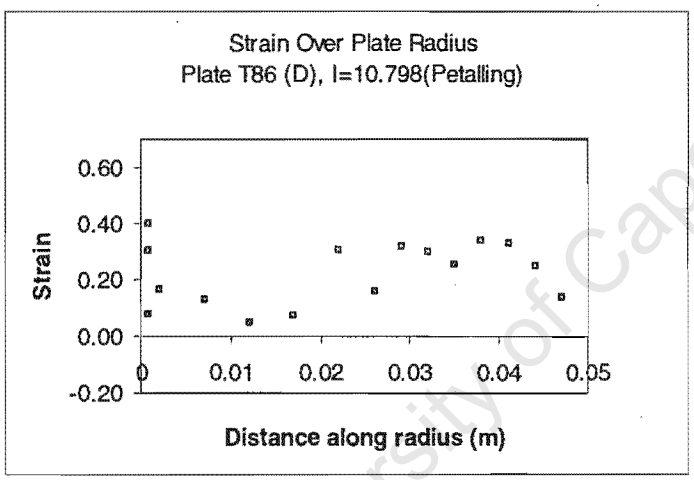

Figure IV.4 Strain Distribution Plate T86

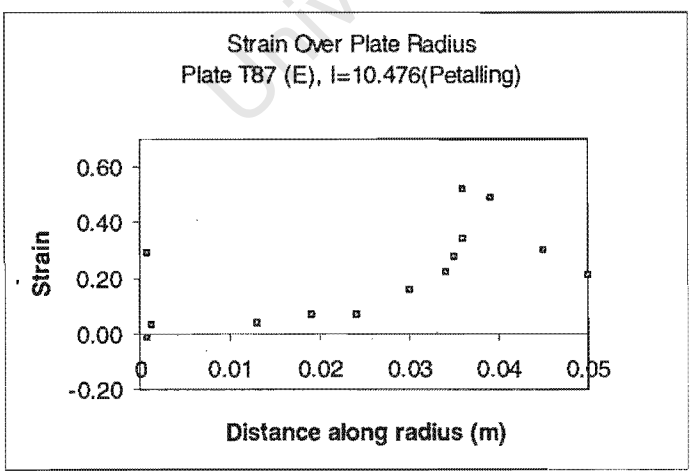

Figure IV.5 Strain Distribution Plate T87

2.6mm Plates

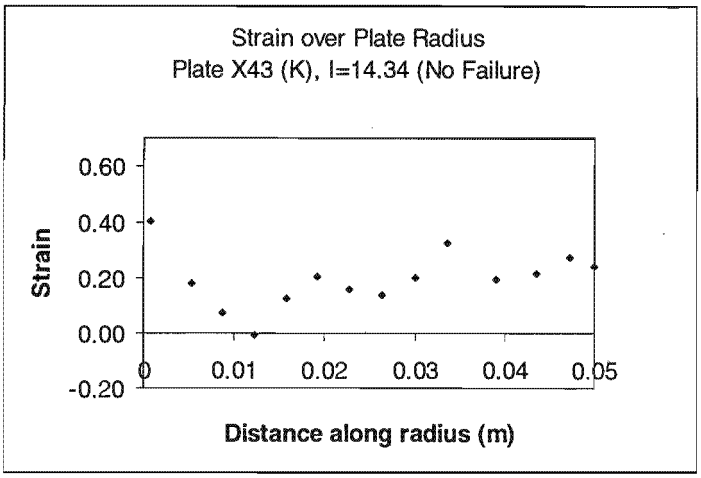

Figure IV.6 Strain Distribution Plate X43

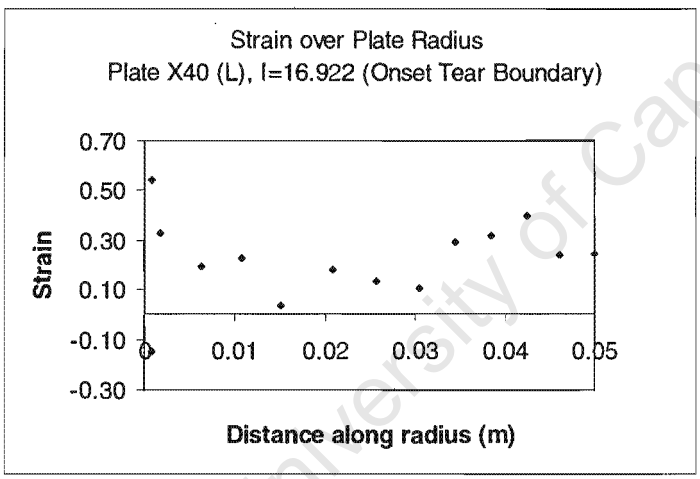

Figure IV.7 Strain Distribution Plate X40

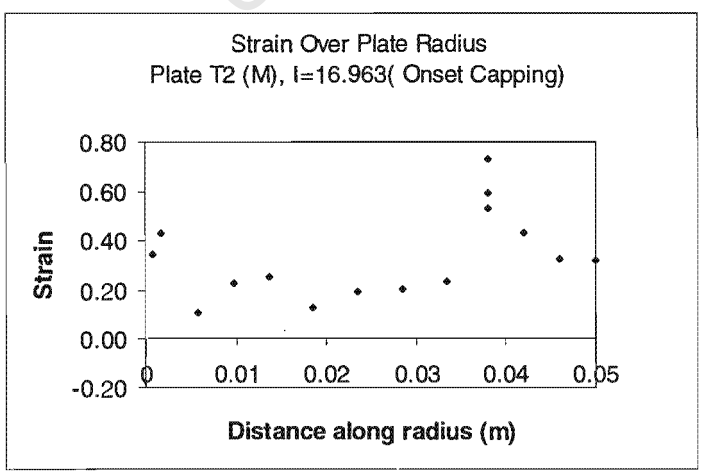

Figure IV.8 Strain Distribution Plate T2

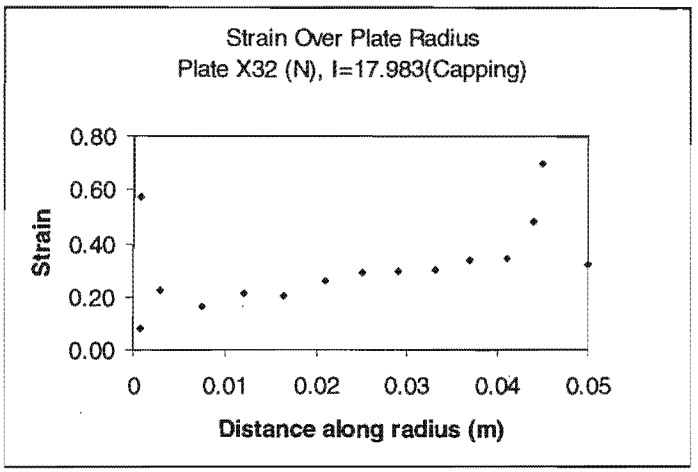

Figure IV.9 Strain Distribution Plate X32

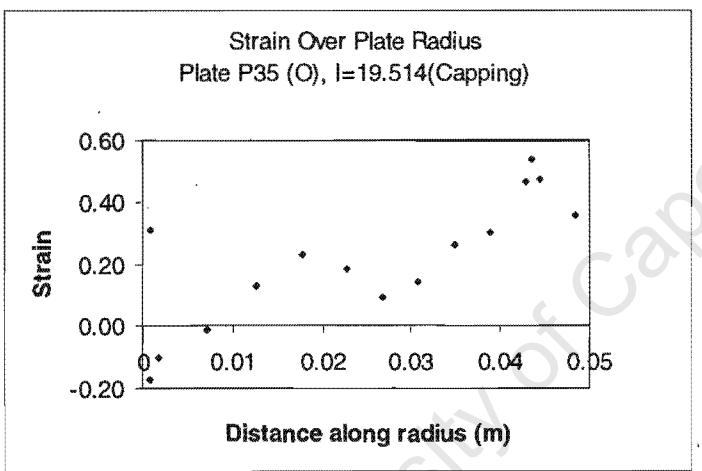

Figure IV.10 Strain Distribution Plate P35

3.6mm Plates

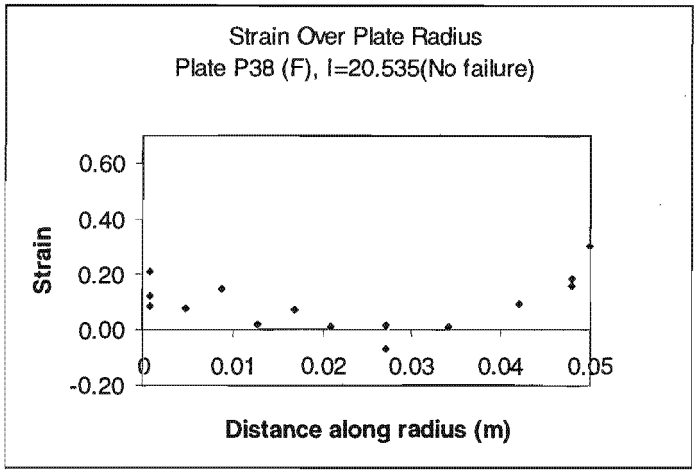

Figure IV.11 Strain Distribution Plate P38

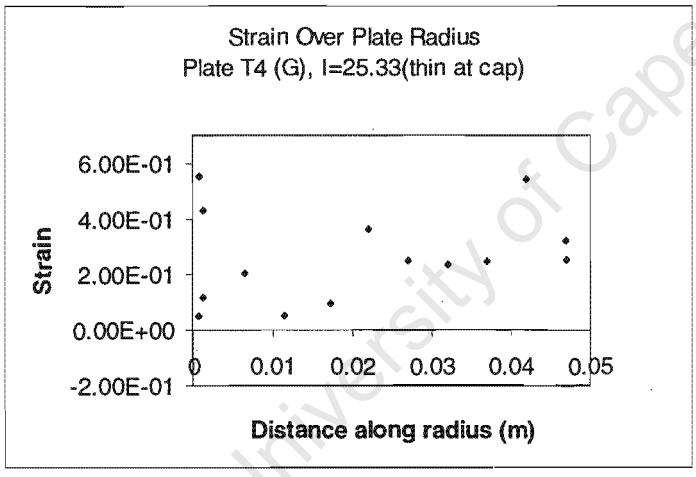

Figure IV.12 Strain Distribution Plate T4

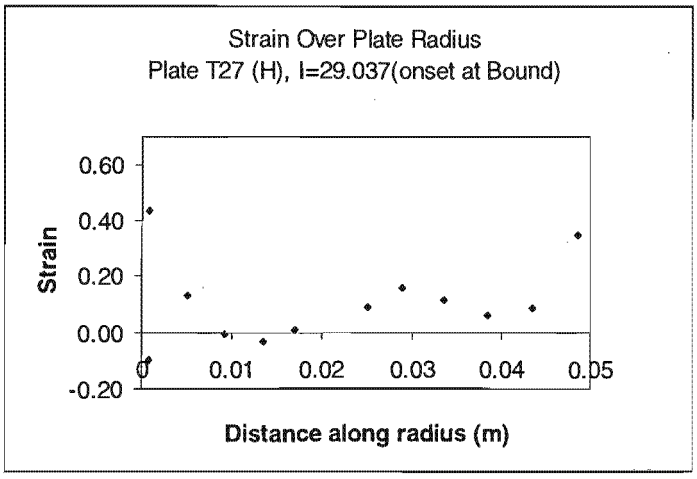

Figure IV.13 Strain Distribution Plate T27

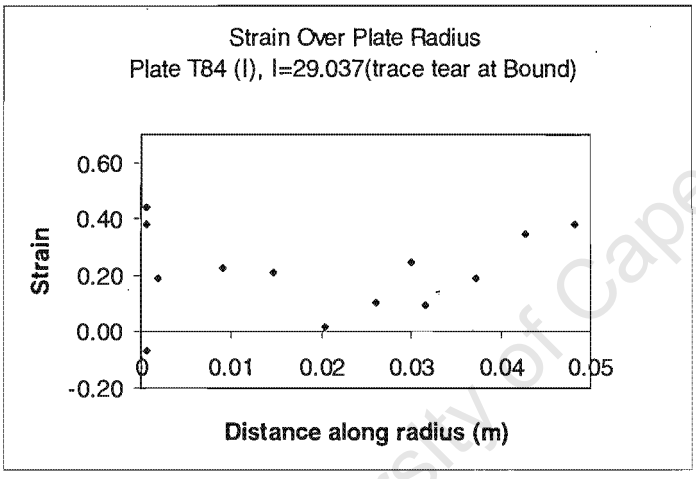

Figure IV.14 Strain Distribution Plate T84

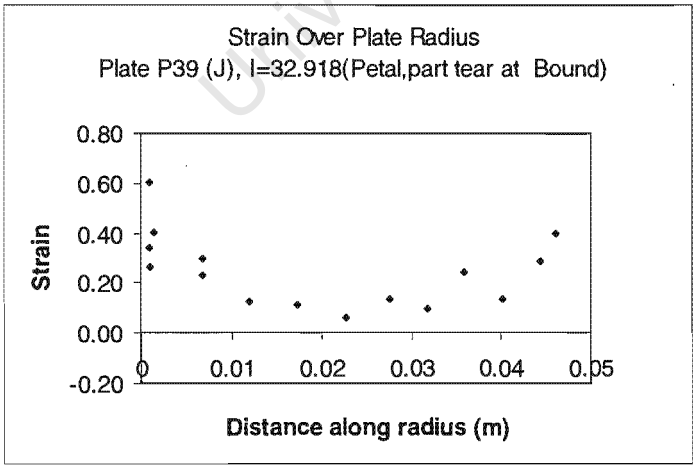

Figure IV.15 Strain Distribution Plate P39

APPENDIX V

SOURCE CODE

Data Analysis Code (Matlab)

```
Clear
% initial constants
unelong=1.10
nfiles=24 %input ('np of files');
twolet='md'  %input ('first two letters of file names','s')
cd d:\grain\m16
% loop through all the micrographs for each plate
for k=0:2;
   for j=0:9;
      if k+j>0
            num=k*10+j;
                  fname=[twolet,'00.txt']; %input
                  sname='mc.txt'; %output
                              fname(3)=num2str(k);
                  fname(4)=num2str(j);
                  load(fname);
                  name=eval([twolet,num2str(k),num2str(j)]);
                  ave=mean(name);
                  aveelo=(ave(13));
                  dim=size(name);
                        for i=1:dim(1);
                              if name(i,11)>=90;
                          orie(i)=name(i,11)-180;
                              else if name(i,11)<90
                          orie(i)=name(i,11);
                        end
                        end
                        end
                  aveorie=mean(orie);
                  % loop through all the grains
                  for i=1:dim(1);
                        angle(i)=(abs(orie(i)-aveorie))*pi/180;
                        gelon(i)=(name(i,13)-1)*cos(2*angle(i));
                        welon(i)=(gelon(i)+1)*name(i,7);
                  end
         elongation=(1+mean(gelon))/unelong;
         elong(num)=elongation;
         welongation=mean(welon)/(ave(7)*unelong);
         num=k*10+j;
         grainno(num)=num;
                  aveang(num)=aveorie;
         wel(num)=welongation;
         if num==nfiles
            break
         end
      end
   end
if num==nfiles
   break
end
end
cd d:\grain\
save md.txt grainno elong wel aveang  -ascii -double % write to file
```

Abaqus Input Decks.

Tensile Test

```
*heading
Tensile test specimen
**_____________________________________________________________
** Node Definition
*node
1,0,-0.0001,0
51,0.02,-0.0001,0
81,0.05,-0.0001,0
101,0.05,0.01,0
1011,0,0.003,0
1061,0.02,0.003,0
1111,0.030908712,0.01,0
9999,0.020,0.015,0
**_____________________________________________________________
*ngen
1,1011,101
51,1061,101
51,81,1
81,101,1
*ngen, line=c
1061,1111,1,9999
*nset, nset=l, generate
1,1011,101
*nset, nset=r, generate
51,1061,101
*nfill,nset=front
l,r,50,1
*nset, nset=inner, generate
51,101,1
*nset, nset=outer, generate
1061,1111,1
*nfill,nset=front
inner,outer,10,101
*ncopy,change number=100000, old set=front,new set=back, shift
0,0,-0.0005

*ncopy,change number=200000, old set=front,new set=back, shift
0,0,-0.001

*ncopy,change number=300000, old set=front,new set=back, shift
0,0,-0.0015

*ncopy,change number=400000, old set=front,new set=back, shift
0,0,-0.002

*ncopy,change number=500000, old set=front,new set=back, shift
0,0,-0.0025

*ncopy,change number=600000, old set=front,new set=back, shift
```

```
0,0,-0.003

*nset, nset=bott, generate
1,81,1
100001,100081,1
200001,200081,1
300001,300081,1
400001,400081,1
500001,500081,1
600001,600081,1
*nset, nset=left, generate
1,1011,101
100001,101011,101
200001,201011,101
300001,301011,101
400001,401011,101
500001,501011,101
600001,601011,101
*nset, nset=right, generate
51,1061,101
100051,101061,101
200051,201061,101
300051,301061,101
400051,401061,101
500051,501061,101
600051,601061,101
**_____
**Element Definition
*element, type=c3d8r
1,1,2,100002,100001,102,103,100103,100102
*elgen, elset=all
1,50,1,1,10,101,100,6,100000,1000
*elset,elset=centre,generate
3001,4000,1
**_____
**Boundary Definition
*boundary
left, xsymm
bott, ysymm
**node
**1011,0,0.0029
**_____
**Material Definition
*solid SECTION,ELSET=all,MATERIAL=STEEL
*MATERIAL,NAME=STEEL
*ELASTIC
210.E9,0.29
*PLASTIC
285E6,0
285E6,0.015
322E6,0.0312
368E6,0.0488
401E6,0.0638
427E6,0.0798
447E6,0.0952
464E6,0.111
478E6,0.126
```

```
489E6,0.141
498E6,0.154
508E6,0.171
515E6,0.185
522E6,0.200
522E6,0.228
522E6,1
*DENSITY
7800
**-----------------------------------------------------------------
*RESTART,WRITE, NUMBER=2
**----------------------------
** Loading
*STEP
*DYNAMIC,EXPLICIT
,0.01
*BOUNDARY,TYPE=VELOCITY
right, 1,1,0.6251
*MONITOR,NODE=51,DOF=1
*END STEP
```

Blast Loaded Plate

```
*Heading
1.6mm built in plate blast loaded - Failure Included
** Node Definition
*node
1,0,0.0027625
501,0.050,0.0027625
16001,0,0.0053625
16501,0.050,0.0053625
100001,0.050,0
100031,0.06,0
5100001,0.050,0.008125
5100031,0.06,0.008125
*ngen,nset=bot
1,501,1
*ngen,nset=top
16001,16501,1
*ngen,nset=binbot
100001,100031,1
*ngen,nset=bintop
5100001,5100031,1
*nfill
bot,top,16,1000
*nfill
binbot,bintop,50,100000
*nset,nset=left,generate
1,16001,1000
*nset,nset=right,generate
100031,5100031,100000
*mpc
pin,501,1800001
pin,1501,1900001
pin,2501,2000001
pin,3501,2100001
pin,4501,2200001
pin,5501,2300001
pin,6501,2400001
pin,7501,2500001
pin,8501,2600001
pin,9501,2700001
pin,10501,2800001
pin,11501,2900001
pin,12501,3000001
pin,13501,3100001
pin,14501,3200001
pin,15501,3300001
pin,16501,3400001
**Element Definition
*element,type=cax4r,elset=plate
1,1,2,1002,1001
*elgen,elset=plate
1,500,1,1,16,1000,500
*element,type=cax4r,elset=built
20000,100001,100002,200002,200001
```

```
*elgen,elset=built
20000,30,1,1,50,100000,30
*element,type=cax3,elset=plate
9999999,16500,16501,3500001
*elset,elset=top,generate
7500,8000,1
```

```
** Material Definition
*solid section,elset=plate,material=steel
*solid section,elset=built,material=steel
*MATERIAL,NAME=STEEL
*DENSITY
7846
*ELASTIC
210E9,.3
*PLASTIC
285E6,0
285E6,0.015
322E6,0.0312
368E6,0.0488
401E6,0.0638
427E6,0.0798
447E6,0.0952
464E6,0.111
478E6,0.126
489E6,0.141
498E6,0.154
508E6,0.171
515E6,0.185
522E6,0.200
522E6,0.228
522E6,1
*RATE DEPENDENT
40,5
**Failure Criterion
*SHEAR FAILURE
0.7
```

```
** Boundary Definition
*boundary
bintop,encastre
binbot,encastre
left,xsymm
*restart,write,number=30
```

```
** Blast Loding step
*step, nlgeom=yes
*DYNAMIC,EXPLICIT
,2.4E-6
*DLOAD
top,P3NU                        ** User defined Load see next section of
*MONITOR,NODE=1,DOF=2           ** appendix
*END STEP
*STEP
*DYNAMIC,EXPLICIT
,34E-6
*DLOAD, OP=NEW
*MONITOR,NODE=1,DOF=2
*END STEP
```

```
** Inertia Respose
*STEP
*DYNAMIC,EXPLICIT
,200E-6
*DLOAD, OP=NEW
*MONITOR,NODE=1,DOF=2
*END STEP
```

Abaqus User Loading (Fortran) (Grobbelaar [57])

```
SUBROUTINE VDLOAD(NBLOCK,NDIM,STEPTIME,TOTALTIME,AMPLITUDE,
     *                  CURCOORDS,VELOCITY,DIRCOS,JLTYP,VALUE)
C
      INCLUDE 'vaba_param.inc'
C
      dimension CURCOORDS(NBLOCK,NDIM), VELOCITY(NBLOCK,NDIM),
     *          DIRCOS(NBLOCK,NDIM,NDIM), VALUE(NBLOCK)
C
      REAL*8 R,PO,K
C     ------------------------------------------------------------------
C     define constants
      PO=4.95D9
      K=180.0D0
C     ------------------------------------------------------------------
C
c       loading function
      DO KM=1,NBLOCK
      write(6,*)'CURCOORDS =',curcoords(KM,1),curcoords(KM,2)
      end do
c
      DO KM = 1, NBLOCK
       if (JLTYP.eq.23) then
         VALUE(KM) = 0.D0
         R=curcoords(KM,1)
C        apply constant pressure to over area of explosive
         IF (R.lt.0.0165D0) THEN
             VALUE(KM)=PO
C         apply exponentially decaying pressure to outer edge
         ELSEIF ((R.ge.0.0165D0).and.(R.lt.0.05D0)) THEN
             VALUE(KM)=PO*DEXP(-K*(R-0.0165D0))
         ELSE
             VALUE(KM)=0.D0
         ENDIF
C       if not within blast time value=0
       endif
      write(6,*)'NBLOCK =',KM
      write(6,*)'R =',R
      write(6,*)'VALUE =',VALUE(KM)
      ENDDO
C -------------------end subroutine-------------------------------------
c
      RETURN
      end
```